



12-2017

Noncontact Vital Signs Detection

Lingyun Ren

University of Tennessee, lren1@vols.utk.edu

Recommended Citation

Ren, Lingyun, "Noncontact Vital Signs Detection. " PhD diss., University of Tennessee, 2017.
https://trace.tennessee.edu/utk_graddiss/4833

This Dissertation is brought to you for free and open access by the Graduate School at Trace: Tennessee Research and Creative Exchange. It has been accepted for inclusion in Doctoral Dissertations by an authorized administrator of Trace: Tennessee Research and Creative Exchange. For more information, please contact trace@utk.edu.

To the Graduate Council:

I am submitting herewith a dissertation written by Lingyun Ren entitled "Noncontact Vital Signs Detection." I have examined the final electronic copy of this dissertation for form and content and recommend that it be accepted in partial fulfillment of the requirements for the degree of Doctor of Philosophy, with a major in Electrical Engineering.

Aly E. Fathy, Jinyuan Sun, Major Professor

We have read this dissertation and recommend its acceptance:

Tai-Gang Nieh, Hairong Qi

Accepted for the Council:

Carolyn R. Hodges

Vice Provost and Dean of the Graduate School

(Original signatures are on file with official student records.)

Noncontact Vital Signs Detection

A Dissertation Presented for the
Doctor of Philosophy
Degree
The University of Tennessee, Knoxville

Lingyun Ren
December 2017

Copyright © 2017 by Lingyun Ren
All rights reserved.

DEDICATION

*To my parents Xiaoxiang Ren, Huizhen Zhou, and my beloved wife, Naijia Hao
Their support means everything to me*

ACKNOWLEDGEMENTS

I wish to express my gratitude to all the people who have helped me through my Ph.D pursuit in the past six years, especially to my advisor Dr. Aly E. Fathy. His profound knowledge, extensive experience and keen insight of RF and microwave field have helped me solve various problems in my research. He is not only an excellent academic advisor, but also a wise mentor outside my research. His patience, support and encouragement make this work possible. I wish to express my gratitude to my co-advisor Dr. Jinyuan Sun as well. Her supervision and support help me to complete my degree.

I would like to acknowledge my committee members, Dr. Hairong Qi, and Dr. T.G. Nieh for their review and advices of my dissertation.

I would like to acknowledge Dr. Haofei Wang and Dr. Quanhua Liu for their help and support in health monitoring of using SFCW radar and UWB pulse radar. Their expertise in radar techniques helps me to solve many problems.

I would like to acknowledge Dr. Krishna Naishadham and Dr. Jean Piou for their invaluable suggestions and help in applying state space method to UWB radar data for human health monitoring. Their expertise in signal processing helps me to enhance the performance of our biomedical radar systems.

I would like to express my appreciation to my lab mates in Dr. Fathy's group for their support: Farnaz Foroughian, Sabikun Nahar, Farhan Quaiyum, Matthew Richardson, Farshid Tamjid, Abdulrahman Bin and so on. Special thanks to Farnaz Foroughian and Sabikun Nahar for their help in improving biomedical radar and doing many experiments with me.

I would like to appreciate my previous group mates who have graduated from Dr. Fathy's group: Koo Yun Seo, Reza Ghahremani, Yazhou Wang, Ki Ryung Shin, Essam Elkhoully, Mohamed Saleh, Dounia Baiya. Special thanks to Dr. Koo Yun Seo for his support and mentorship of my first two years in Dr. Fathy's group.

ABSTRACT

Human health condition can be accessed by measurement of vital signs, i.e., respiratory rate (RR), heart rate (HR), blood oxygen level, temperature and blood pressure. Due to drawbacks of contact sensors in measurement, non-contact sensors such as imaging photoplethysmogram (IPPG) and Doppler radar system have been proposed for cardiorespiratory rates detection by researchers.

The UWB pulse Doppler radars provide high resolution range-time-frequency information. It is bestowed with advantages of low transmitted power, through-wall capabilities, and high resolution in localization. However, the poor signal to noise ratio (SNR) makes it challenging for UWB radar systems to accurately detect the heartbeat of a subject. To solve the problem, phased-methods have been proposed to extract the phase variations in the reflected pulses modulated by human tiny thorax motions. Advance signal processing method, i.e., state space method, can not only be used to enhance SNR of human vital signs detection, but also enable the micro-Doppler trajectories extraction of walking subject from UWB radar data.

Stepped Frequency Continuous Wave (SFCW) radar is an alternative technique useful to remotely monitor human subject activities. Compared with UWB pulse radar, it relieves the stress on requirement of high sampling rate analog-to-digital converter (ADC) and possesses higher signal-to-noise-ratio (SNR) in vital signs detection. However, conventional SFCW radar suffers from long data acquisition time to step over many frequencies. To solve this problem, multi-channel SFCW radar has been proposed to step through different frequency bandwidths simultaneously. Compressed sensing (CS) can further reduce the data acquisition time by randomly stepping through 20% of the original frequency steps.

In this work, SFCW system is implemented with low cost, off-the-shelf surface mount components to make the radar sensors portable. Experimental results collected from both pulse and SFCW radar systems have been validated with commercial contact sensors and satisfactory results are shown.

TABLE OF CONTENTS

Chapter One Introduction and General Information	1
1.1 State-of-the-art	1
1.1.1 Current Status of Biomedical Radar	2
1.1.2 Radar Operating Frequencies.....	4
1.1.3 Hardware Implementation.....	4
1.1.4 Signal Processing	4
1.1.5 Validation Method	8
1.1.6 Detection Accuracy	8
1.2 Contributions	11
1.3 Organization of the Dissertation	11
Chapter Two Phase Based Methods for Heart Rate Detection using UWB	
Impulse Doppler Radar	14
2.1 Background	14
2.2 Mathematical Model	16
2.3 Phase-Based Methods	20
2.3.1 Complex Signal Demodulation.....	22
2.3.2 Arctangent Demodulation	24
2.3.3 State Space Method in Conjunction with CSD and AD	24
2.4 Experimental Results	26
2.4.1 Subject 1 Withheld Respiration.....	27
2.4.2 Subject 2 Breathed Normally	30
2.4.3 Actuator Experiment	32
2.4.4 Block Processing SSM.....	34
2.4.5 Two Subjects Breathed Normally.....	34
2.5 Discussion	37
2.6 Conclusion.....	42
Chapter Three Short Time State Space Method for Micro-Doppler Identification	
of Walking Subject using UWB Impulse Doppler Radar.....	43
3.1 Background	43
3.2 Short time state space method for UWB Impulse Radar	45
3.3 Human Walking Model	46
3.4 Full Wave Electromagnetic Model for a Human in Motion	47
3.5 Simulation results	50
3.6 Experimental results.....	51
3.6.1 Subject Walking Towards Radar.....	51
3.6.2 Subject Walking in front of radar at oblique directions	55
3.7 Conclusion.....	71
Chapter Four Alternative Ultra-Wideband Transceiver Based on Stepped-	
Frequency Continuous Wave Operation and Compressive Sensing	72
4.1 Background	72
4.2 Design of Two-Channel SFCW Radar System.....	75

4.2.1 Overview of the SFCW Radar System.....	76
4.2.2 Frequency Synthesizer Based on DDS-Driven PLL Architecture.....	76
4.3 Application of CS Theory to SFCW Radar	78
4.3.1 Brief Overview of Compressive Sensing.....	79
4.3.2 CS-based Stepped-Frequency Signal Processing	80
4.4 Simulation and Experimental Results	80
4.4.1 Simulation Results	80
4.4.2 Experimental Results	83
4.5 Conclusion and Future Direction	88
Chapter Five Non-Invasive Detection of Cardiac and Respiratory Rates from Stepped Frequency Continuous Wave Radar Measurements Using the State Space Method.....	89
5.1 Background	89
5.2 SFCW Radar	90
5.3 Two-Channel SFCW Radar System Integration	92
5.4 Experimental Results	95
5.4.1 Subject holds breath	95
5.4.2 Subject breathes normally	97
5.4.3 Subject facing radar at different angles.....	97
5.5 Discussion and Summary	97
Chapter Six Comparison Study of Non-Contact Vital Signs Detection Using a Doppler Stepped-Frequency Continuous Wave Radar and Camera-Based Imaging Photoplethysmography	99
6.1 Background	99
6.2 Operating Principle of SFCW Radar and IPPG System	102
6.2.1 SFCW radar	102
6.2.2 IPPG system	104
6.3 Experimental Setup	106
6.3.1 SFCW Radar Implementation	106
6.3.2 IPPG System Implementation	109
6.4 Experimental Results	110
6.4.1 Comparison between SFCW radar and IPPG System.....	110
6.4.2 SpO ₂ Measurements.....	115
6.5 Discussion	120
6.6 Conclusion.....	120
Chapter Seven Conclusion and future work.....	123
7.1 Accomplishments and Contributions	123
7.2 Publications	124
7.3 Conclusion.....	127
7.4 Direction of Future Work.....	128
Bibliography	129
Appendix.....	142
A.1 Differentiate and cross-multiply (DACM).....	143
A.2 Imbalance compensation method	144

Vita.....	145
-----------	-----

LIST OF TABLES

Table 1.1 Comparison between different radar types..	3
Table 1.2 Operating frequencies of biomedical radars.....	4
Table 1.3 Hardware implementations of biomedical radars..	5
Table 1.4 Signal processing of biomedical radars.....	6
Table 1.5 Performance validations of biomedical radars..	7
Table 1.6 Detection accuracies of biomedical radars.....	8
Table 2.1 Specifications of components used in UWB radar..	16
Table 2.2 UWB radar system parameters.....	16
Table 2.3 Comparison of each method in heart rate (Beats/Minute), deviation (%) and SNR (dB)..	25
Table 2.4 Comparison of each method in heart rate (Beats/Minute), deviation (%) and SNR (dB)..	28
Table 2.5 Comparison between CSD and AD.....	35
Table 2.6 Current methods to detect respiratory rate (RR) and heart rate (HR) for UWB impulse Doppler radar..	35
Table 3.1 μ -D signatures of a walking target with height 1.7 m and speed 0.33 m/s.....	44
Table 3.2 μ -D signatures of walking target with height 1.72 m and speed 0.38 m/s.....	47
Table 3.3 μ -D signatures of walking target with height 1.71 m and speed 0.38 m/s.....	51
Table 3.4 μ -D signatures of walking target with height 1.71 m and speed 0.37 m/s.....	52
Table 3.5 μ -D signatures of walking target with height 1.75 m and speed 0.4 m/s..	54

Table 3.6 μ -D signatures of walking target with height 1.75 m and speed 0.40 m/s.....	55
Table 4.1 Parameters of two TI ADC chips.....	58
Table 4.2 Parameters of the two-channel SFCW radar system.....	66
Table 5.1 Components used for SFCW radar.....	77
Table 5.2 Dynamic range analysis of the transceiver.....	78
Table 5.3 SSM error in heart rate for subject..	81
Table 6.1 Components used in experimental setup.....	91
Table 6.2 Mean, standard deviation, upper and lower limits statistics for the ambient light intensity effects on SpO2.....	99
Table 6.3 Summary of different radar types for remote detection.....	99

LIST OF FIGURES

Figure 1.1 (a) setup of ECG. (b) physical discomfort caused by ECG electrodes..	2
Figure 2.1 Schematic of UWB radar system and prototype..	15
Figure 2.2 Conventional FFT method to detect vital signs..	18
Figure 2.3 Proposed phase based methods..	18
Figure 2.4 Block diagram of (a) CSD; (b) AD for UWB radar system, where $M(t) = \text{Imag}\{Y(t,0)\}$, $R(t) = \text{Real}\{Y(t,0)\}$, F is a multiple of 180° , k is an integer.	20
Figure 2.5 Experiment setup with (a) human subject, (b) linear actuator.	24
Figure 2.6 Reference and demodulated raw data with AD from right heart side..	25
Figure 2.7 When subject 1 held breathing, detected heart rate using (a) reference FFT, (b) CSD, (c) AD, (d) SSM, (e) SSM-CSD and (f) SSM-AD..	26
Figure 2.8 When subject 2 breathed normally, detected heart rate using (a) reference FFT, (b) CSD, (c) AD, (d) SSM, (e) SSM-CSD and (f) SSM-AD..	28
Figure 2.9 Detected actuator movement frequency using (a) reference FFT, (b) CSD, (c) AD, (d) SSM, (e) SSM-CSD and (f) SSM-AD..	29
Figure 2.10 (a) Heart rate estimates obtained using block-processing SSM. (b) Cumulative distribution function of the heart rate.....	30
Figure 2.11 (a) Breathing rates estimated using block-processing SSM. (b) Cumulative distribution function of the respiration rate..	31
Figure 2.12 (a) Experiment setup. (b) Localization with UWB system..	32
Figure 2.13 Heart rate detection of subject 1 with arctangent method.....	32
Figure 2.14 Heart rate detection of subject 2 with arctangent method.	32
Figure 2.15 In the second experiment, detected heart rate using CSD and AD..	34
Figure 2.16 In the second experiment, detected heart rate using CSD with hamming window and CSD without Hamming window	34

Figure 3.1 (a) Human motion model with 17 body parts. (b) μ -D frequencies of different body joints in one cycle.....	41
Figure 3.2 (a) Human joint body. (b) Human ellipsoid body. (c) Meshed human body and (d) Human scattering scenario.	43
Figure 3.3 (a) Spectrogram using STFT when sliding window length of 24 samples, (b) spectrogram using STSSM for a sliding window length of 24 samples.	44
Figure 3.4 (a) HRRP of walking subject with arms swinging, (b) Boulic model of subject at the radial direction, (c) spectrogram using STFT when sliding window length of 50 pulses, (d) spectrogram using STSSM when sliding window length of 50 pulses.....	46
Figure 3.5 (a) HRRP of walking subject 1 (b) Boulic model of subject at 30° to the radial direction, (c) spectrogram using STFT when sliding window length of 45 pulses, (d) spectrogram using STSSM when sliding window length of 45 pulses.	50
Figure 3.6 (a) HRRP of walking subject 1 (b) Boulic model of subject at 60° to the radial direction, (c) spectrogram using STFT when sliding window length of 45 pulses, (d) spectrogram using STSSM when sliding window length of 45 pulses.	52
Figure 3.7 (a) HRRP of walking subject 2 (b) Boulic model of subject at 30° to the radial direction, (c) spectrogram using STFT when sliding window length of 45 pulses, (d) spectrogram using STSSM when sliding window length of 45 pulses.	53
Figure 3.8 (a) HRRP of walking subject 2 (b) Boulic model of subject at 60° to the radial direction, (c) spectrogram using STFT when sliding window length of 45 pulses, (d) spectrogram using STSSM when sliding window length of 45 pulses.	54
Figure 4.1 Time-frequency representation of stepped-frequency continuous wave	60
Figure 4.2 Block diagram of the multi-channel SFCW radar system.....	62
Figure 4.3 Block diagram of a DDS with the output of each stage illustrated.....	63
Figure 4.4 Photograph of the two-channel DDS board	63

Figure 4.5 Data measurement schemes: (a) conventional scheme where all the frequencies are measured on each channel and (b) CS scheme where only randomly selected frequencies are measured on each channel. The filled rectangles indicate the selected frequencies. The frequencies are indexed by (pq) pairs where p denotes the channel index and q denotes the frequency index on that channel.	66
Figure 4.6 Simulation geometry	68
Figure 4.7 Synthesized HRRPs of the target at various CSRs	68
Figure 4.8 Synthesized HRRPs of the target for various SNR levels at CSR of 40%	69
Figure 4.9 Experimental setup	70
Figure 4.10 Synthesized HRRPs of the corner reflector at various CSRs.....	71
Figure 5.1 Block diagram of SFCW radar system.	76
Figure 5.2 Stack-up implementation of two-channel SFCW radar system	77
Figure 5.3 (a) Layout of transceiver board; (b) fabricated transceiver board.	78
Figure 5.4 Layout of diplexer board with LNA and PA.	78
Figure 5.5 Experimental setup	79
Figure 5.6 Demodulated heartbeat signal of the subject.....	79
Figure 5.7 Detected heart rate of Subject 1 (a) with FFT, (b) with SSM.....	80
Figure 5.8 Subject breathes normally. Detected vital signs of subject (a) with FFT and (b) with SSM	80
Figure 5.9 Subject at different positions. (a) right 45°; (b) right 90°; (c) left 45°; (d) left 90°; (e) back and (f) front	81
Figure 6.1 Process of extracting vital signs from video recorded by camera; Step I: take average from all pixels of each video frame and plot it in time; Step II: filter the signal with a band-pass filter; Step III: acquire the PPG signals after band-pass filtering.	89

Figure 6.2 (a) Block diagram of the experimental setup. (b) Experimental setup in lab.	92
Figure 6.3 SNRs of SFCW radar and iPPG system with regard to different levels of light illumination.	94
Figure 6.4 Four orientations of subject (a) front, (b) back, (c) right, (d) left	94
Figure 6.5 Spectra of demodulated signals from (a) SFCW radar, (b) camera with 520 nm filter when illumination level is 500 lx	94
Figure 6.6 When illumination is 500 lx, comparison of ratio to reference using SFCW radar and camera in respiratory rate detection when subject is at orientation of (a) front, (b) left, (c) right, and (d) back.	95
Figure 6.7 When illumination is 500 lx, comparison of ratio to reference using SFCW radar and camera in heart rate detection when subject is at orientation of (a) front, (b) left, (c) right, and (d) back.	96
Figure 6.8 When subject is 2 m away, comparison of ratio to reference using SFCW radar and camera in respiratory rate detection when illumination level is (a) 500 lx, (b) 200 lx, and (c) 100 lx.....	97
Figure 6.9 When subject is 2 m away, comparison of ratio to reference using SFCW radar and camera in heart rate detection when illumination level is (a) 500 lx, (b) 200 lx, and (c) 100 lx.....	97
Figure 6.10 When subject is at orientation of front, comparison of ratio to reference using SFCW radar and camera in respiratory rate detection when illumination level is (a) 500 lx, (b) 200 lx, and (d) 100 lx	98
Figure 6.11 When subject is at orientation of front, comparison of ratio to reference using SFCW radar and camera in heart rate detection when illumination level is (a) 500 lx, (b) 200 lx, and (d) 100 lx	98

LIST OF ABBREVIATIONS

RR	Respiratory Rate
HR	Heart Rate
ECG	Electrocardiography
iPPG	Imaging Photo-plethysmographic
NLOS	Non-line-of-sight
UWB	Ultra-wideband
CW	Continuous Wave
FMCW	Frequency Modulated Continuous Wave
SFCW	Stepped Frequency Continuous Wave
CSD	Complex Signal Demodulation
AD	Arctangent Demodulation
SSM	State Space Method
STSSM	Short Time State Space Method
STFT	Short Time Fourier Transform
FFT	Fast Fourier Transform
SAR	Synthetic Aperture Radar
SNR	Signal-to-noise Ratio
ADC	Analog-to-digital Converter
FPGA	Field-programmable gate array
HRRP	High-resolution Range Profile
SpO ₂	Blood Oxygen Saturation Levels
PCB	Printed Circuit Board
CS	Compressive Sensing
μ-D	micro-Doppler
IR	Impulse Radio
PRF	Pulse Repetition Frequency
PRT	Pulse Repetition Time

CHAPTER ONE

INTRODUCTION AND GENERAL INFORMATION

Vital signs, i.e. respiratory rate (RR), heart rate (HR) and blood oxygen level, provide critical information for human health care, which help to monitor subject health conditions, make life-saving decisions, determine treatment protocols to follow, identify acute medical problem and so on.

For RR detection, the most popular way is to use a belt sensor wrapped around the chest or belly of subject. Due to periodical pressure variations caused by human inhale and exhale motions, belt sensors are capable of monitoring the movements of respiration. For HR detection, contact Electrocardiography (ECG) has been widely used for the real-time monitoring. Bed-type sensor capable of HR and RR monitoring has been proposed as well as a sleep monitoring system in [1]. Though the noninvasive feature of aforementioned sensors makes them attractive for long-term daily monitoring, their drawbacks have greatly limited the applications of these contact sensors. For belt sensor, it needs be wrapped tightly enough to have accurate readings and this may cause discomfort of subject. For ECG, it is difficult to setup and place all the electrodes on the human body and direct contact between skin and electrodes limits its applications for some cases. For example, it may cause physical skin irritation to subjects like babies and patient with burn injury for prolonged use of contact ECG, as shown in Figure 1.1. Though showing capability of both HR and RR identification, the air-mattress sensor is not portable and may be bulky to relocate for use.

To solve this problem, non-contact sensors such as laser based system, camera-based Photo-plethysmographic (PPG) and radar sensors have been developed targeting the same applications without compromising the accuracy and reliability [2]. Compared with its non-contact counterparts, radar systems have the capability of non-line-of-sight (NLOS) monitoring, and can see through fog, smoke, and foliage and cement wall in long distances. As a result, we focus on radar techniques on vital signs monitoring in this work.

1.1 State-of-the-art

By now, various types of radar systems have been developed by different groups for biomedical applications, including continuous wave (CW) radar, frequency modulated continuous wave (FMCW) radar, ultra wideband (UWB) radar and stepped frequency continuous wave (SFCW) radar [3-14].

1.1.1 Current Status of Biomedical Radar

CW radars are very popular in vital signs monitoring and Doppler information extraction due to its low cost and simple architecture. In [15], a dc-coupled CW radar sensor has been presented to provide a noncontact and noninvasive approach for accurate respiration measurement in motion-adaptive radiotherapy. In [16], successful measurements of heart and respiration rates of a human subject at long distances, up to 69 meters, have been demonstrated using CW radar systems. Meanwhile, various algorithms have been proposed for CW radar to enhance the accuracy in respiratory and heart rates identification. In [17], the complex signal demodulation (CSD) technique is proposed for the elimination of unwanted torso motions. In [18], arctangent demodulation (AD) together with dc offset calibration greatly improves the accuracy of heart rate detection. Although CW radars are simple to implement and low-cost, they do not provide range information of subjects and capability of multiple subjects monitoring, leading to limited applications.

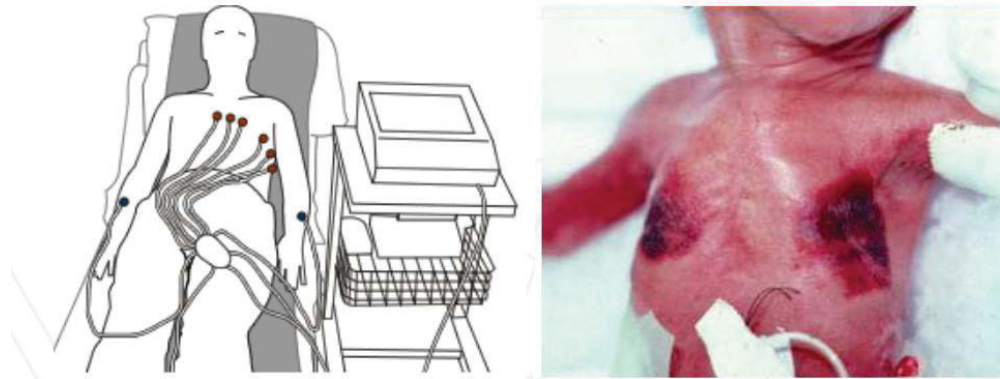


Figure 1.1 (a) setup of ECG. (b) physical discomfort caused by ECG electrodes.

UWB impulse radars, operating in a wideband bandwidth, send narrow pulses in a scale of picosecond. By collecting and processing the reflected pulses, we are able to identify the distance of objects with high range resolution, localize subjects in synthetic aperture radar (SAR) image and monitor tiny motions of subjects. These capabilities of UWB radars have led to many applications benefiting people such as, through-wall imaging, ground penetrating detection of landmines, radar-based driver assistance, and home care of the elderly. In order to provide cardio-respiratory estimation with high accuracy, various UWB radar systems have been proposed [19-22]. In [22], for example, a UWB impulse radar using circularly polarized antennas has enhanced the accuracy for the estimation of cardio-respiratory rates. In [23], a correlation receiver is implemented to avoid direct sampling of the pulses with picosecond precision. The sensing precision is verified by breath-rate measurements. In [24], an integrated UWB transceiver has been developed for respiration rate detection. However, the transmitted power of UWB radar is limited and accompanied by a relatively high noise over

the wide band, which causes its low signal-to-noise ratio (SNR). Moreover, UWB impulse radar requires high-speed analog-to-digital converters, which inevitably increases its complexity and hardware cost in system design.

Alternatively, Frequency-Modulated Continuous Wave (FMCW) radar, which overcomes the drawbacks of CW and UWB impulse radars simultaneously, has been successfully applied to non-contact vital signs detection and subject localization. In [4], a hybrid radar system that integrates the FMCW mode and interferometry mode has been presented for indoor precise positioning and versatile life activity monitoring. In [6], an UWB 80 GHz FMCW radar system with bandwidth of 10 GHz is developed for contactless monitoring of HR and RR and the results are validated with contact sensors. In [25], a linear FMCW minimizing the undesired effects of surrounding clutter has been exploited for noncontact range tracking of vital signs. Since it transmits CW signal, high transmitting power can be used without need for high-speed ADCs. However, calibration is still needed to compensate for non-linearities in frequency sweeping [26, 27].

SFCW radar is widely studied for its application for vital signs monitoring, gait analysis, and subject localization due to its advantages [28, 29]. Compared with CW radar systems, SFCW radar systems have the advantages of localization capability and the potential to monitor multiple subjects in real time. SFCW radar system can approximate UWB pulses in frequency domain, and therefore should have similar capabilities like UWB systems. It requires low-speed ADCs as it has narrow instantaneous bandwidth, and frequencies can be skipped or can even be randomly selected, which enables compressive sensing for even faster detection [30]. It also produces relatively strong received signals as it transmits long-duration waveforms; hence, it possesses higher SNRs than UWB radar in vital signs detection. Furthermore, compared with FMCW radar, it is easier to calibrate the signal distortion caused by any imperfection of the SFCW radar system hardware. A comparison between different types of radar is presented in Table 1.1.

Table 1.1 Comparison between different radar types

	CW	UWB	FMCW	SFCW
Localization	No	Yes	Yes	Yes
Multiple Subjects	No	Yes	Yes	Yes
ADC Speed	Low	Fast	Low	Low
Calibration	-	-	Difficult	Easy

1.1.2 Radar Operating Frequencies

Table 1.2 summarizes the operating frequencies of various radars proposed by researchers for vital signs monitoring. The most common used frequencies and frequency bands are 2.4 GHz, 5.8 GHz, 60 GHz, 24 GHz, 3.1 – 10.6 GHz, 2 – 4 GHz and so on.

CW radars are widely used for Doppler detections and health monitoring, due to its high SNR and low system complexity. UWB radar, FMCW and SFCW radar are needed when both localization and μ -D information are needed of the subject. It is worth mentioning that configurable radar transceivers with both CW mode and UWB/FMCW mode are proposed to accommodate different scenarios. When accurate μ -D information is needed, CW mode will be on; while UWB/FMCW mode will be switched on when ranging or direction information is desirable of subjects. The UWB/FMCW mode can be utilized for more than one subject monitoring as well.

1.1.3 Hardware Implementation

Table 1.3 summarizes the techniques of biomedical radar hardware implementation. Generally, there are four ways to implement a biomedical radar transceiver, i.e., using bench instruments such as signal generator and vector network analyzer (VNA), utilizing commercial off-the-shelf components, using MMIC components for PCB design, utilizing CMOS design for integrated system. It is not recommended to implement biomedical radar with bench instruments due to its limitation of portability. This type of radar system can only be used for system demonstration. The radar transceivers implemented with off-the-shelf components is suitable to system prototyping. Satisfactory performance can be achieved using these components with housing, since electromagnetic interference (EMI) will be minimized in the system. However, they have bulky sizes and cannot be used for portable applications. The radar transceivers implemented with MMIC chips have the advantages of low cost and portability. With proper design of PCB layout, the EMI problem can be effectively avoided. Moreover, this type of radar transceivers is geared towards mass productions due to their simple architectures.

CMOS designs of integrated radar transceiver can minimize the system size while optimizing the system performance. Specifications of each component in the system can be customized. They have the advantages of low power requirement, small system size and so forth.

1.1.4 Signal Processing

Table 1.4 summarizes the signal processing methods for vital signs detection using biomedical radars. In [7], a new method was proposed to characterize the human random motion and detect the RR of subject under large 1-D motion. In [18], CSD was proposed for random motion cancellation in vital signs detection, with one radar at the front of subject, the other at the back. In [31], random body

Table 1.2 Operating frequencies of biomedical radars

Research Group	Radar Type	Measurement	Frequency/Bandwidth
Tu et al. [7]	CW	RR	5.8 GHz
Li et al. [18]	CW	HR/RR	within 4-7 GHz
Gu et al. [31]	CW	HR/RR	2.4 GHz
Kuo et al. [8]	CW	HR/RR	60 GHz
Kao et al. [12]	CW	HR/RR	60 GHz
Chuang et al. [32]	CW	HR/RR	60 GHz
Huang et al. [9]	CW	HR/RR	within 2.4-2.5 GHz
Chioukh et al. [10]	CW	HR/RR	12, 24 GHz
Wu et al. [11]	CW	HR/RR	2.4 GHz
Wang et al. [14]	CW	HR/RR	2.4 GHz
Vinci et al. [13]	CW	HR/RR	24 GHz
Park et al. [17]	CW	HR/RR	2.4 GHz
Baboli et al. [16]	CW	HR/RR	2.45 GHz
Wang et al. [33]	CW/Pulse	RR	1.5-4.5 GHz
Schleicher et al. [23]	Pulse	RR	3.1-10.6 GHz
Lazaro et al. [34]	Pulse	HR/RR	3.1-10.6 GHz
Wang et al. [6]	FMCW	HR/RR	75-85 GHz
Wang et al. [4]	FMCW/CW	HR/RR	5.72-5.88 GHz
Wang et al. [25]	FMCW	RR	5.72-5.88 GHz
Ren et al. [35]	SFCW	HR/RR	3.14-3.46 GHz
Liu et al. [29]	SFCW	RR	0.3-1.3 GHz

Table 1.3 Hardware implementations of biomedical radars

Research Group	Radar Type	Measurement	Technique
Tu et al. [7]	CW	RR	PCB
Li et al. [18]	CW	HR/RR	PCB
Gu et al. [31]	CW	HR/RR	PCB
Kuo et al. [8]	CW	HR/RR	CMOS
Kao et al. [12]	CW	HR/RR	CMOS
Chuang et al. [32]	CW	HR/RR	off-the-shelf components
Huang et al. [9]	CW	HR/RR	PCB
Chioukh et al. [10]	CW	HR/RR	Bench instruments
Wu et al. [11]	CW	HR/RR	PCB
Wang et al. [14]	CW	HR/RR	NA
Vinci et al. [13]	CW	HR/RR	PCB
Park et al. [17]	CW	HR/RR	NA
Baboli et al. [16]	CW	HR/RR	off-the-shelf components
Wang et al. [33]	CW/Pulse	RR	off-the-shelf components
Schleicher et al. [23]	Pulse	RR	PCB
Lazaro et al. [34]	Pulse	HR/RR	bench instruments
Wang et al. [6]	FMCW	HR/RR	PCB
Wang et al. [4]	FMCW/CW	HR/RR	off-the-shelf components
Wang et al. [25]	FMCW	RR	off-the-shelf components
Ren et al. [35]	SFCW	HR/RR	Bench instruments
Liu et al. [29]	SFCW	RR	Bench instruments

Table 1.4 Signal processing of biomedical radars

Research Group	Radar Type	Measurement	Signal Processing
Tu et al. [7]	CW	RR	1-D body motion characterization
Li et al. [18]	CW	HR/RR	CSD
Gu et al. [31]	CW	HR/RR	Random body movement cancellation
Kuo et al. [8]	CW	HR/RR	CSD
Kao et al. [12]	CW	HR/RR	Time domain recovery algorithm
Chuang et al. [32]	CW	HR/RR	FFT
Huang et al. [9]	CW	HR/RR	upper-bound and linear matrix inequality relaxation
Chioukh et al. [10]	CW	HR/RR	FFT
Wu et al. [11]	CW	HR/RR	FFT
Wang et al. [14]	CW	HR/RR	Random body movement cancellation
Vinci et al. [13]	CW	HR/RR	FFT
Park et al. [17]	CW	HR/RR	AD
Baboli et al. [16]	CW	HR/RR	FFT
Wang et al. [33]	CW/Pulse	RR	FFT
Schleicher et al. [23]	Pulse	RR	FFT
Lazaro et al. [34]	Pulse	HR/RR	Moving target indicator canceller
Wang et al. [6]	FMCW	HR/RR	FFT
Wang et al. [4]	FMCW/CW	HR/RR	FFT
Wang et al. [25]	FMCW	RR	phase-based range-tracking algorithm
Ren et al. [35]	SFCW	HR/RR	State space method
Liu et al. [29]	SFCW	RR	FFT

movement cancellation technique using iPhone to track human motions was proposed. This method was based on phase compensation at the RF front or baseband. In [8], a CMOS RF sensor with clutter cancellation was designed and CSD was utilized to process the radar data. In [12], time domain recovery algorithm was presented to detect the vital signs when subject displacement is larger or comparable to wavelength of transmitted signal. In [9], signal model identification was formulated into a quadratically constrained l_1 minimization problem and solved using upper-bound and LMI relaxation. In [14], the random body movement of the subject between two self-injection-locked radar could be effectively cancelled with wireless mutual injection locking of the two radars. In [17], AD was proposed together with dc tracking and compensation scheme for accurate real-time HR monitoring. In [34], the moving target indicator canceller was proposed to suppress the respiration harmonics so that HR was highlighted in the spectrum. In [25], phase-based range-tracking algorithm was developed for RR monitoring using linear FMCW radar with robustness against noise and clutter. In [35], state space method was proposed for HR/RR detection using SFCW radar. It successfully suppressed the unwanted harmonics and intermodulation interferences in the spectrum.

1.1.5 Validation Method

Table 1.5 summarizes the various methods which have been utilized to validate the performance of biomedical radar and effectiveness of algorithms. Generally, there are two ways to validate the performance of radar system, i.e., using programmable actuator, and commercial contact sensors. In [7], experiment using actuator was conducted for performance validation. RR baseline of subject was determined as the reference of respiration signal. In [31], the programmable shaker was used to evaluate the system performance. Data collected from belt sensor and pulse sensor served as the reference in human subject test. In [9], the accuracy of proposed system was tested with an experiment using programmable actuator. In [10], a commercial oximeter was used as reference for human HR in the 13 experiments. In [17, 36], a finger pulse sensor was utilized to record the HR information as reference for radar monitoring. In [6, 13, 34], ECG was used as the reference for HR detection. In [6], CO₂ measurement served as the reference of RR detection. In [35], commercial belt sensors and pulse sensors were attached to subject as references.

1.1.6 Detection Accuracy

Table 1.6 summarizes the accuracies of HR/RR detection using different radar systems and signal processing method. In [7], the error rate of 7% was achieved for RR detection of human subject under 1-D body motions. In [9], the detection accuracy of tiny motion generated by actuator was reported to be less than 1 % when motion displacement was set from 0.1 cm to 4 cm, and the motion

Table 1.5 Performance validations of biomedical radars

Research Group	Radar Type	Measurement	Validation Method
Tu et al. [7]	CW	RR	actuator/RR baseline
Li et al. [18]	CW	HR/RR	NA
Gu et al. [31]	CW	HR/RR	shaker/belt sensor/pulse sensor
Kuo et al. [8]	CW	HR/RR	NA
Kao et al. [12]	CW	HR/RR	NA
Chuang et al. [32]	CW	HR/RR	NA
Huang et al. [9]	CW	HR/RR	actuator
Chioukh et al. [10]	CW	HR/RR	oximeter
Wu et al. [11]	CW	HR/RR	NA
Wang et al. [14]	CW	HR/RR	NA
Vinci et al. [13]	CW	HR/RR	ECG
Park et al. [17]	CW	HR/RR	pulse sensor
Baboli et al. [16]	CW	HR/RR	pulse sensor
Wang et al. [33]	CW/Pulse	RR	NA
Schleicher et al. [23]	Pulse	RR	NA
Lazaro et al. [34]	Pulse	HR/RR	ECG
Wang et al. [6]	FMCW	HR/RR	ECG/CO ₂ measurement
Wang et al. [4]	FMCW/CW	HR/RR	NA
Wang et al. [25]	FMCW	RR	NA
Ren et al. [35]	SFCW	HR/RR	Belt sensor/pulse sensor
Liu et al. [29]	SFCW	RR	NA

Table 1.6 Detection accuracies of biomedical radars

Research Group	Radar Type	Measurement	Detection Accuracy
Tu et al. [7]	CW	RR	7%
Li et al. [18]	CW	HR/RR	NA
Gu et al. [31]	CW	HR/RR	NA
Kuo et al. [8]	CW	HR/RR	NA
Kao et al. [12]	CW	HR/RR	NA
Chuang et al. [32]	CW	HR/RR	NA
Huang et al. [9]	CW	HR/RR	<1%
Chioukh et al. [10]	CW	HR/RR	2%
Wu et al. [11]	CW	HR/RR	NA
Wang et al. [14]	CW	HR/RR	NA
Vinci et al. [13]	CW	HR/RR	<1%
Park et al. [17]	CW	HR/RR	<1%
Baboli et al. [16]	CW	HR/RR	NA
Wang et al. [33]	CW/Pulse	RR	NA
Schleicher et al. [23]	Pulse	RR	NA
Lazaro et al. [34]	Pulse	HR/RR	<1%
Wang et al. [6]	FMCW	HR/RR	8%
Wang et al. [4]	FMCW/CW	HR/RR	NA
Wang et al. [25]	FMCW	RR	NA
Ren et al. [35]	SFCW	HR/RR	5.7%
Liu et al. [29]	SFCW	RR	NA

frequency set from 0.2 Hz to 2 Hz. In [10], the average error rate of HR detection when subject 0.5 m away was around 2%. In [34], the HR detection achieved less than 1% error rate when subject was 1 m away from radar transceiver. In [13], the proposed six-port radar demonstrated less than 1% error rate in heart rate detection when subject was approximately 1 m away. In [17], the HR detection error was reported to be less than 1% using CW radar when subject was 1 m away. In [6], the best result of HR detection was obtained when subject at 1 m distance frontal position with a median error around 8 %. In [35], when subject was 0.6 m away from SFCW radar at different orientations, the error rate of HR detection was within 6%.

1.2 Contributions

My major contributions include:

- Improved the UWB pulse radar operating at 1.5-4.5 GHz with phase-locked transmitting signal and enhanced the phase noise performance of the coherent pulse radar system.
- Proposed the phased-based algorithms, i.e., complex signal demodulation and arctangent method, for UWB pulse radar. Extended the UWB pulse radar for real time heart rate monitoring.
- Proposed the state space method for vital signs detection using UWB pulse radar and combined the state space method with phase-based algorithm for higher signal to noise ratio in heart rate detection.
- Extended the UWB pulse radar for heart rate detection of more than one subject.
- Extend the UWB pulse radar for micro-Doppler trajectories extraction from different body joints of walking human subject with the short time state space method.
- Developed and implemented two-channel stepped-frequency continuous wave radar prototype operating at 2-4 GHz, with the first channel covering 2-3 GHz, and the second channel covering 3-4 GHz.
- Developed portable SFCW radar with stack-up configuration and validate its performance with experiments of human vital signs detection.
- Proposed compressive sensing based signal processing to reduce the data acquiring time of SFCW radar and validated the radar performance with experiment of close range localization of a corner reflector.
- Experimentally and numerically compared the performance of SFCW radar and IPPG system in human vital signs detection.

1.3 Organization of the Dissertation

The rest of the dissertation is organized as follows:

Chapter 2 presents the system block diagram of UWB pulse radar with system synchronization and phase-locked transmitting signals. To overcome the

drawbacks of amplitude-based signal processing, phase-based methods of complex signal demodulation and arctangent demodulation have been extended to the signal processing of UWB pulse radar. Moreover, state space method in conjunction with phase-based method is proposed to further enhance the signal to noise ratio in heart rate detection using UWB pulse radar. To evaluate system performance, UWB pulse radar will be used to monitor the chest movement of human subject and periodic motion of actuator. The proposed algorithms will be employed to extract the cardiorespiratory rates of stationary subject and the motion frequency of actuator from reflected and collected pulses. The system performance will be numerically evaluated with commercial reference sensors.

Chapter 3 extends the UWB pulse radar for micro-Doppler signatures extraction of walking human subject with short time state space method. The full-wave electromagnetic scattering model will be utilized to compare the performance of short-time Fourier transform with short time state space method. Based on the subject's height and walking subject, Boulic model will be used as reference of micro-Doppler trajectories of different body joints of walking human subject. The experiments of subject walking towards UWB radar and in an oblique direction to the radar will be conducted. The performance of micro-Doppler trajectories extraction using UWB pulse radar will be numerically evaluated with reference of Boulic model.

Chapter 4 presents the block diagrams and implementation details of SFCW radar, an alternative to UWB pulse radar. Instead of transmitting a frequencies bandwidth simultaneously as pulse radar, SFCW radar steps through the operating frequencies in a stepwise manner. However, SFCW radar suffers from the long data acquisition time, which limits its application and maximum achievable frequency in spectrum. Multi-channel SFCW radar will be proposed to reduce the data acquisition time of SFCW radar. To further reduce the data acquisition time, CS will be employed so that a random subset of frequencies will be transmitted. With a CS based sub-Nyquist sampling algorithm, the target space can be reconstructed accurately and target distance can be precisely localized. Both full-wave electromagnetic simulation and localization experiment of corner reflector will be implemented to evaluate the performance of CS-based SFCW radar.

Chapter 5 presents the implementation of two-channel SFCW radar with stack-up PCB configuration for portable applications. Surface mounted chips are utilized to build the radar transceiver. The mathematical model of SFCW radar in vital signs monitoring has been derived. To evaluate the system performance, the experiments of subject holding breath, breathing normally and at different orientation in front of radar will be conducted and the data will be processed with SSM. All the results will be compared the data collected from commercial contact sensors.

Chapter 6 will briefly review iPPG sensors and radar techniques for non-contact physiological parameters detection. Mathematical models for both iPPG sensor and SFCW radar in vital signs detection will be derived. The signal to noise ratio

of both sensors in cardiorespiratory rates detection will be theoretically estimated. To numerically compare the performance of iPPG sensor and SFCW radar, experiments of heart rate and respiratory rates detection in the same environment will be conducted.

Chapter 7 makes a conclusion of this dissertation and summarizes the contributions of this work, published papers, and future work of the research.

CHAPTER TWO ¹

PHASE BASED METHODS FOR HEART RATE DETECTION USING UWB IMPULSE DOPPLER RADAR

Ultra-wide band (UWB) pulse Doppler radars can be used for non-contact vital signs monitoring of more than one subject. However, their detected signals typically have low signal to noise ratio (SNR) causing significant heart rate detection errors; as the spurious harmonics of respiration signals and mixed products of respiration and heartbeat signals (that can be relatively higher than heart beat signals) corrupt conventional FFT spectrograms. In this chapter, we extend the complex signal demodulation (CSD) and arctangent demodulation (AD) techniques previously used for accurately detecting the phase variations of reflected signals of continuous wave radars to UWB pulse radars as well. These detection techniques reduce the impact of the interfering harmonic signals; thus improving the SNR of the detected vital sign signals. To further enhance the accuracy of the heart rate estimation, a recently developed state-space method (SSM) has been successfully combined with CSD and AD techniques and over 10 dB improvements in SNR is demonstrated. The implementation of these various detection techniques has been experimentally investigated and full error and SNR analysis of the heart rate detection is presented.

2.1 Background

Ultra-wide band (UWB) continuous wave (CW) based radars have demonstrated very promising results for vital sign detection, human gait analysis, fall detection, indoor target localization and so on [4-6, 37]. As an alternative to UWB CW based radars, UWB impulse-radio (IR) radar systems have been widely used in many non-contact scenarios as well [38]-[39]. Definitely, the performance of UWB radars in vital sign detection still needs further improvement, and their capability of tracking more than one subject is really unique.

When a human subject is illuminated by radio waves, reflected waves are modulated by the tiny motion of human thorax. Most of the reflected signal is due to the large step dielectric constant discontinuity at the skin/air interface. Additional reflections could be traced to various scattering of the penetrated signals at the inner organs layers, interfaces [40]. Hence, using 80 GHz radar systems can avoid this penetration problem and provide high SNR in cardio-respiratory motion monitoring, but cannot be used for monitoring objects behind

¹ I worked on this chapter with Hao-fei Wang from Beijing Institute of Technology, K. Naishadham from Georgia Institute of Technology, and Ozlem Kilic from The Catholic University of America.

walls [6]. Additionally, the heartbeat motion causes volume thorax displacement rather than linear motion, and average readings by the radar could be function of both the orientation of the subject and which part of the body is being tracked; hence measured amplitude and phase of these reflected signals could vary accordingly. In [40], UWB multiple-input and multiple-output (MIMO) array is implemented using multi-path/multi-direction signals for micro-motion detection and monitoring real time respiratory and cardiac motions. Multiple receiving antennas are utilized in this array to cancel random torso motions during the experiment as well.

But mono-static or bi-static radar systems focusing on the reflected line-of-sight signals have experimentally demonstrated satisfactory performance as well. In order to provide cardio-respiratory estimation with high accuracy, various UWB radar systems have been proposed [19-22]. In [22], for example, a UWB impulse radar using circularly polarized antennas has enhanced the accuracy for the estimation of cardio-respiratory rates. In [23], a correlation receiver is implemented to avoid direct sampling of the pulses with picosecond precision. The sensing precision is verified by breath-rate measurements. In [24], an integrated UWB transceiver has been developed for respiration rate detection.

Various algorithms have been proposed by researchers to detect respiration and heart rates for UWB radars [41]-[43]. The Fast Fourier Transform (FFT) is widely used for cardio-respiratory rate extraction [33]. In [40], the blind source separation (BSS) is presented to decompose the complex UWB signals and extract the cardiac component. In [34], a Moving Target Indicator is utilized as a filter to suppress harmonics of respiration signals, and in [44] the authors demonstrate that singular value decomposition (SVD) can be utilized to separate the respiration from the non-stationary clutter and enhance the SNR. In [45], higher order cumulant is proposed to reduce the second-order respiration harmonic. Various algorithms and demodulation methods for CW radars have demonstrated satisfactory performance in vital signs monitoring [18]-[46]. For example, the complex signal demodulation (CSD) technique is proposed for the elimination of unwanted torso motions [18]. Arctangent demodulation (AD) together with dc offset calibration greatly improves the accuracy of heart rate detection [17]. In [46] the ensemble empirical mode decomposition is used for heart rate variability analysis.

Focusing on phase information of the reflected radio wave, UWB radars demonstrate promising performance in monitoring human activities. The phase based motion characterization measurement for fall detection by using stepped-frequency CW radar is investigated in [47]. In [48], the two widely used phase-based demodulation schemes for CW radar systems, i.e., CSD and AD, have been extended to UWB pulse radar systems. Similarly, a logarithmic method is proposed in [49] to directly monitor phase variations in heart rate detection. Hence, phase variations due to thorax displacements can be directly detected

with these three techniques using UWB pulse radars.

In this chapter, we focus on CSD and AD for UWB radar systems [48] and derive the analytical framework for these two schemes. Additionally, we experimentally show that phase-based methods outperform direct FFT method by avoiding harmonics and intermodulation products as expected. However, the detected cardiac signal is still very weak due to the small amplitude of heartbeat motion. Hence, state space method (SSM), originally developed for radar target identification and feature extraction [50], [51], is applied in this work to amplify the spectral components of respiration and heartbeat, enabling significant improvement in the performance of CSD and AD methods. The preliminary results of enhanced phased-based methods have been presented in [52]. State space method is a parametric estimation method, which is quite effective in suppressing harmonics and intermodulation frequencies, and improving the SNR, in vital signs estimation [53], [35]. The short time SSM has been successfully applied to UWB pulse radar data for the extraction of human micro-Doppler (μ -D) signatures [54].

In this chapter we concentrate on accurate heart rate detection using UWB radar and arranged as follows. Section 2.2 describes the impulse radar used for measurements. The analytical signal model of the UWB radar is shown. In Section 2.3, CSD and AD algorithms applicable to UWB data are discussed. SSM in conjunction with CSD and AD is briefly introduced as well. In section 2.4, respiration and heart rates are extracted by each algorithm based on UWB data collected from a sedentary subject, and the results are discussed. State-of-the-art in cardio-respiratory detection using UWB radar is briefly summarized in Section 2.5, followed by conclusions in Section 2.6.

2.2 Mathematical Model

The radar prototype used in this work is basically composed of four blocks, a power supply, a transmitter, a receiver and a digital board for data collection [55]. The overall radar block diagram and radar prototype are shown in Figure 2.1 [54], with its components and devices itemized in Table 2.1. The digital board generates a clock signal to feed the pulse generator and synchronize the Agilent 83622B Signal Generator. The output signal of Agilent 83622B serves as the local oscillator for both transmitter and receiver. The receiving antenna can be either a single horn or a SP8T switch-controlled SAR array antenna for monitoring single or multi-objects respectively, depending on the application. The received pulses go through I (in-phase) and Q (quadrature-phase) channels before being collected by the digital board. Note that all the clock signals in the radar system are synchronized. Compared with the radar architecture in [38] and [33], this radar architecture demonstrates higher accuracy in detecting tiny motion. The specific radar parameters are presented in Table 2.2 [56]. This UWB

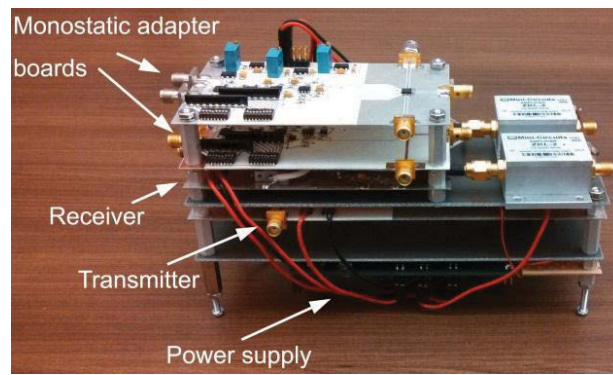
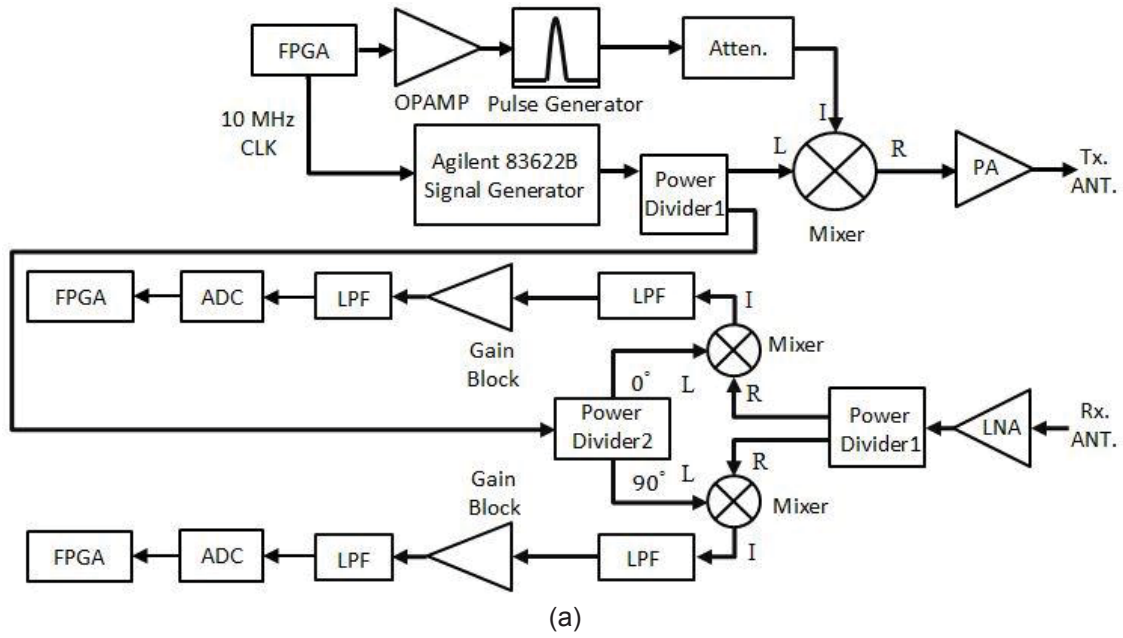


Figure 2.1 (a) Schematic of UWB radar system and (b) prototype.

Table 2.1 Specifications of components used in UWB radar

Block	Manufacturer	Specifications
OPAMP	Texas Instruments	5V output voltage, 500 mA output current
Atten.	Mini Circuits	DC-6 GHz, 12 dB
Mixer	Mini Circuits	0.3-12 GHz, 36 dB LO to RF isolation, 6.5 dB conversion loss
Power Divider1	Mini Circuits	2-4 GHz, 2 way phase difference 0°, 0.4 dB insertion loss
Power Divider2	Mini Circuits	2-4 GHz, 2 way phase difference 90°, 0.4 dB insertion loss
PA	Mini Circuits	2-8 GHz, 30 dB gain, 30 dBm output at 1 dB compression point
LNA	Hittite	1-11 GHz, 1.5 dB NF @ 4 GHz, 16.5 dB gain
LPF	Mini Circuits	DC-1.8 GHz, 0.19 dB insertion loss @500 MHz
Gain Block	Mini Circuits	0.01-2 GHz, 33.5 dB gain, maximum input 13 dBm
ADC	National Semiconductor	16 Bits resolution, 160 MSPS conversion rate

Table 2.2 UWB radar system parameters

Parameter	Value
Bandwidth	1.5 – 4.5 GHz
Pulse Duration	700 ps
PRF	75 Hz
Transmission Power	-28 dBm
Receiver Sensitivity	-65 dBm
USB 2.0 Data Rate	25 MB/s

impulse radar operates over 1.5-4.5 GHz bandwidth. The duration of the transmitted Gaussian pulses is 700 ps and the pulse repetition frequency (PRF) is 75 Hz. The peak transmission power is around -28 dBm and the receiver sensitivity is -65 dBm. The USB between digital board and computer can reach data rate of 25 MB/s.

To identify the spectrum of vital signs, a mathematical signal model for the UWB radar system is developed. This model follows the one proposed in [34] and the signals of I/Q channels can be analyzed. Conventionally, fast-time denotes the range bin and slow-time denotes the pulse number. In this signal model, t indicates slow-time and f is its transformed frequency component; τ indicates fast-time and ν represents its transformed frequency component. As shown in Figure 2.2, the time of arrival (ToA) of collected pulses will be modulated by the periodical motions of respiration and heartbeat. The distance between a subject and radar receiver can be expressed as [34],

$$d(t) = d_0 + m_b \sin(2\pi f_b t) + m_h \sin(2\pi f_h t) \quad (2-1)$$

where d_0 is the distance between receiver and thorax vibration center; m_b and m_h are the amplitudes of respiratory and cardiac motions; f_b and f_h are the respiratory and cardiac rates. The signal received at the receiver front end is [34],

$$r(t, \tau) = \sum_i A_i p(\tau - \tau_i) + A_p p(\tau - \tau_d(t)) \quad (2-2)$$

where $p(t)$ is the collected pulse with a carrier of frequency ν_c ; A_i indicates the strength of multipath components and τ_i is the corresponding time delay, A_p indicates the amplitude of collected pulse, and $\tau_d(t)$ is the ToA [49],

$$\tau_d(t) = 2d(t)/c = \tau_0 + \tau_b \sin(2\pi f_b t) + \tau_h \sin(2\pi f_h t) \quad (2-3)$$

where τ_0 is due to the subject's distance d_0 ; τ_b and τ_h are delays related to the respiratory and cardiac motions, respectively. It is worth mentioning that the multipath components from a static background and stationary body parts will introduce a dc component in the pulses. This dc component can be readily removed with background subtraction or other adaptive filters [43]-[44]. As a result, the signal of interest at the receiver is [49]

$$r'(t, \tau) = A_p p(\tau - \tau_d(t)) \quad (2-4)$$

The intermediate signals of the I/Q branches and their collected (complex) pulse are given by [49]

$$I(t, \tau) = r'(t, \tau) \cdot \cos(2\pi\nu_c \tau) \quad (2-5)$$

$$Q(t, \tau) = r'(t, \tau) \cdot \sin(2\pi\nu_c \tau) \quad (2-6)$$

$$\begin{aligned} y(t, \tau) &= I(t, \tau) - jQ(t, \tau) \\ &= r'(t, \tau) \cdot \exp(-j2\pi\nu_c \tau) \end{aligned} \quad (2-7)$$

Specifically, the FFT of $y(t, \tau)$ in slow time is $Y(f, \tau)$; the FFT of $y(t, \tau)$ in fast time is $Y(t, \nu)$; the 2D FFT of $y(t, \tau)$ is $Y(f, \nu)$. As shown in Figure 2.2, by applying the direct FFT method to slow-time samples, we can identify the frequency of displacements which modulate the amplitude of collected samples. Suppose (2-7) is the Fourier transformed at fast-time $\tau = \tau_0$. The acquired spectrum is as follows [34], [49].

$$Y(f, \tau_0) = A_p \sum_{k=-\infty}^{+\infty} \sum_{l=-\infty}^{+\infty} C_{kl} \delta(f - kf_b - lf_h) \quad (2-8)$$

$$C_{kl} = \int_{-\infty}^{+\infty} P(\nu) J_k(\beta_b \nu) J_l(\beta_h \nu) d\nu \quad (2-9)$$

where $P(\nu)$ is the FFT of pulse $p(t, \tau)$ in τ , $\beta_b = 2\pi m_b$, and $\beta_h = 2\pi m_h$; $J_k(\beta_b \nu)$ and $J_l(\beta_h \nu)$ are Bessel functions. Each intermodulation product is identified by a frequency $f = kf_b + lf_h$ and amplitude C_{kl} . The heartbeat amplitude is very small and the respiration harmonics and intermodulation interference may be dominant in the spectrogram. As a result, the direct FFT method can be erroneous in heart rate detection.

The waveforms collected by FPGA are stored in a matrix R in a discrete form,

$$R[m, n] = r(t_m = mT_s, \tau_n = nT_f) \quad (2-10)$$

where m, n are indices; T_s and T_f are the sampling periods in slow-time and fast-time respectively. The Echo-Planar Spectroscopic Imaging (EPSI) of matrix R is an $m \times n$ matrix, which has the fast-time/range displayed vertically and power spectrum displayed horizontally. Each row of EPSI is obtained by calculating the power spectrum of the corresponding row of R .

2.3 Phase-Based Methods

As presented in Figure 2.3, phase-based methods first implement FFT on each pulse along slow time for direct phase variation extraction. The harmonic and intermodulation interference of respiration are suppressed using the phase

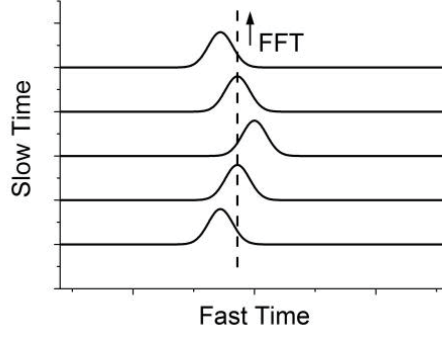


Figure 2.2 Conventional FFT method to detect vital signs

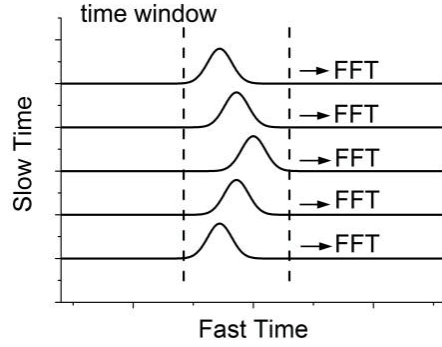


Figure 2.3 Proposed phase based methods.

information because of the linear relationship between phase and time delay. FFT is performed next on the fast time samples of (2.7) [48],

$$\begin{aligned} Y(t, \nu) &= \left[A_p P(\nu) \exp(-j2\pi\nu\tau_d(t)) \right] * \delta(\nu + \nu_c) \\ &= A_p P(\nu + \nu_c) \exp[-j2\pi(\nu + \nu_c)\tau_d(t)] \end{aligned} \quad (2-11)$$

where $*$ represents convolution. For the FFT of each pulse, the computation complexity is minimal at dc compared with any other frequency. As a result, FFT of each pulse at dc is

$$\begin{aligned} Y(t, 0) &= \sum_k \left[I(t, \tau_k) - jQ(t, \tau_k) \right] \\ &= A_p P(\nu_c) \exp[-j2\pi\nu_c\tau_d(t)] \end{aligned} \quad (2-12)$$

It is worthwhile mentioning that synchronization between FPGA clock and carrier frequencies helps in eliminating the jitter in the system for the proposed phase based method. Suppose the jitter in the FPGA clock is $J(t)$, then the signal of interest at the receiver will be

$$r'(t, \tau) = A_p p(\tau - \tau_d(t) - J(t)) \quad (2-13)$$

When the FPGA clock and carrier frequencies are synchronized, there will be phase coherence between these two frequencies, i.e., the two different

frequencies are phase locked. The intermediate signals of //Q channels and collected pulses are,

$$I(t, \tau) = r'(t, \tau) \cdot \cos(2\pi\nu_c(\tau - J(t))) \quad (2-14)$$

$$Q(t, \tau) = r'(t, \tau) \cdot \sin(2\pi\nu_c(\tau - J(t))) \quad (2-15)$$

$$\begin{aligned} y(t, \tau) &= I(t, \tau) - jQ(t, \tau) \\ &= r'(t, \tau) \cdot \exp(-j2\pi\nu_c(\tau - J(t))) \end{aligned} \quad (2-16)$$

When FFT is applied on the fast time samples of (16), we obtain

$$\begin{aligned} Y(t, \nu) &= \left[A_p P(\nu) \exp(-j2\pi\nu\tau_d(t) - j2\pi\nu J(t)) \right] \\ &\quad * \left[\delta(\nu + \nu_c) \exp(j2\pi\nu_c J(t)) \right] \\ &= A_p P(\nu + \nu_c) \exp[-j2\pi(\nu + \nu_c)\tau_d(t)] \\ &\quad \cdot \exp(-j2\pi\nu J(t)) \end{aligned} \quad (2-17)$$

When each pulse is Fourier transformed at dc, (2-17) will become (2-12). In this manner, the jitter existing in the FPGA clock can be eliminated from the demodulated phase information using proposed phase based methods.

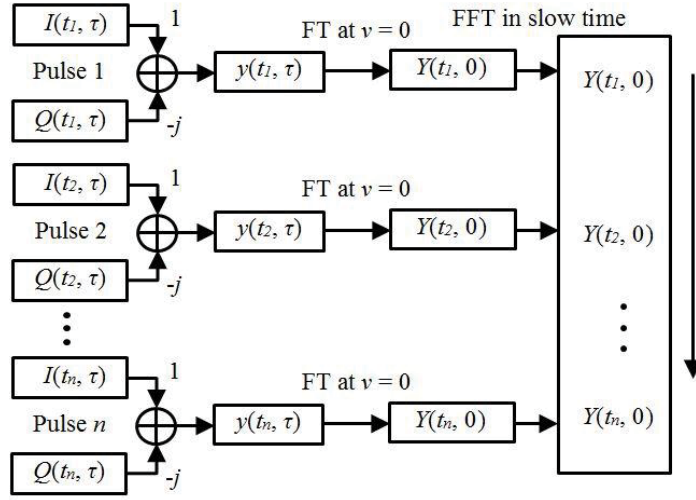
2.3.1 Complex Signal Demodulation

The block diagram for complex signal demodulation is shown in Figure 2.4 (a). When pulse n is Fourier transformed at $\nu = 0$ along fast time, one complex value $Y(t_n, 0)$ will be acquired accordingly. A sequence of complex values is available for spectral analysis. The Fourier series of (2-12) can be represented as

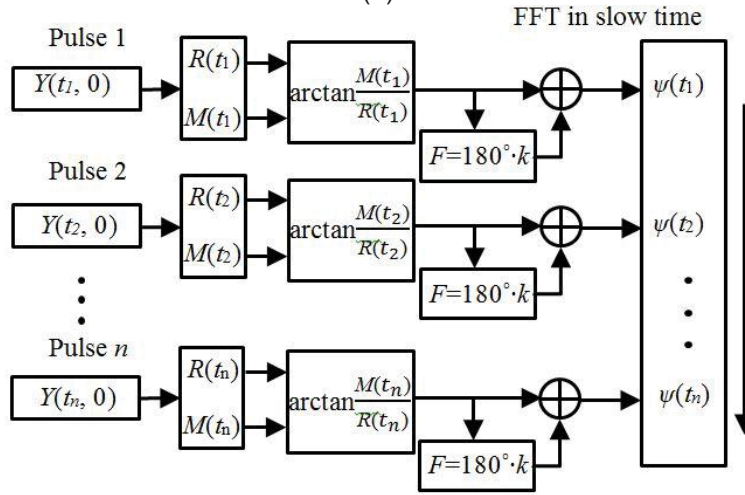
$$\begin{aligned} \frac{Y(t, 0)}{A_p P(\nu_c)} &= \exp\left[4\pi m_b \sin(2\pi f_b t)/\lambda + 4\pi m_h \sin(2\pi f_h t)/\lambda + \phi\right] \\ &= \text{DC}_B - 2j \left[C_{10} \sin(\omega_b t) + C_{01} \sin(\omega_h t) + \dots \right] \cdot e^{-j\phi} \\ &\quad + 2 \left[C_{20} \cos(2\omega_b t) + C_{02} \cos(2\omega_h t) + \dots \right] \cdot e^{-j\phi} \end{aligned} \quad (2-18)$$

$$\begin{aligned} \text{DC}_B &= \text{DC}_{\text{Re}} - j \cdot \text{DC}_{\text{Im}} \\ &= J_0(4\pi m_b/\lambda) \cdot J_0(4\pi m_h/\lambda) \cdot e^{-j\phi} \end{aligned} \quad (2-19)$$

where $\lambda = c/\nu_c$; $\phi = 2d_0\nu_c/c$; $\omega_b = 2\pi f_b t$; $\omega_h = 2\pi f_h t$; $C_{ij} = J_i(4\pi m_b/\lambda) \cdot J_j(4\pi m_h/\lambda)$ are the amplitudes of frequency components, J_n is the first kind Bessel function; DC_{Re} and DC_{Im} are dc components in the real and imaginary parts; DC_B is the desired baseband dc information for the vital sign detection. As shown in (2-18), the available complex values are summation of frequency components and a dc term. The dc offsets introduced by clutter or unbalance between //Q channels will only affect the dc term of $Y(t, 0)$. So the extraction of frequency components of



(a)



(b)

Figure 2.4 Block diagram of (a) CSD; (b) AD for UWB radar system, where $M(t) = \text{Imag}\{Y(t,0)\}$, $R(t) = \text{Real}\{Y(t,0)\}$, F is a multiple of 180° , k is an integer.

interest will not be interfered in the signal processing. Mean subtraction has been used to remove the baseband DC_B as well as any dc offset. However, CSD cannot eliminate higher harmonics with even-orders [18].

2.3.2 Arctangent Demodulation

The block diagram of arctangent demodulation in frequency domain is shown in Figure 2.4 (b). This method is geared towards the calculation of total Doppler shift caused by physiological movement [17]. Based on the complex values obtained in (2-12), arctangent demodulation calculates the total phase of modulated pulse according to

$$\begin{aligned}\psi(t) &= \arctan \frac{M(t)}{R(t)} + F \\ &= \frac{4\pi m_b \sin(\omega_b t)}{\lambda} + \frac{4\pi m_h \sin(\omega_h t)}{\lambda} + \phi\end{aligned}\quad (2-20)$$

where $M(t)$ and $R(t)$ are the imaginary and real components of (2-12) respectively, i.e., $M(t) = \text{Imag}\{Y(t,0)\}$, $R(t) = \text{Real}\{Y(t,0)\}$; F is a multiple of 180° to deal with the wrapping problem when the absolute jumps between consecutive phase elements are greater than or equal to the default jump tolerance of π . Alternatively, differentiate and cross-multiply (DACM) can be used to avoid the wrapping problem, as shown in Appendix A.1 [57].

Since the directly demodulated $\psi(t)$ is a linear combination of respiration and heartbeat signal, harmonics of respiration and intermodulation interference are not involved in the spectrum estimation of vital signs. Furthermore, the amplitude of thorax displacement can be directly detected as well. However, the imbalance introduced by system hardware and dc offset caused by reflection from cluttering may deteriorate the accuracy and needs to be accounted for i.e., (calibrated) first. The imbalance compensation method proposed for CW radar can be used to correct such imbalance and dc offsets in UWB radar data [58] as well. The details are shown in Appendix A.2. The signal processing algorithms (e.g., DACM, imbalance compensation) proposed for phase-based methods previously developed for CW radar system can be applied to UWB radar data too.

2.3.3 State Space Method in Conjunction with CSD and AD

State space method is a parameter estimation algorithm with robustness against noise and efficiency in computation [50]-[51]. In this chapter, state space method is used in conjunction with CSD and AD, so that the heartbeat signal is enhanced in spectrum and precise estimates of cardiac frequency components can be achieved.

For state space method in conjunction with CSD (SSM-CSD), the sequence of complex values acquired by (2-12) is processed with state space method; for

state space method in conjunction with AD (SSM-AD), phase information demodulated using arctangent demodulation is processed with state space method. Details of the SSM have been given in [50] and [35], but will be summarized here for completeness. The steps of SSM-AD are described here and the same procedure is applicable to SSM-CSD as well. Suppose that N phase values are demodulated with arctangent demodulation, i.e., $\psi(n)$, $n = 0, 1, 2, \dots (N-1)$. The state equations are defined in [35] as

$$x(n+1) = Ax(n) + Bu(n) \quad (2-21)$$

$$\psi(n) = Cx(n) + u(n) \quad (2-22)$$

where $u(n)$ and $\psi(n)$ are the input and output respectively. The vector $x(k) \in \mathbb{C}^{P \times 1}$ is the state, $A \in \mathbb{C}^{P \times P}$ is the state transition matrix, while $B \in \mathbb{C}^{P \times 1}$ and $C \in \mathbb{C}^{1 \times P}$ are constant matrices. By taking the z-transform, the transfer function $H(z)$ is obtained according to [35]

$$H(z) = C(zI - A)^{-1} B + 1 \quad (2-23)$$

where I is an identity matrix. The poles and zeros of $H(z)$ are the eigenvalues of A and $(A-BC)$ respectively. As a result, the relation between the impulse response of the model and state-space parameters is defined as [35]

$$\psi(n) = CA^{n-1}B \quad (2-24)$$

The steps in applying SSM to $\psi(n)$ can be summarized below:

(1) First, a Hankel matrix H is formed using $\psi(n)$ as

$$H = \begin{bmatrix} \psi(1) & \psi(2) & \cdots & \psi(L) \\ \psi(2) & \psi(3) & \cdots & \psi(L+1) \\ \vdots & \vdots & \vdots & \vdots \\ \psi(N-L+1) & \psi(N-L+2) & \cdots & \psi(N) \end{bmatrix} \quad (2-25)$$

where L is the nearest integer less than or equal to $N/2$.

(2) This Hankel matrix H is decomposed via singular value decomposition (SVD) into signal and noise subspaces.

$$H = \begin{bmatrix} U_{sn} & U_n \end{bmatrix} \begin{bmatrix} \Sigma_{sn} & 0 \\ 0 & \Sigma_n \end{bmatrix} \begin{bmatrix} V_{sn}^* \\ V_n^* \end{bmatrix} \quad (2-26)$$

where Σ_{sn} and Σ_n are diagonal matrices containing singular values; $(U_{sn} \ U_n)$, $(V_{sn} \ V_n)$ are left-unitary and right-unitary matrices; U_{sn} , Σ_{sn} and V_{sn} are the signal components; U_n , Σ_n and V_n represent the noise components; $*$ denotes the Hermitian operator.

(3) Suppress the noise components in SVD by truncating the matrix H and keeping the dominant components, based on an assumed threshold. The newly obtained matrix with reduced rank is given by

$$\tilde{H} = U_{sn} \Sigma_{sn} V_{sn}^* \quad (2-27)$$

(4) Factorize the truncated matrix as

$$\tilde{H} = \Omega \Gamma \quad (2-28)$$

where $\Omega = U_{sn} \Sigma_{sn}^{1/2}$ and $\Gamma = \Sigma_{sn}^{1/2} V_{sn}^*$ are known as observability and controllability matrices, respectively [50]. The state transition (or system) matrix A is obtained according to

$$A = \left(\Omega_{-rf}^* \Omega_{-rl} \right)^{-1} \Omega_{-rl}^* \Omega_{-rf} \quad (2-29)$$

where Ω_{-rf} is computed by deleting the first row of Ω , and Ω_{-rl} is obtained by deleting the last row of Ω .

(5) The intermediate matrix C (state independent) is acquired from the first row of observability matrix as

$$C = \Omega(1,:) \quad (2-30)$$

(6) The state-independent matrix B is computed as

$$B = \left(\Omega_N^* \Omega_N \right)^{-1} \Omega_N^* \psi^T \quad (2-31)$$

where ψ^T is the transpose of $\psi(n)$ and matrix Ω_N is expressed as

$$\Omega_N = \begin{bmatrix} C \\ CA \\ CA^2 \\ \vdots \\ CA^{N-1} \end{bmatrix} \quad (2-32)$$

(7) The original data $\psi(n)$ can be approximated in terms of state space parameters A , B and C as

$$\psi(n) = CA^{n-1}B, \quad n = 0, 1, \dots, (N-1) \quad (2-33)$$

Eq. (2-33) is formally the state space model that represents the measured sequence $\psi(n)$. Finally, spectral analysis such as Fourier transform can be applied to $\psi(n)$ for vital sign detection. State space method is capable of parametrically characterizing the spectral peaks of heart and respiratory frequencies in the spectrogram, i.e., the amplitude and frequency at each peak in the spectrogram are uniquely identified with the eigenvalues of the state matrix.

2.4 Experimental Results

In order to validate the phase-based methods, two experiments on human subjects and a third one using an actuator have been carried out. In these experiments, horn antennas were used, which were 1.5 m above the ground.

These two antennas were located 50 cm away from each other for adequate decoupling, and the human target was 0.8 m away. The receiving antenna was located closer to the left part of the human subject and it was focused on the amplitude variations of the chest movement of the left heart side, while the subject is facing the antenna. In the first experiment, subject 1 held his breath and sat still in front of the radar system; in the second experiment, subject 2 breathed normally and kept also stationary in front of the UWB radar. The data collected by a reference commercial sensor serves as a reference for heartbeat signal. The six algorithms, i.e., direct FFT, CSD, AD, SSM, SSM-CSD and SSM-AD, are applied to the radar data collected in the experiments and their accuracies as well as their SNRs are evaluated. To judge the performance of different methods, the reference data (ground truth) should be fully predictable and controllable, such as using a periodic object movement enabled by an actuator [9]. Hence in the third experiment, a linear actuator served as the absolute reference to demonstrate the capability of tiny motion detection of our UWB radar. The difference between our readings and the reference rates are obtained and will be noted as deviations. The experiment setups with human subject and actuator are shown in Figure 2.5.



Figure 2.5 Experiment setup with (a) human subject, (b) linear actuator.

2.4.1 Subject 1 Withheld Respiration

When subject 1 held breathing and was stationary, the heartbeat signal was then demodulated directly from radar data with arctangent demodulation, as shown in Figure 2.6. The detected heartbeat signal shows good alignment with the reference in time domain. To clearly show the performance of the six methods for vital sign detection, the detected heart rate with each method using the UWB radar is shown in the subplots of Figure 2.7. The identified heart rate by the reference sensor was 58.0 Beats/Minute. As shown in Figure 2.7 (a), the identified heart rate with direct FFT was 56.7 Beats/Minute, presenting a deviation of 2.1%; as shown in Figure 2.7 (b), (c), complex signal demodulation

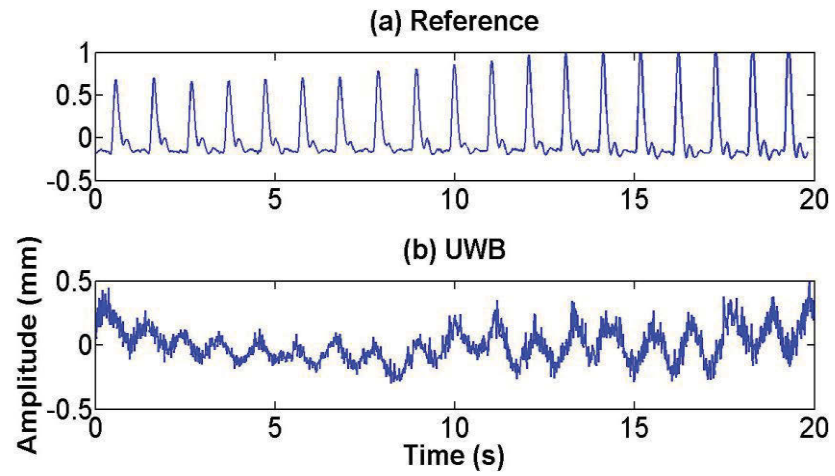


Figure 2.6 Reference and demodulated raw data with AD from right heart side.

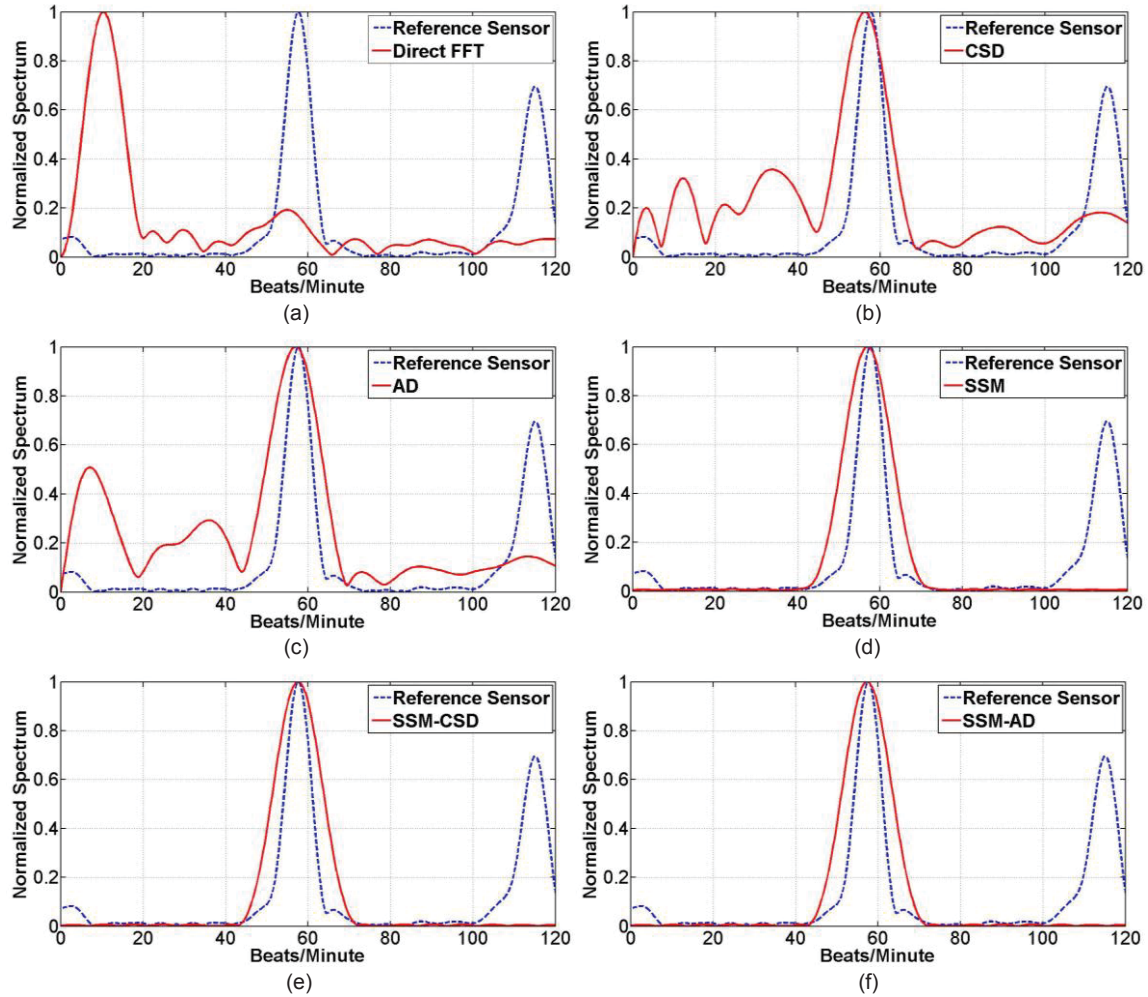


Figure 2.7 When subject 1 held breathing, detected heart rate using (a) reference FFT, (b) CSD, (c) AD, (d) SSM, (e) SSM-CSD and (f) SSM-AD.

as well as arctangent demodulation sensed similar heart rate of 57.1 Beats/Minute, presenting a deviation of 1.5%; as shown in Figure 2.7 (d), the identified heart rate with SSM was 57.0 Beats/Minute, presenting a deviation of 1.7%; as shown in Figure 2.7 (e), (f), the heart rate detected with both SSM-CSD and SSM-AD is the same (57.7 Beats/Minute) and the corresponding deviation is significantly reduced to 0.5%. The detected cardiac rate and deviation with the six methods are listed in Table 2.3. Meanwhile, phase-based methods indicate heartbeat signal much better with clearly visible peaks. Another metric that can indicate the advantages of SSM is SNR, calculated as [45],

$$SNR = 20 * \log \left[\frac{\text{Heartbeat Fundamental}}{\text{SQRT}(\text{Sum}(\text{SQR}(\text{Noise}))/N)} \right] \quad (2-34)$$

where SQRT indicates square root; SQR indicates square; N indicates number of noise samples. The SNR characterizes the ratio of the fundamental frequency heartbeat signal level to the noise level. The noise level is estimated by averaging all non-fundamental spectral components without the dc component, the respiration and heartbeat fundamental frequency and its harmonics. The SNR of detected heartbeat signal with each method is calculated and listed in Table 2.3 as well. It is observed that, arctangent demodulation and complex signal demodulation showed similar performance in SNR in heart rate detection (~ 21 dB). As a general conclusion, all six methods show similar performance in accuracy; while complex signal demodulation and arctangent demodulation outperform the direct FFT method in SNR by at least 10 dB. Meanwhile SSM, SSM-CSD and SSM-AD have higher SNR compared to all other methods, which is over 25 dB higher than that of arctangent demodulation for example. Meanwhile, the use of complex signal demodulation and arctangent demodulation algorithms demonstrated similar SNRs. SSM-CSD and SSM-AD had similar performance in SNR as well.

Table 2.3 Comparison of each method in heart rate (Beats/Minute), deviation (%) and SNR (dB)

Method	Direct FFT	CSD	AD	SSM	SSM-CSD	SSM-AD
HR	56.7	57.1	57.1	57.0	57.7	57.7
Deviation	2.1	1.5	1.5	1.7	0.5	0.5
SNR	8.4	21.2	21.8	46.6	49.9	50.2

2.4.2 Subject 2 Breathed Normally

When subject 2 breathed normally, heart rates detected with these various detection methods are shown in Figure 2.8. Direct FFT method as indicated in [59] detects respiration rate with a deviation of more than 1% compared with the reference sensor. Also all the proposed phase-based methods achieved

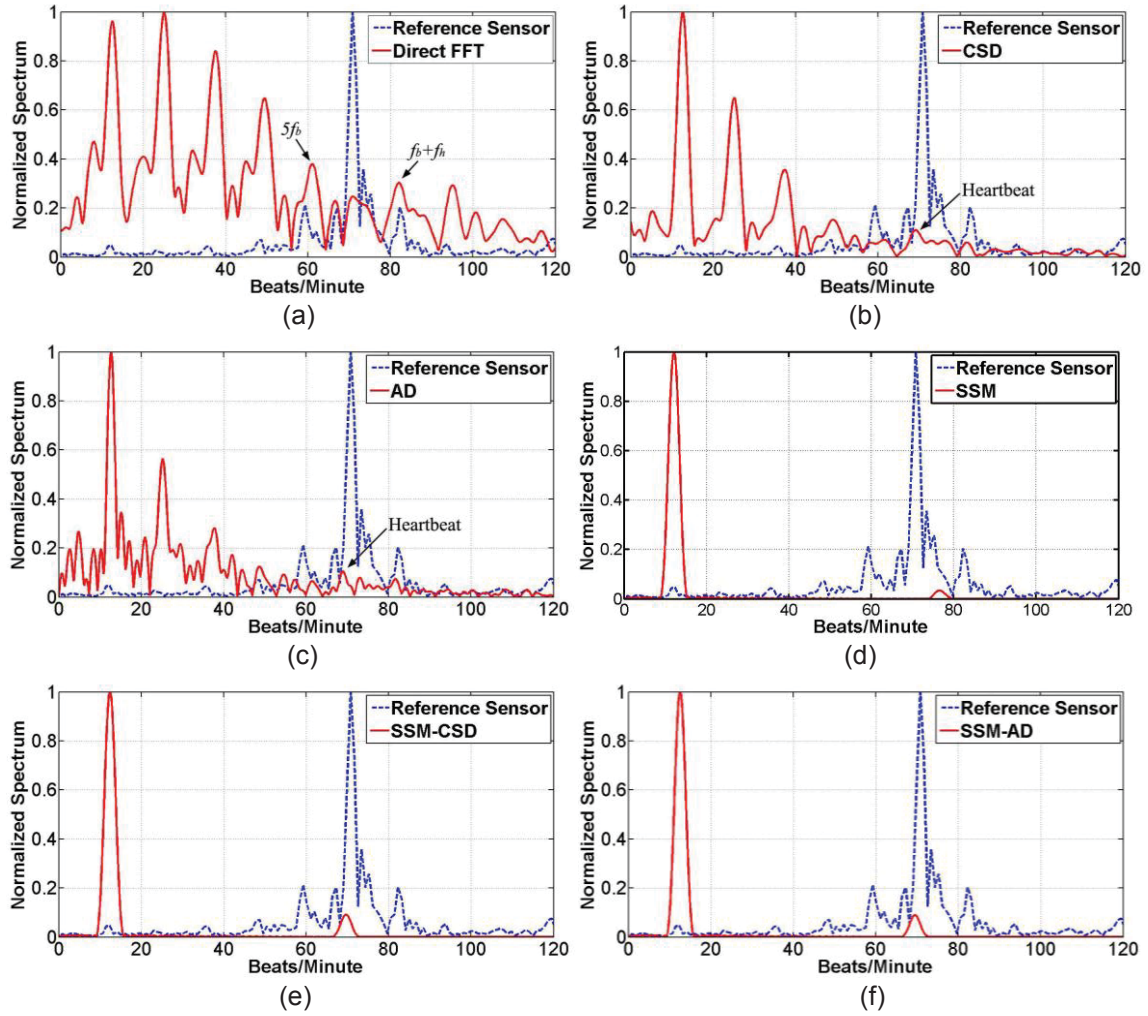


Figure 2.8 When subject 2 breathed normally, detected heart rate using (a) reference FFT, (b) CSD, (c) AD, (d) SSM, (e) SSM-CSD and (f) SSM-AD.

comparable deviations. So we focus here on the heartbeat signal to demonstrate advantages of the newly proposed methods, which were also introduced in [49] as well. The reference heart rate was 70.8 Beats/Minute. As presented in Figure 2.8 (a), the highest two peaks in the frequency range of interest (55 – 100 Beats/Minute) were 60.8 and 82.5 Beats/Minute. The first peak indicates the fifth harmonic of the fundamental respiratory frequency, while the second peak, i.e., 82.5 Beats/Minute, was the intermodulation between respiration and heartbeat signals, i.e., $f_b + f_h$. As a result, the direct FFT method could not identify the heartbeat signal due to the strong harmonic and intermodulation interference. As shown in Figure 2.8 (b), (c), both CSD and AD showed the same accuracy in heart rate detection. The detected heart rate with these two methods was 69.0 Beats/Minute and the corresponding deviation was 2.6 %. Note that, even though the level of noise interference was relatively high, heartbeat signal was successfully extracted. In Figure 2.8 (d), the identified heart rate with SSM was 68.4 Beats/Minute, presenting a deviation of 3.7%. In Figure 2.8 (e), (f), the heart rate detected with SSM-CSD and SSM-AD was 69.6 Beats/Minute, showing a deviation of only 1.7%. The noise level was greatly suppressed and heartbeat signal was clearly visible in the spectrum.

The sensed heart rates, deviations and SNRs are listed in Table 2.4. When the subject breathed normally the heartbeat signal detected with direct FFT method was masked by harmonics and intermodulation products, hence it was not listed in Table 2.4. CSD and AD had the same SNR in heartbeat monitoring. SSM demonstrated similar performance in SNR to SSM-CSD and SSM-AD. In summary, phase based methods and SSM showed same level of accuracy, and application of SSM-CSD and SSM-AD led to an improvement of 10 dB at least in SNR over the CSD and AD methods.

Table 2.4 Comparison of each method in heart rate (Beats/Minute), deviation (%) and SNR (dB)

Method	CSD	AD	SSM	SSM-CSD	SSM-AD
HR	69.0	69.0	68.4	69.6	69.6
Deviation	2.6	2.6	3.7	1.7	1.7
SNR	20.7	20.4	27.9	32.4	32.6

2.4.3 Actuator Experiment

To imitate the torso motions due to human heartbeat, the actuator was programmed to perform sinusoidal movements. A foil plate was mounted on the translational stage to reflect incident wave from the UWB radar system. The actuator was placed 1 m away in front of the radar. The amplitude of displacement was 1 mm and the movement frequency was 1 Hz. The actuator motion was measured and demodulated from collected pulses with phase based algorithms and the extracted spectrums are demonstrated in Figure 2.9. After coherent combination of all the energy of range bins traversed by the actuator

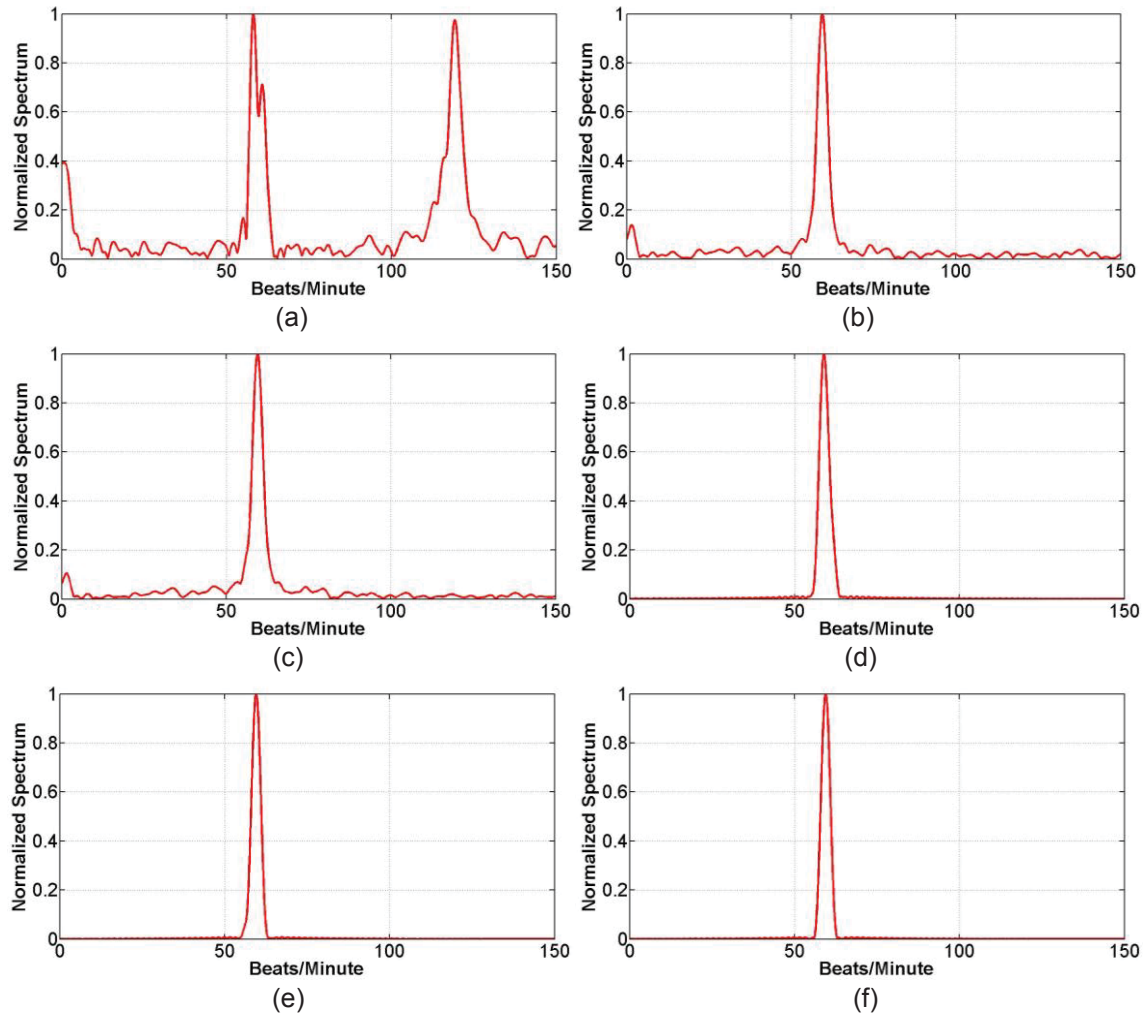


Figure 2.9 Detected actuator movement frequency using (a) reference FFT, (b) CSD, (c) AD, (d) SSM, (e) SSM-CSD and (f) SSM-AD.

and implementation of direct FFT, the acquired spectrum is shown in Figure 2.9 (a). The second harmonic of the presented frequency is comparable to the fundamental frequency. The obtained motion frequencies using phase based methods and their enhanced counterparts are presented in Figure 2.9, all indicating a deviation of less than 1%. Moreover, SSM, SSM-AD and SSM-CSD demonstrate better performance in SNR. These results validate the accuracy of our algorithms for detecting vital signs, and are consistent with commercial sensors previously used to evaluate measurement errors in these experiments.

2.4.4 Block Processing SSM

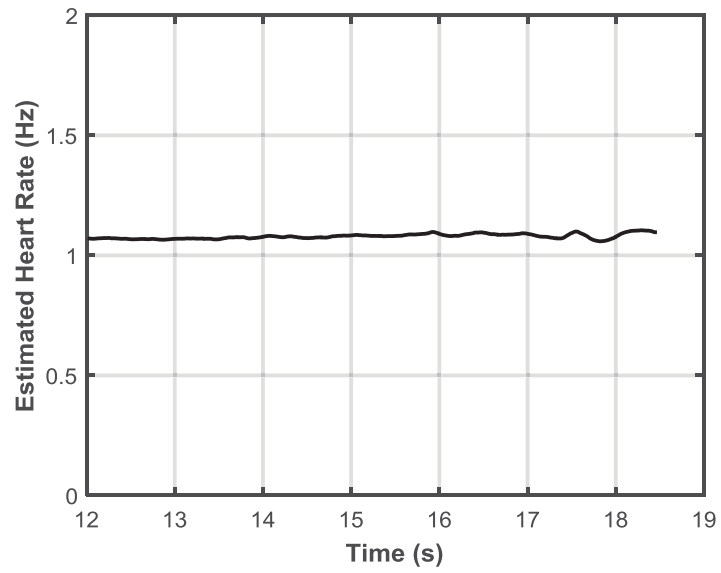
To evaluate the performance of continuous monitoring, a long data set of 18.5 s duration (1386 samples) collected on the human subject is considered. SSM is applied sequentially to blocks of 900 samples with each block after the first one shifted forward by one sample to generate contiguous blocks until the last block of 900 samples is reached. The estimation of the vital signs begins by passing the block of first 900 samples that cover a time duration of 12 s to the SSM. As time evolves, blocks of 900 samples that share 899 samples with their two immediate neighbors are sequentially fed to the SSM with a model order of 10 to extract the vital signs until the entire 18.5 s are covered. Figure 2.10 (a) depicts block-processed estimates of the heart rate signifying a solid trend of about 1.1 Hz for all the blocks, lying within 3% accuracy compared to the reference.

Next, the heart rate error is computed for each estimate with respect to the reference of 1.073 Hz to form an error vector Δv_h containing entries arranged in ascending order of the error. A cumulative distribution function (CDF) is then formed by computing percentage of the entries in Δv_h smaller than each one of its individual elements. It is gratifying that the errors depicted in the CDF plot in Figure 2.10 (b) are indeed very small, reaffirming that about 98% of the heart rate estimates show error less than 0.03 Hz (or within 3% of the reference).

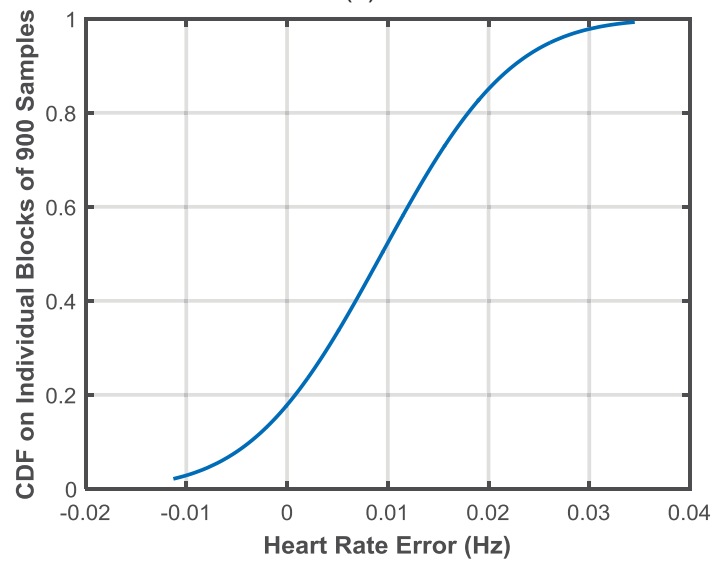
Fig. 2.11 (a) depicts the block-processed estimates of the respiration rate for the entire 18.5 s duration, demonstrating reasonably good corroboration between the estimates and the reference respiration rate of 0.28 Hz measured on the subject. As seen in the CDF plot of Figure 2.11 (b), 92% of the blocks processed produce errors lying within 7% of the reference (or within 0.025 Hz). Due to the subject's body movement and the proximity of the respiration rate to DC, a transient-type phenomenon induces larger errors in the estimates of respiration rate for time intervals that fall below 12.5 s.

2.4.5 Two Subjects Breathed Normally

In the fourth experiment, two subjects were sedentary 0.6 m and 0.9 m away from the receiver, and breathing normally. The experiment setup is shown in Figure 2.12. The back-projection algorithm was utilized to achieve a high resolution in subject localization as indicated in Figure 2.12 (b). The phase-based method was used to identify the vital signs of the two subjects. As shown in

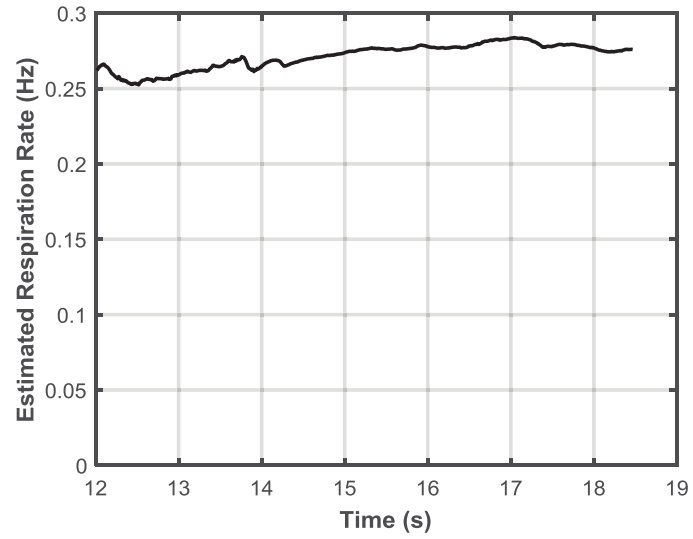


(a)

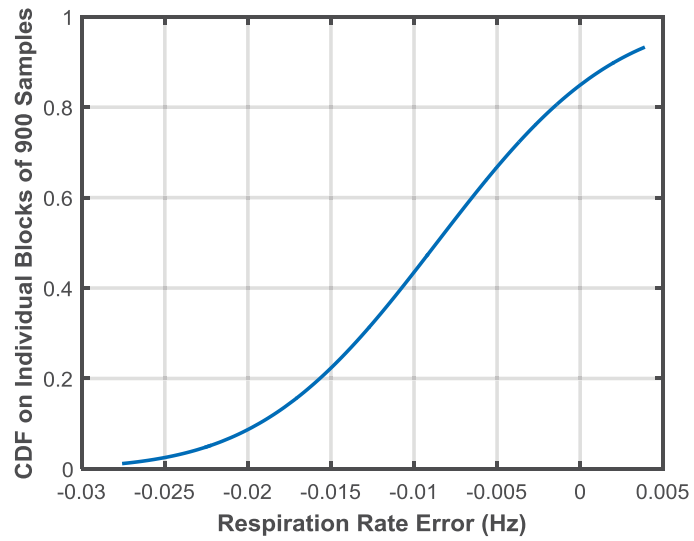


(b)

Figure 2.10 (a) Heart rate estimates obtained using block-processing SSM. (b) Cumulative distribution function of the heart rate.



(a)



(b)

Figure 2.11 (a) Breathing rates estimated using block-processing SSM. (b) Cumulative distribution function of the respiration rate.

Figure 2.13, the detected respiration and heart rates for subject 1 using the commercial references were 13.45 and 73.66 Beats/Minute respectively. The respiration and heart rates obtained using the UWB radar were 13.45 and 75.34 Beats/Minute, showing an error of 2.28 % for heart rate detection. For subject 2, the detected respiration and heart rates from the references were 15.30 and 77.36 Beats/Minute, as shown in Figure 2.14. The respiration and heart rates acquired using the UWB radar were 15.30 and 79.57 Beats/Minute, showing an error of 2.85 % for heart rate detection.

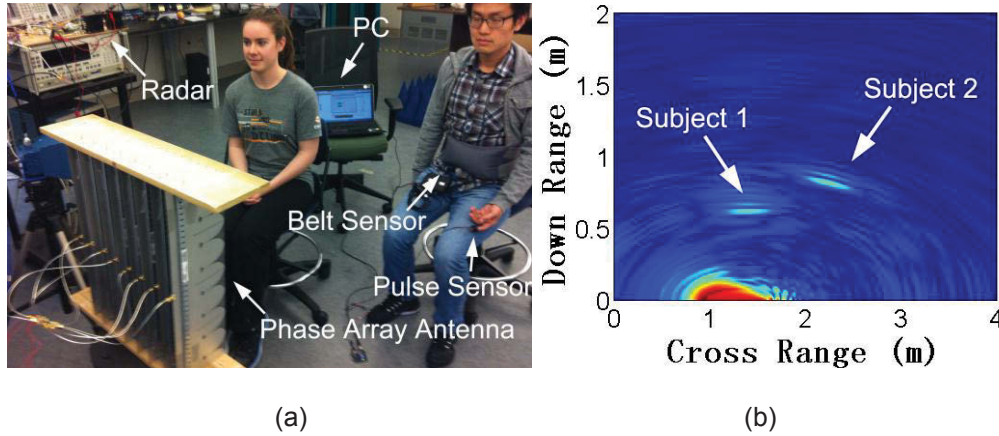


Figure 2.12 (a) Experiment setup. (b) Localization with UWB system.

2.5 Discussion

In the above two human subject experiments, we presented the performance of direct FFT method, SSM and phase-based methods, focusing on their accuracy and SNR in vital sign detection. Note that zero padding is utilized in the spectrum estimation so that the frequency resolution is less than 0.01 Hz which is very adequate for accurate heart rate estimation.

1) When the subject held breath, all six methods demonstrated comparable accuracy in heart rate detection; when the subject breathed normally, the detected heartbeat signal by the direct FFT method was masked by the respiration harmonics and mixed intermodulation products.

2) Both CSD and AD showed a similar SNR performance in our experiments, as shown in Figure 2.15. Practically, in applying these phase-based methods it is essential to apply a window function, i.e., Hamming window before performing their FFTs. Otherwise, the resulting spectrum would suffer from leakage if the signal is not perfectly periodic in FFT's finite length. Figure 2.16 shows the results of vital sign detection for breathing subject using complex signal demodulation with and without a Hamming window. It is obvious that energy is more dispersed in the spectrum when the complex values of the spectrum are not multiplied by a Hamming window. The dispersed result makes it more difficult

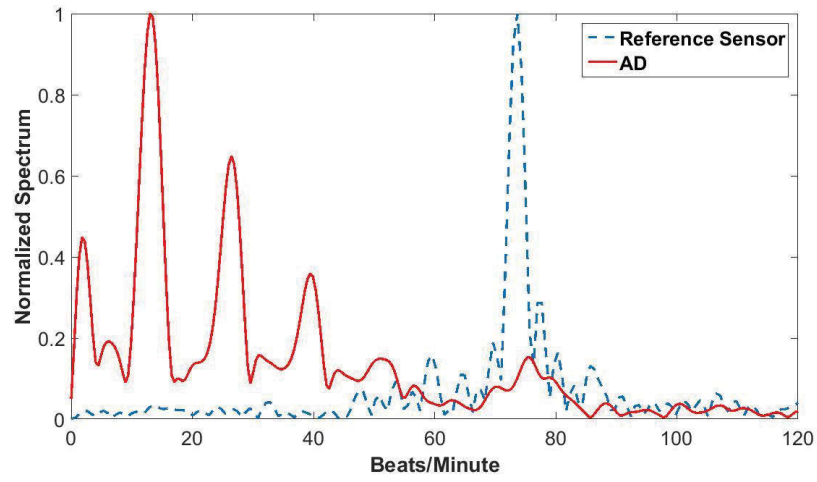


Figure 2.13 Heart rate detection of subject 1 with arctangent method.

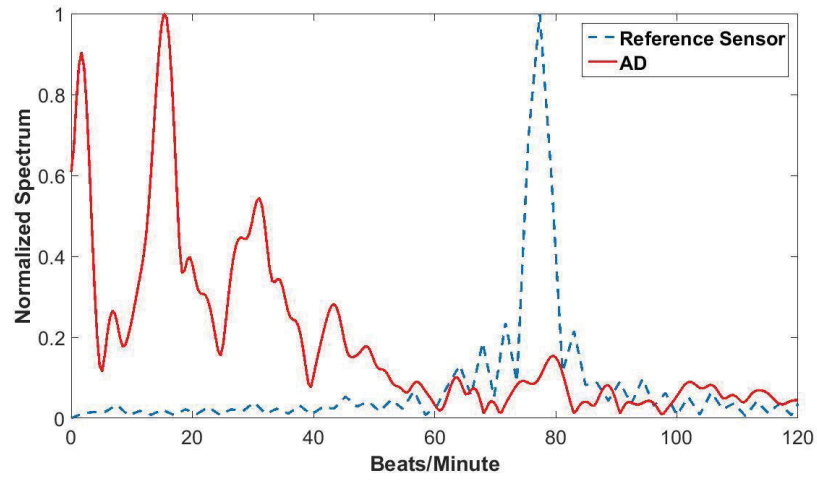


Figure 2.14 Heart rate detection of subject 2 with arctangent method.

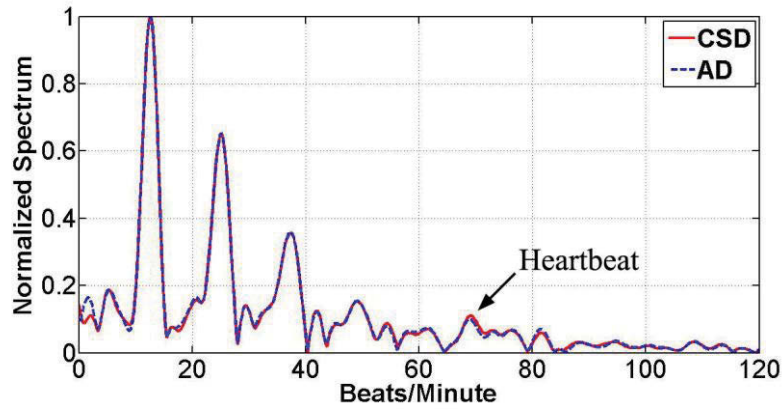


Figure 2.15 In the second experiment, detected heart rate using CSD and AD.

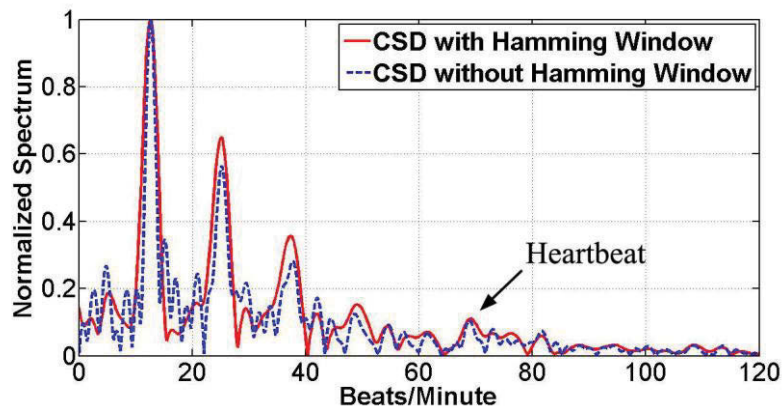


Figure 2.16 In the second experiment, detected heart rate using CSD with hamming window and CSD without Hamming window.

Table 2.5 Comparison between CSD and AD

	Pre-processing	Advantage	Application	Enhanced Version
CSD	windowing	lower computation cost	spectrum	SSM-CSD
AD	windowing, dc offset calibration	less harmonics	spectrum, amplitude	SSM-AD

to identify the respiration and heart rates.

CSD and AD are compared in Table 2.5, where windowing functions were necessary for both demodulation methods. Arctangent demodulation eliminates nonlinear modulation in phase and can demodulate the amplitude of tiny displacements, while it requires dc bias calibration. Fortunately, the dc bias calibration methods proposed for CW radar can be utilized here, e.g., dc estimation method proposed in [18], or dc imbalance correction method proposed in [58]. The dc imbalance correction method for UWB radar is shown in Appendix A.2 in details. Complex signal demodulation is free of the dc offset problem and has lower computation cost, while it is subjected to even-order harmonics as indicated in (2-18), and consistent with [18]. Though these two methods are robust in suppressing harmonics interferences, they still need to be improved in SNR, as shown in the second experiment. State space method is a parametric estimation algorithm which works in conjunction with CSD and AD to address the issue of SNR. SSM enhanced methods, SSM-CSD and SSM-AD, render low deviation in respiration and heart rates estimation as well as high SNR.

Table 2.6 provides a summary of methods used for vital sign detection utilized by various other groups. In [19-24], variety of UWB radar systems types is proposed and the direct FFT method is used for vital sign identification. In [40], multiple receiving channels are utilized to avoid artifacts due to body motions. By calculating the blind source separation of channels with low variation, a heartbeat signal is extracted with sharp trailing slopes and good match with high resolution ECG. In [41], a hidden Markov model (HMM) is developed for respiration tracking using more than one UWB sensor. In [36], the wavelet transform and filter banks are proposed for physiological monitoring. The heart movement is detected with a Chirp Z-Transform (CZT) computing the spectrum, a deviation of 5% was demonstrated. With the help of MTI suppressing harmonics a deviation of 2.4% was realized in [34] for heart rate detection when subject breathed normally. Higher order cumulant (HOC) proposed in [45] outperforms direct FFT in SNR of vital signs detection. For References [42], [43] and [44] algorithms are presented for non-line-of-sight (NLOS) vital signs monitoring. In [42], SVD is utilized to de-noise signal and Hilbert-Huang transform (HHT) is used to extract human vital sign frequencies. In [43], a dual-frequency UWB radar is developed to adaptively eliminate the non-static clutter for respiration rate detection in through-wall scenarios. Respiratory motion detection (RMD) involving SVD, threshold and target classification is developed in [44] for detection of trapped victims. To the authors' best knowledge, it is the first time that phase-based methods were proposed to demodulate heartbeat signal for UWB radar system in [48]. SSM enhanced methods further improve the SNR for heart rate detection by over 10 dB. The advantage of a UWB radar system to process the phase information in the spectral estimation of vital signs is the exclusion of respiration frequency harmonics and their intermodulation interference. Additionally, due to the inherent ultra-wide bandwidth, the pulse signal of UWB radar is narrow in the time domain, and a high range resolution can be achieved. As a result, UWB

Table 2.6 Current methods to detect respiratory rate (RR) and heart rate (HR) for UWB impulse Doppler radar

Research Group	Method	Vital Signs	Reported HR Deviation	Operating Range	Technique
This work	CSD	RR/HR	2.6%	0.8m	Assembly
This work	AD	RR/HR	2.6%	0.8m	Assembly
This work	SSM	RR/HR	3.7%	0.8m	Assembly
This work	SSM-CSD	RR/HR	1.5%	0.8m	Assembly
This work	SSM-AD	RR/HR	1.5%	0.8m	Assembly
Bernardi et al. [19]	FFT	RR	NA	0.6m	Assembly
Lai et al. [20]	FFT	RR	NA	2m	Assembly
Wang et al. [21]	FFT	RR	NA	0.5m	CMOS
Chan et al. [22]	FFT	RR/HR	$\leq 3\%$	3m	Assembly
Schleicher et al. [23]	FFT	RR	NA	0.25m	Assembly
Zito et al. [24]	FFT	RR	NA	0.4m	CMOS
Hilger et al. [40]	BSS	RR/HR	NA	1m	Assembly
Nijsure et al. [41]	HMM	RR	NA	3m	Assembly
Baboli et al. [36]	wavelet	RR/HR	5%	1m	Assembly
Lazaro et al. [34]	MTI/CZT	RR/HR	$\leq 2.4\%$	1m	Assembly
Xu et al. [45]	HOC	RR/HR	NA	1.8m	Assembly
Li et al. [42]	SVD/HHT	RR/HR	NA	NLOS	Assembly
Li et al. [43]	ACC	RR	NA	NLOS	Assembly
Nezirovic et al. [44]	RMD	RR	NA	NLOS	Assembly

radar can clearly receive the reflected pulses from human body at specified distance range (spatial gating) and totally rejecting clutter from other distances. In this manner, the signal to noise ratio for the UWB radar in phase demodulation is significantly improved.

2.6 Conclusion

A UWB impulse radar is presented with all clock signals synchronized, which guarantees the accuracy of tiny motion detection. Then a signal model for the UWB radar system with I/Q channels is introduced and demodulation algorithms originally developed for CW radar have been extended to the UWB radar data analysis. Experiments using low power UWB radars demonstrated that complex signal demodulation and arctangent demodulation are capable of avoiding harmonics and mixed frequency products of respiration and heart rates. Meanwhile, SNR of heart rate detection has been enhanced using SSM-CSD and SSM-AD, where improvement of over 10 dB has been achieved. It is important to recognize that UWB radars can be utilized for multi-target detection and tracking as well with similar performance when combining either CSD or AD algorithms.

CHAPTER THREE ²

SHORT TIME STATE SPACE METHOD FOR MICRO-DOPPLER IDENTIFICATION OF WALKING SUBJECT USING UWB IMPULSE DOPPLER RADAR

In this chapter, ultra-wideband (UWB) Doppler radar signatures from walking human subjects are processed with state space method (SSM); and micro-Doppler (μ -D) features are extracted for gait analysis. To clearly distinguish μ -D signatures of different body joints for the subjects, the SSM, originally developed for characterization of radar target signatures and sensor fusion, is applied on a sliding short-time window to enhance resolution in a dismount feature extraction. This application of SSM to sliding short-time data, termed herein as short-time SSM (STSSM), is validated with a full-wave electromagnetic (EM) simulation of a walking subject using the Boulic model that represents the human kinematics. The EM scattering model is then utilized to compare the performance of short-time Fourier transform (STFT) with STSSM. The experimental results show that STSSM can be successfully applied to identify multiple μ -D trajectories in real experimental data, thus demonstrating the capability to positively identifying human motions even in a low signal-to-noise ratio (SNR) environment.

3.1 Background

There has been concentrated effort by many scientists to develop various algorithms and models to describe human movements, such as Boulic model [60]. Large amount of data has been produced by simulating the mechanics of various body-parts, including muscles, bones and joints. Simulation and measurement of various joint movements help to identify abnormalities in individuals with cerebral palsy, stroke, osteoarthritis and Parkinson's disease, for example, they can be used to develop a full understanding of normal motion and establish a scientific basis for correcting abnormalities; however, it is still a major challenge.

Several radar technologies have been applied to extract various micro-Doppler (μ -D) features of human subjects including the impulse radar [33], the continuous-wave (CW) radar [61-64], the frequency-modulated CW (FMCW) radar [4, 65], and the pulse compression radar [66]. CW radar system, however, does not provide range information of subjects, which limits its application. Although, CW radar using dual frequency is capable of direction-of-arrival (DOA)

² I worked on this chapter with Nghia Tran, Ozlem Kilic from The Catholic University of America, Hao-fei Wang from Tsinghua University, Krishna Naishadham from Georgia Institute of Technology and Jean E. Piou from Wayland, MA.

estimation of targets, it is subject to multipath effects. On the other hand, it is quite expensive and complicated to implement wideband FMCW and pulse compression radars. Alternatively, UWB impulse Doppler radar has numerous advantages, such as relatively low prototype cost, less power consumption, and high-resolution range profile (HRRP) using a range-time-frequency representation. Hence, UWB radar has been utilized here to extract μ -D features. There are various algorithms to extract μ -D signatures from radar signals and provide valuable information of human motion dynamics. Most of these methods are based on time-frequency analysis of radar echoes. For example, the high-resolution time-frequency method, e.g. short-time Fourier transform (STFT), is widely used in human gait analysis and motion pattern classification [39, 67-71]. Many other transforms or methods have been proposed, as well, including Hilbert-Huang transform [72], reassigned joint time-frequency transform [73], wavelet transform [74], k-nearest neighbor (k-NN) classifier [75], artificial neural network [76], support vector machine (SVM) [77], probabilistic principal component analysis (PPCA) [78], and so on.

To gain elaborate information on human motion, it is necessary to identify the motion of specific limbs and body joints and clearly distinguish their corresponding μ -D signatures in their spectrogram. Typically, a walking human subject can be modeled by sixteen body joints [60], and the backscattered radar signal from human body involves multiple μ -D trajectories due to these various body joints. Fortunately, many algorithms have been proposed to improve the resolution of these trajectories that are usually depicted in time versus frequency map or spectrogram and detail the monitored subject's status. In [79], for illustration, a novel short-time iterative adaptive approach (ST-IAA) is used to obtain a more accurate spectrogram. In [80], nonlinear least squares (NLS) and an expectation-maximization algorithm have been used to decompose human signatures into the response of the constituent body parts. In [81], an empirical mode decomposition method is used to produce a unique feature vector from human μ -D signals and SVM is used to classify the subjects' motion. An application comprising of a modified high-order ambiguity function (MHAF) with the CLEAN algorithm is proposed to extract μ -D features based on their scattering centers (body joints) in [82].

Meanwhile, a state space method (SSM) has been successfully used in characterization of radar target, radar sensor fusion, and electromagnetic wave-based target feature extraction from polarimetric radar measurements with low signal-to-noise ratio (SNR) [50, 51]. The SSM has the capability of separating backscattered signal components based on system poles; and their amplitudes specific to a target scattering feature, or in the case of biomedical radar, specific to the Doppler signature of a particular body joint. Hence recently, SSM has been used in biomedical radar applications to retrieve accurate estimation of respiratory and heartbeat frequencies from Doppler signatures, without producing the inter-modulation products that typically plague FFT-based spectrograms [53]. Other examples of SSM implementation include computation of fundamental gait

frequencies using simulated radar data [83], and image resolution enhancement in nuclear magnetic resonance (NMR) spectroscopy [84]. In this chapter, we apply SSM to short-time windowed segments of sliding data sequences generated by FFT of each pulse along the fast time of the backscattered returns from UWB radar, and extract human gait characteristics. For convenience, this modified SSM is referred to in the sequel as short-time state space method (STSSM).

In this chapter, Section 3.2 presents the STSSM algorithm; it is based on the combination of the original SSM and a sliding window function that are used to identify specific μ -D components of each scattering body joint from UWB data. An empirical analytical model of a human walking kinetics is discussed in section 3.3. A full-wave electromagnetic scattering model for the human body in motion is presented in section 3.4. This model is employed in section 3.5 to simulate the backscattering of CW radar signals from a walking subject [85]. STFT and STSSM methods are compared in processing data of the scattering model. Finally, in section 3.6, STSSM is applied to UWB signals reflected from different walking subjects in radial and oblique directions. Its performance validates that the μ -D signatures generated by different body joints in human motion can be successfully distinguished.

3.2 Short time state space method for UWB Impulse Radar

The UWB radar described in [33] is used to collect data from human subjects. Data from one channel is saved in a data cube denoted by $\mathbf{s}(\mathbf{k}, \mathbf{n})$, where $k = 1, 2, \dots, K$ represents fast time or range index, and $n = 1, 2, \dots, N$ denotes the slow time or cross-range index. HRRP can be utilized to show the real-time location of the subject or detect the walking path of a human target; it is widely used in through-barrier detection [39], [86]. HRRP at time n_0T can be directly obtained from $\mathbf{s}(\mathbf{k}, \mathbf{n}_0)$, where T is the pulse repetition time. Meanwhile, range bins traversed by a subject are unraveled by HRRP. Upon applying time-frequency analysis to these range bins, μ -D signatures of a target can be readily extracted. Alternatively, we can first apply FFT to each reflected pulse along fast time and acquire its corresponding spectrum. In this manner, data cube $\mathbf{s}(\mathbf{k}, \mathbf{n})$ is transformed into $s'(\mathbf{m}, \mathbf{n})$ in frequency domain, where $m = 1, 2, \dots, M$ represents fast-time frequency index. A conventional joint time-frequency transform, i.e. STFT, can be applied to the slow-time signal $s'(\mathbf{m}_0, \mathbf{n})$, where m_0 indicates frequency in the fast-time spectrum of each reflected pulse. The spectrum illustrating signal variation in both time n and slow-time frequency f domains is calculated as

$$s(n, f) = \left| \sum_{p=-\infty}^{\infty} s'(p) g(p-n) e^{-jpf} \right|^2 \quad (3-1)$$

where $s'(n)$ denotes slow-time samples for a selected fast-time spectrum bin, and $g(n)$ is the sliding window function.

Instead of using STFT, a parametric signal analysis method, i.e. STSSM, is considered for μ -D feature extraction in low SNR situations. Consider the data cube $s'(m, n)$ after FFT of each pulse, where $m = 1, 2, \dots, M$ represents fast-time spectrum, $n = 1, 2, \dots, N$ denotes slow time index. When a subject is located at range bin m_0 , the data sequence to be processed is

$$y(n) = s'(m_0, n) \cdot g(n - p), \quad p \in (-\infty, \infty) \quad (3-2)$$

where $g(n-p)$ is the sliding window function centered at p . The data sequence $y(n)$ could be modeled as,

$$y(n) = \sum_{i=1}^Q a_i e^{-(b_i + j \frac{4\pi}{c} r_i') f_n} + w(n), \quad n = 0, 1, \dots, (N-1) \quad (3-3)$$

where $y(n)$ is composed of Q complex sinusoidal signals corrupted by noise $w(n)$ and has N time-domain samples which are spaced at pulse repetition frequency (PRF). The parameters a_i and b_i represent amplitude and damping factor related to i^{th} scattering body joint, r_i' and c denote the target range-rate and speed of light respectively, the n^{th} frequency component is associated with the carrier frequency f_0 as $f_n = f_0 + (n-1) \cdot \Delta f$, and Δf is PRF.

The poles in (3-3) contain the information of target motion and are critical for signal component separation in μ -D feature extraction. The poles represent the roots of the denominator of the transfer function of an autoregressive moving average (ARMA) derived from the state space equations [50], [51]. As a result, an alternative input-output relationship for (3-1) is given by

$$\begin{aligned} x(n+1) &= A \cdot x(n) + B \cdot w(n) \\ y(n) &= C \cdot x(n) \end{aligned} \quad (3-4)$$

where $w(n)$ is the input and $y(n)$ is the output; $x(n) \in \mathbb{C}^{Q \times 1}$ is the state, $A \in \mathbb{C}^{Q \times Q}$ is the state transition matrix, $B \in \mathbb{C}^{Q \times 1}$ and $C \in \mathbb{C}^{1 \times Q}$ are constant matrices. By following the steps of SSM from (2-23) to (2-33), we can acquire the estimated data sequence after signal component separation, i.e., $\hat{y}(n)$. Then, spectral analysis such as Fourier transformation could be applied to $\hat{y}(n)$ for identification of μ -D trajectory from each body joint. It is worthwhile mentioning that by computing the eigenvalues of state transition matrix A , we can acquire the poles of the model and thus the corresponding frequency components in the data sequence $y(n)$.

3.3 Human Walking Model

To model human motion kinematics, we utilize an analytical model extracted from empirical data, namely, the well-known Boulic model [60]. According to this model, human walking motion is modeled by cycles with constant translational

velocity. There are two inputs to this model – velocity and height of the human. From these inputs, the human body phantom can be created using 16 joints between its 17 body parts, which are identified as the head and the lines between the joints, as depicted in Figure 3.1 (a). Furthermore, the fundamental spatial and temporal motion characteristics (i.e. the length of the walking cycle, L_c , and the duration of the walking cycle, T_c) are also determined from these inputs. The time-dependent translation and rotation of each joint on a human body are then calculated using these two parameters, i.e. L_c and T_c . Figure 3.1 (b) shows the radial speeds of different human body parts for one walking cycle, $T_c = 2.3$ s, created by the Boulic model for a human of height 1.72 m, walking at 0.33 m/s speed. We can see that the lower parts of the legs such as the feet and the ankles achieve the maximum μ -D frequency at around 30 Hz, while the torso and hands oscillate slightly around the velocity of the translational movement of the human. The motions of the left and right parts of human body are observed to be periodic.

3.4 Full Wave Electromagnetic Model for a Human in Motion

In this section, Method of Moments enhanced with Fast-Multipole-Method (MoM-FMM) is utilized as an efficient way to calculate the scattered fields from a walking human. Mutual coupling and ground effects are incorporated. Even though the mesh sizes on curved surfaces can be larger than those in finite difference time domain (FDTD), we still can maintain high accuracy [87].

The MoM-FMM technique focuses on the grouping concept (aggregation) of mesh elements, wherein N edges in the mesh of a given structure are categorized into M localized groups based on their proximity to each other. Incorporating this grouping concept of FMM reduces the complexity of MoM from $O(N^3)$ to $O(N^{3/2})$, which is significant for large value of N . There are two important interaction types in MoM-FMM, namely, near-field (applies to neighbor groups and utilizes conventional MoM approach) and far-field (applies to groups spaced apart and utilizes on-the-fly computations without having a need to store element-to-element interactions for each mesh element in the group). Recently, MoM-FMM has been implemented using parallelization on GPU clusters, achieving a good speed-up factor in computation [87]. To simplify modeling of the human subject using MoM-FMM, the body parts are approximately modeled here by using perfectly conducting ellipsoids between the joints except for the head, which is represented by a sphere, as shown in Figure 3.2. A representative mesh for the human is shown in Figure 3.2 (c).

The full wave analysis to model the motion of a human was carried out with the same parameters used for the Boulic model, i.e. a height of 1.72 m and walking with a velocity of 0.33 m/s. A z-polarized plane wave with a 3 GHz frequency and propagating along -x direction is assumed to illuminate the human body, as shown in Figure 3.2 (d). The reflected (scattered) fields are similar to what would be captured by the radar receiver, and can be used to develop motion

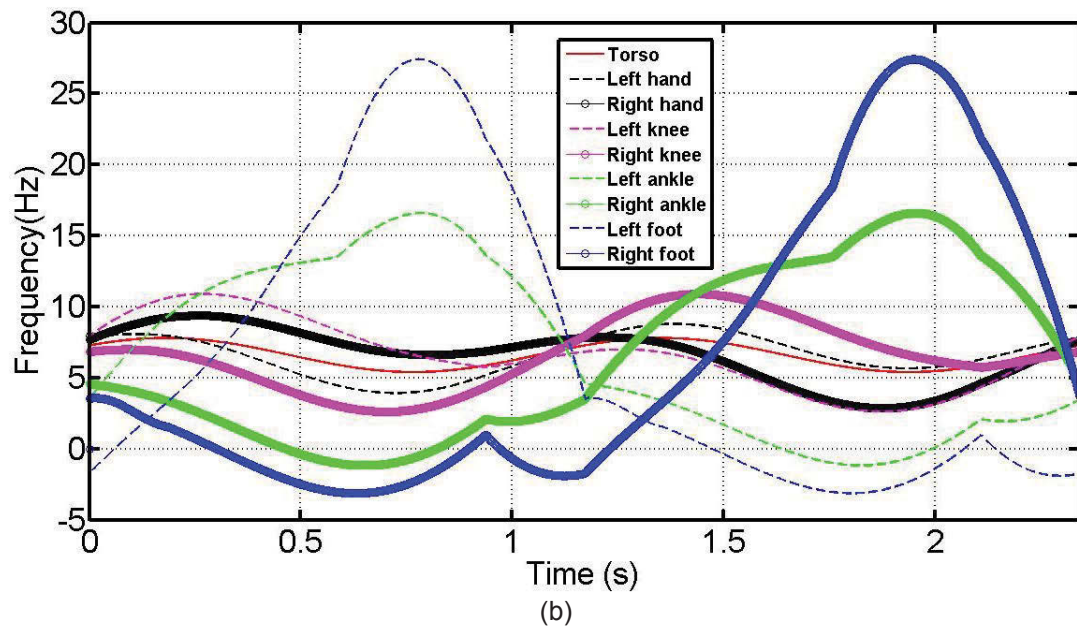
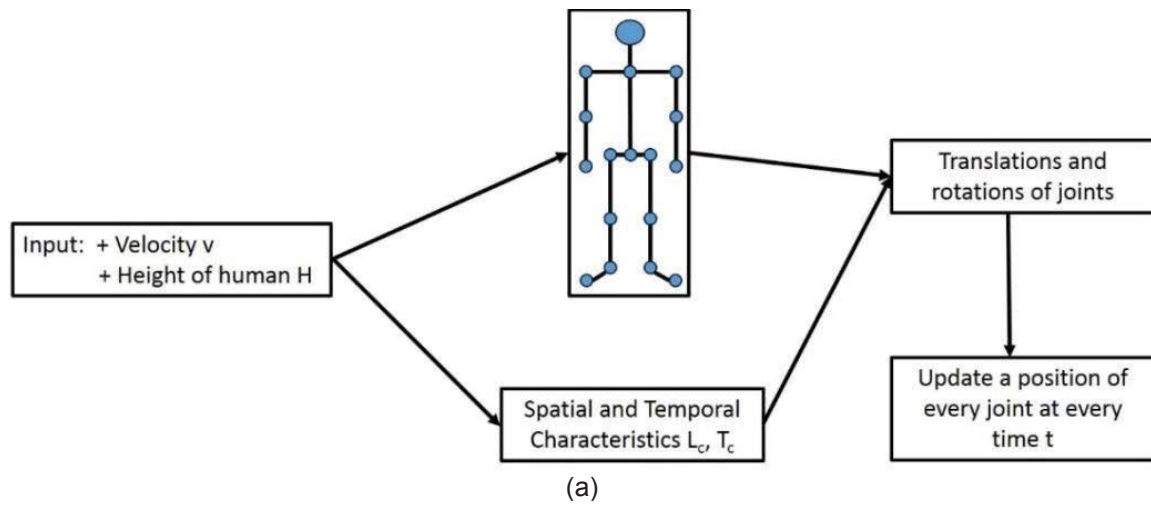
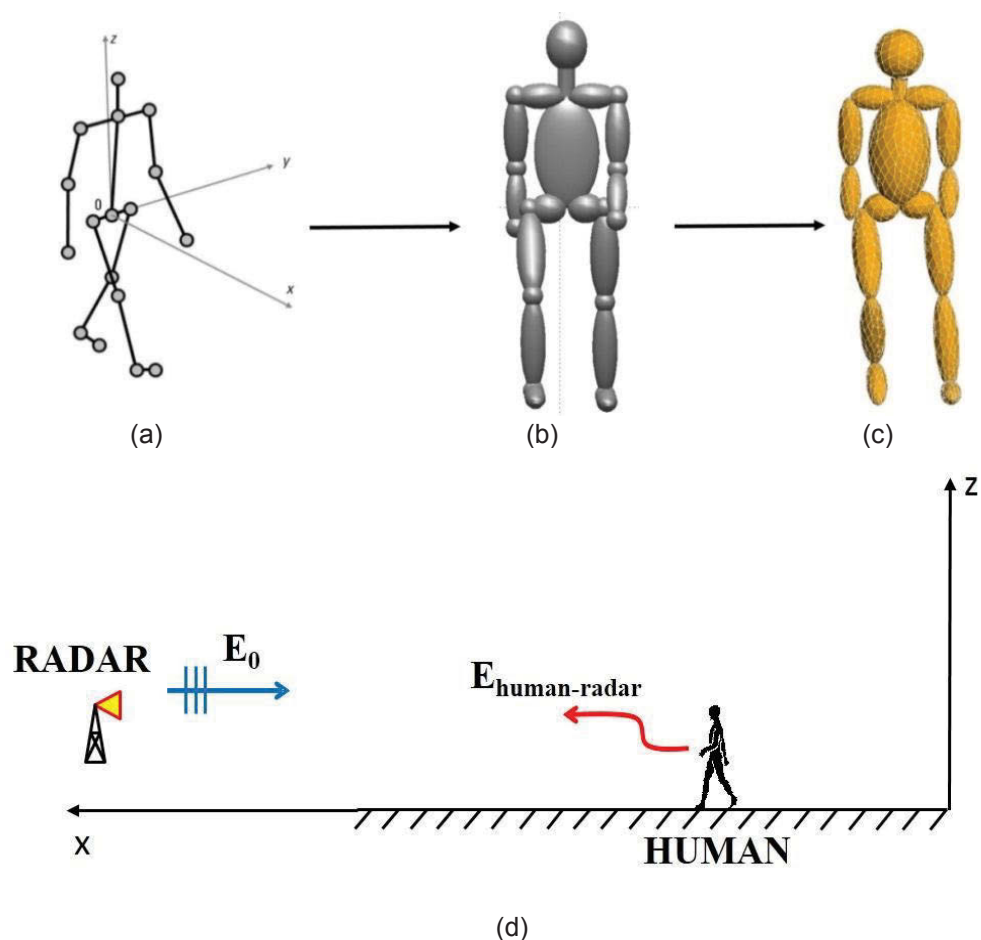


Figure 3.1 (a) Human motion model with 17 body parts. (b) μ -D frequencies of different body joints in one cycle.



(d)
Figure 3.2 (a) Human joint body. (b) Human ellipsoid body. (c) Meshed human body and (d) Human scattering scenario.

spectrograms. However, antennas utilized in our simulation were assumed isotropic; directional antennas like those used in our radar measurement set-up can be eventually used for better accuracy. Subsequently, we use these simulated spectrograms to analyze different body motion characteristics as will be explained in the next section.

3.5 Simulation results

In this section, the μ -D signatures from a walking human are simulated and compared to Boulic model results. Subject is located at the origin point, i.e., (0, 0, 0) m, walking towards the radar. A 3 GHz CW radar located at (2.5, 0, 1) m is assumed to receive the scattered fields from the scene, i.e., radar is 2.5 m away from the subject along the x-direction, and mounted at 1 m height. It is important to mention that using of wider band signals in our simulation (such as UWB radar) will give better resolution- but it is computationally inefficient. In our simulation too, a human model is assumed to move along the direct path to the radar, and is represented by point scatters – created based on the Boulic model as described in the previous section.

The μ -D signatures from the scene are then estimated by applying STFT and STSSM to the center range-gate over short time duration to compute back-scattered fields received at the radar. This approach appears to be applicable even to narrow-band data due to its independence of range resolution. In this simulation, the human walking cycle is 2.43 s, and 200 single-frequency samples are collected and stored. FFT is applied to each pulse and the center range-gate is selected. Next, a sliding window length of 24 pulses is used to formulate the state space method and extract movements from many body parts. The model order of STSSM, i.e., the number of signals impinging into the data to compute the poles that give rise to Doppler frequencies from the human torso and feet, is set to 4. The simulated μ -D spectrograms using STFT and STSSM are shown in Figure 6.2 (a) and (b). They depict that the highest μ -D frequencies around 30 Hz are from the lower parts of the human body, i.e., the feet. Furthermore STFT and STSSM show similar trends in the μ -D frequencies monitoring. However, the region of the curves from STSSM that lie within 0.4 s to 2.3 s provides better performance than STFT. Thus, μ -D trajectories from left foot, right foot and torso can be distinguished in the spectrogram processed with STSSM.

To validate the performance of STSSM, the maximum μ -D frequencies of trajectories in Figure 3.3 (b) are compared with the maximum μ -D frequencies of body joints estimated with Boulic model in Figure 3.1 (b). The maximum μ -D frequency generated from the left foot, right foot and torso are estimated to be around 27.1 Hz, 27.1 Hz and 7.9 Hz, respectively. As shown in Figure 3.3 (b), the monitored maximum μ -D frequencies with STSSM for left foot, right foot and torso are 27.7 Hz, 26.3 Hz and 7.6 Hz respectively. As a result, the difference between Boulic model and results obtained from CW radar with STSSM is within $\pm 3.8\%$. The comparison details are listed in Table 3.1.

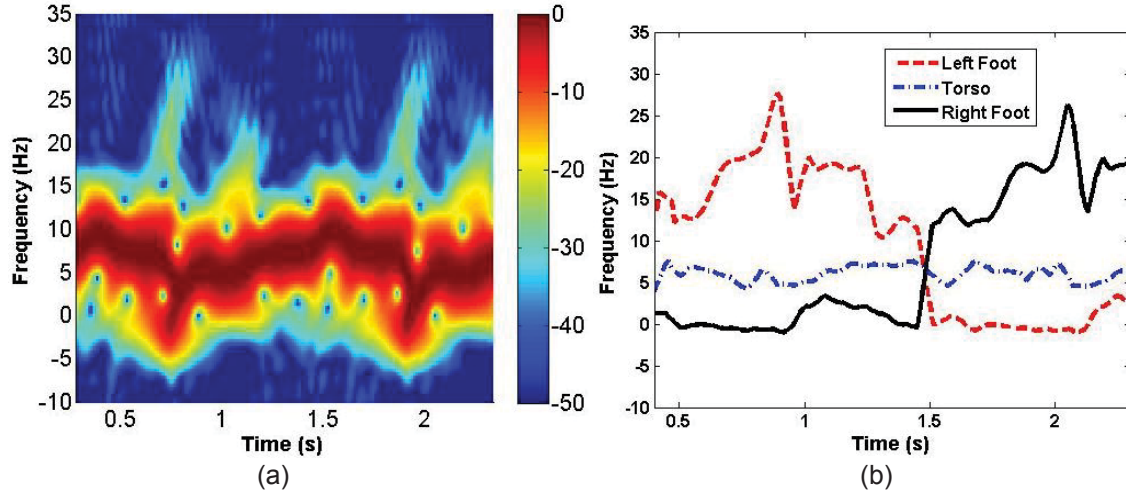


Table 3.1 μ -D signatures of a walking target with height 1.7 m and speed 0.33 m/s

	Boulic Model (Hz)	Scattering Model (Hz)	Difference (%)
Left foot	27.1	27.7	2.2
Right foot	27.1	26.3	-3.0
Torso	7.9	7.6	-3.8

3.6 Experimental results

In the simulation example described above, the STSSM algorithm was tested and its performance was compared with the Boulic model. In this section, simulated EM and experimental data are utilized to validate STSSM capability in μ -D frequency extraction from experimental data. To test the practicality of the STSSM, five experiments are conducted on three subjects walking at different angles in front of the radar receiver. A UWB radar system used in the experiments exhibits a pulse repetition frequency of 75 Hz and range resolution of 3 mm. The collected data are first processed with STFT followed by STSSM from which results are generated and compared with the Boulic model.

3.6.1 Subject Walking Towards Radar

In this experiment, the UWB radar was used to monitor the μ -D features of a walking dismount. A human subject of 1.72m height walked in front of the radar system at 0° to the radial direction. The radar data was saved into $\mathbf{s}(\mathbf{k}, \mathbf{n})$, where $\mathbf{k} = 1, 2, \dots, 2000$ represents fast time or range index, and $\mathbf{n} = 1, 2, \dots, 600$ denotes the slow time or pulse index. Thus, the radar detected a range up to 6 m for 8 s. After removal of the static background, the HRRP clearly indicates the walking trace of the human subject, as shown in Figure 3.4 (a). Spikes along the

Figure 3.4 (a) HRRP of walking subject with arms swinging, (b) Boulic model of subject at the radial direction, (c) spectrogram using STFT when sliding window length of 50 pulses, (d) spectrogram using STSSM when sliding window length of 50 pulses.

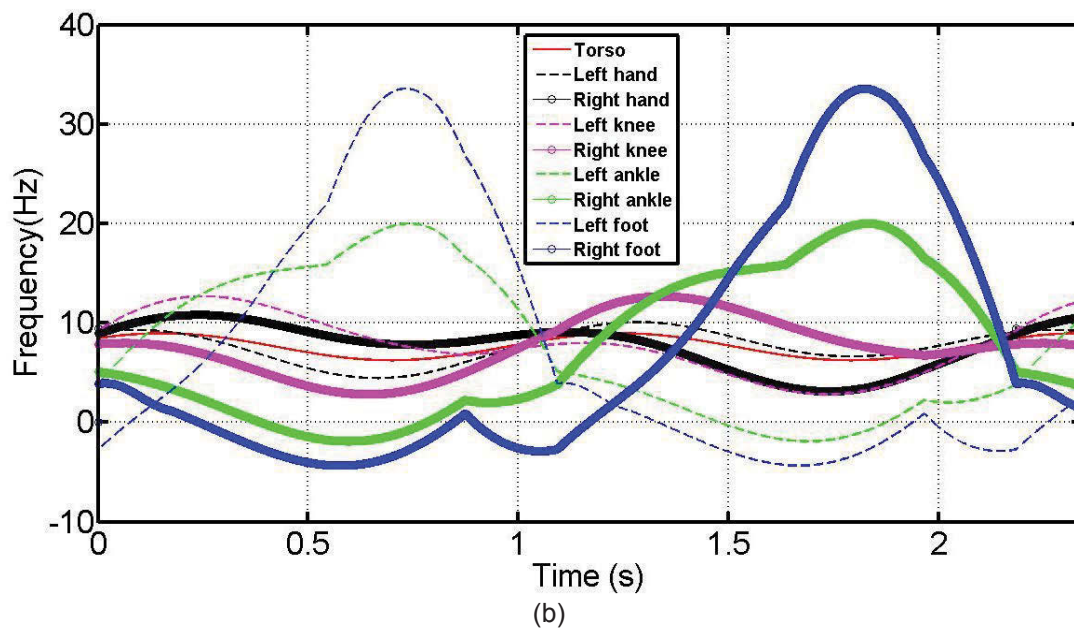
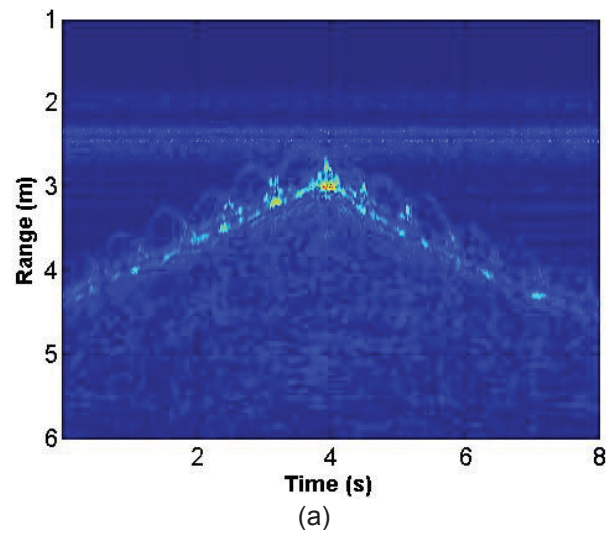


Figure 3.4 continued.

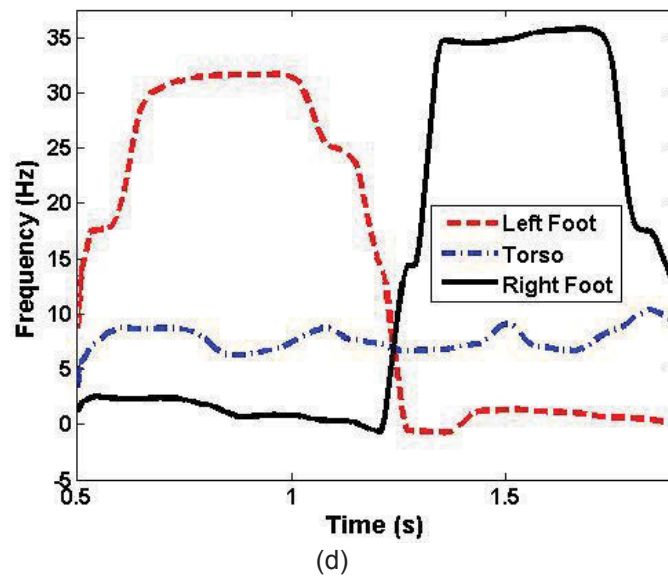
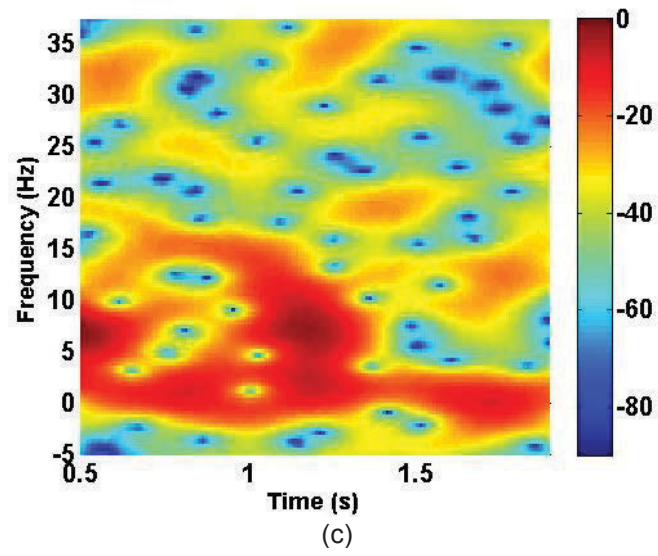


Figure 3.4 continued.

walking path are depicted. In the HRRP generated from the motions exhibited by the human limbs, i.e. arm swings and leg strides, it is observed from the HRRP that the subject has traversed the range from 2.9 m to 4.4 m. The subject first walked toward the radar system then turned around and walked away. The walking speed is thus estimated to be 0.38 m/s. By using the subject's height and walking speed, the Boulic model of a walking human is calculated and presented in Figure 3.4 (b).

To focus on the motion identification by STFT and STSSM, μ -D frequencies of a walking cycle are zoomed in. A sliding window length of 50 pulses is used for both STFT and STSSM. FFT is first applied to each reflected pulse along fast time to acquire compressed pulses. In this manner, a data cube $\mathbf{s}(\mathbf{k}, \mathbf{n})$ is transformed into a data sequence $\mathbf{y}(\mathbf{n})$, where \mathbf{n} denotes the pulse index selected at the center range-gate. STFT is applied to the slow-time signal $\mathbf{y}(\mathbf{n})$ over a window length of 50 pulses to acquire the spectrogram, as shown in Figure 3.4 (c). The order model of STSSM is set to 6. The spectrogram created by STSSM on $\mathbf{y}(\mathbf{n})$ is shown in Figure 3.4 (d), and associated μ -D trajectories of left foot, right foot and torso are extracted. The identified region of the curves in the spectrogram from 0.5 s to 2 s matches well in magnitude with the Boulic model, which demonstrates that STSSM outperforms STFT in μ -D frequencies identification.

To validate the performance of STSSM, the maximum μ -D frequencies of trajectories in Figure 3.4 (d) are compared with the maximum μ -D frequencies of body joints estimated with Boulic model in Figure 3.4 (b). As shown in Figure 3.4 (b) the maximum μ -D frequency generated from the left foot, right foot and torso are estimated to be around 34.4 Hz, 34.4 Hz and 8.8 Hz, respectively. As depicted in Figure 3.4 (d) the monitored maximum μ -D frequencies with STSSM for left foot, right foot and torso are 31.6 Hz, 35.6 Hz and 8.6 Hz, respectively. As a result, the difference between Boulic model and results obtained from UWB radar with STSSM is within $\pm 6\%$. The comparison details are listed in Table 3.2. Meanwhile, it is difficult to distinguish various parts/joints movements using STFT spectrograms as it is obvious from Figure 3.4(c).

Table 3.2 μ -D signatures of walking target with height 1.72 m and speed 0.38 m/s

	Boulic Model (Hz)	UWB Radar (Hz)	Difference (%)
Left foot	33.6	31.6	-6.0
Right foot	33.6	35.6	6
Torso	8.8	8.6	-2.3

3.6.2 Subject Walking in front of radar at oblique directions

To enhance and emphasize the practicality of STSSM, four more experiments have been conducted and data from different subjects walking in various directions are collected and processed. Two subjects walked in front of the radar at 30° and 60° to the radial direction and data were collected and processed with

STSSM. Both spectrogram and μ -D trajectories were generated from the experiments and results were compared with the Boulic model data to validate the performance of STSSM. While the subject is walking directly to the radar system, the HRRP records the walking traces of the human subject and his/her walking speed can be readily calculated. Suppose a subject who is walking in oblique directions at an angle θ to radial direction, the walking speed monitored by UWB radar is v ; where, the actual velocity of the subject is computed according to $v/\cos(\theta)$.

In the first experiment, subject 1 of height 1.71 m walked back and forth at 30° to the radial direction of radar system. The radar data was saved in a data cube denoted by $\mathbf{s}(\mathbf{k}, \mathbf{n})$, where $\mathbf{k} = 1, 2, \dots, 2000$ represents range index, and $\mathbf{n} = 1, 2, \dots, 600$ denotes the pulse index. So the radar detected a range up to 6 m for 8 s. It is observed from HRRP in Figure 3.5 (a) that the subject has traversed the range from 2.6 m to 4.2 m and the detected walking velocity from HRRP is 0.4 m/s. With subject height and walking velocity, the corresponding Boulic model of one walking cycle is presented in Figure 3.5 (b). The maximum μ -D frequencies generated from the left foot, right foot and torso are estimated to be around 35.9 Hz, 35.9 Hz and 9.5 Hz, respectively. The sliding window length of 45 pulses is used for both STFT and STSSM. FFT is first applied to each reflected pulse along fast time at dc to acquire a corresponding complex value. Data cube $\mathbf{s}(\mathbf{k}, \mathbf{n})$ is transformed to a data sequence $\mathbf{y}(\mathbf{n})$, where \mathbf{n} indicates pulse index. STFT is applied then to the slow-time signal $\mathbf{y}(\mathbf{n})$ to acquire the spectrogram, as shown in Figure 3.5 (c).

The STSSM is carried out at the center-range gate along the sliding window length over 45 pulses with a model order of 8. The extracted μ -D trajectories of left foot, right foot and torso are demonstrated in Figure 3.5 (d). The monitored maximum μ -D frequencies with STSSM for left foot, right foot and torso are 36.8 Hz, 34.2 Hz and 9.6 Hz, respectively. As a result, the difference between Boulic model and results obtained from UWB radar using STSSM is within $\pm 4.7\%$. The comparison details are listed in Table 3.3. Due to the coarse Doppler resolution, i.e, 75 Hz PRF, it is difficult to identify the μ -D frequencies of different body joints using STFT reported in Figure 3.5 (c) as well here, while the STSSM provides μ -D frequencies that clearly unravel the torso and foot motions of the human subject as depicted in Figure 3.5 (d).

In the second experiment, subject 1 walked at 60° to the radial direction of the radar system. As presented in Figure 3.6 (a), the subject traversed the range from 2.4 m to 3.5 m and the detected walking velocity from HRRP is 0.37 m/s.

Table 3.3 μ -D signatures of walking target with height 1.71 m and speed 0.38 m/s

	Boulic Model (Hz)	UWB Radar (Hz)	Difference (%)
Left foot	35.9	36.8	2.5
Right foot	35.9	34.2	-4.7
Torso	9.5	9.6	1.0

Figure 3.5 (a) HRRP of walking subject 1 (b) Boulic model of subject at 30° to the radial direction, (c) spectrogram using STFT when sliding window length of 45 pulses, (d) spectrogram using STSSM when sliding window length of 45 pulses.

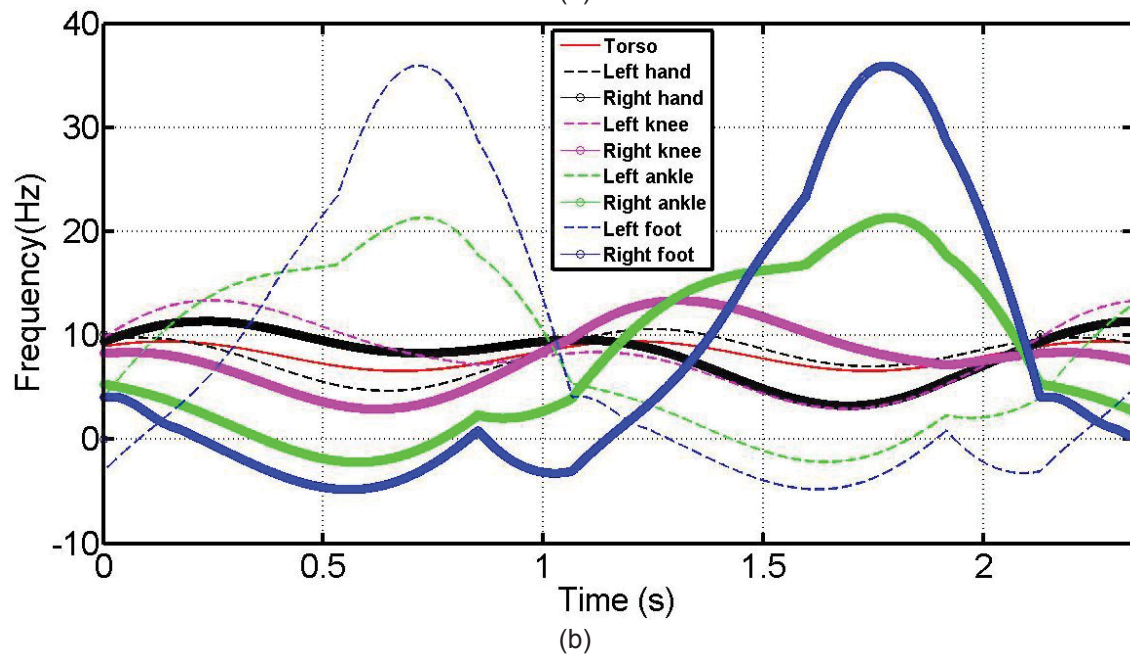
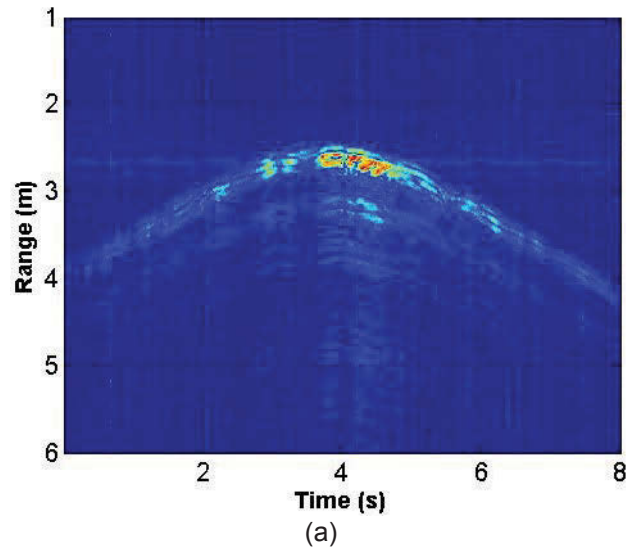


Figure 3.5 continued.

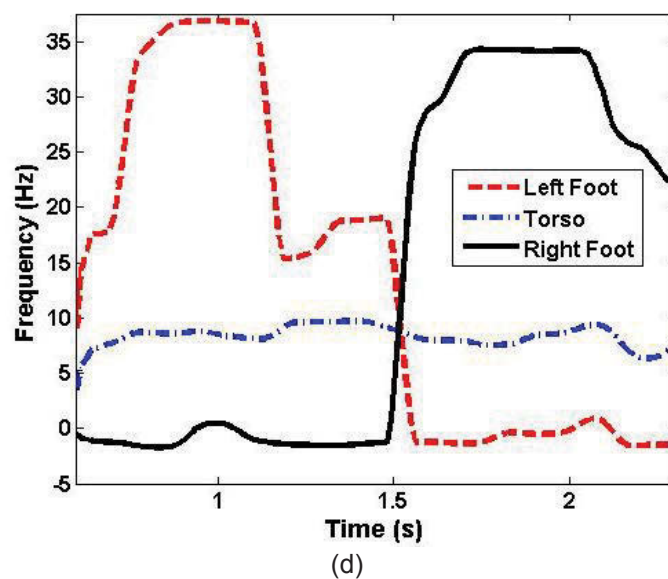
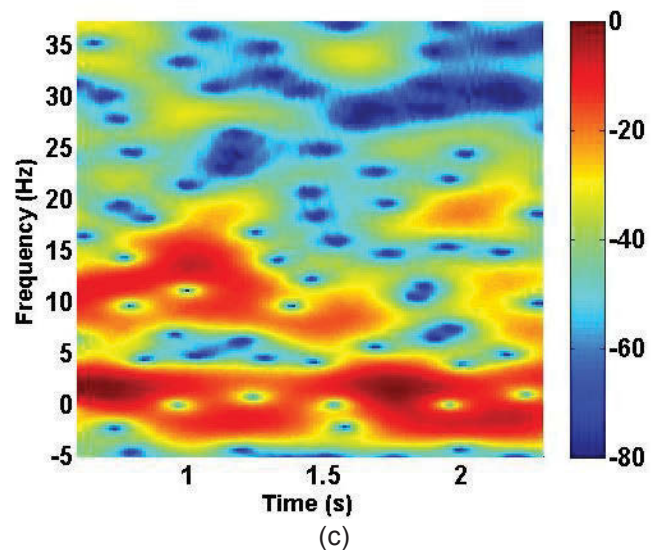
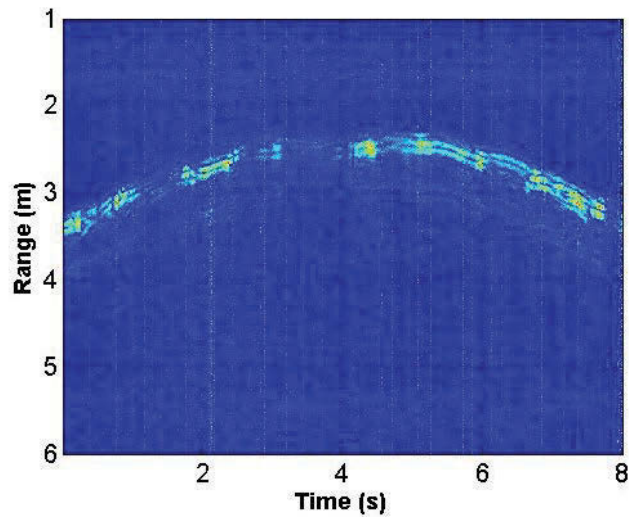
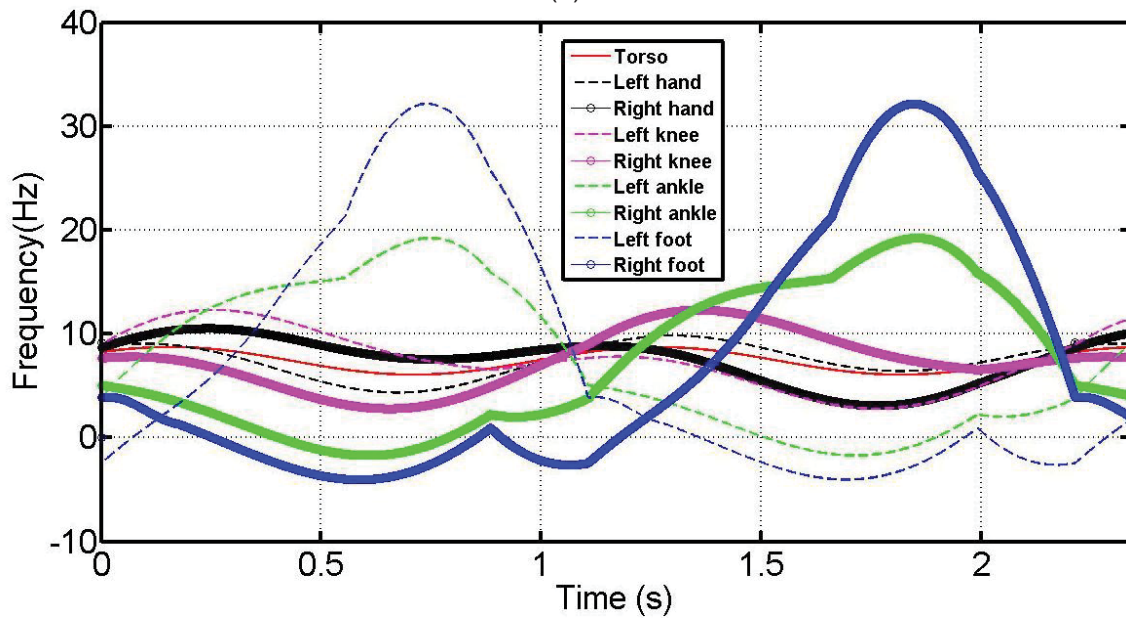


Figure 3.5 continued.

Figure 3.6 (a) HRRP of walking subject 1 (b) Boulic model of subject at 60° to the radial direction, (c) spectrogram using STFT when sliding window length of 45 pulses, (d) spectrogram using STSSM when sliding window length of 45 pulses.



(a)



(b)

Figure 3.6 continued.

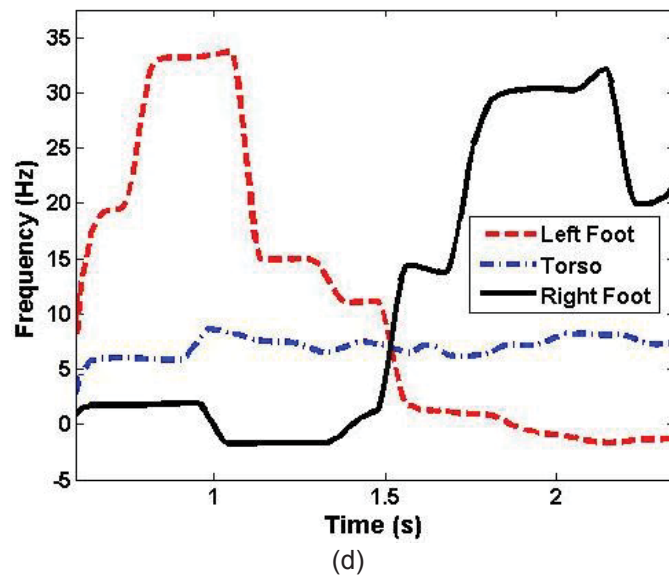
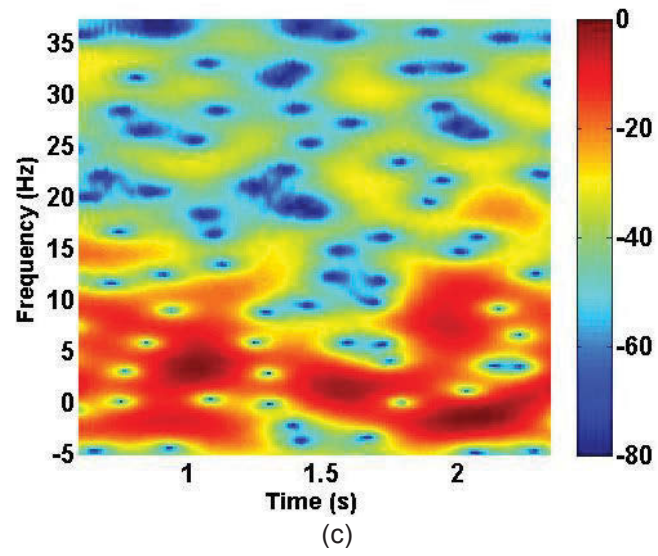


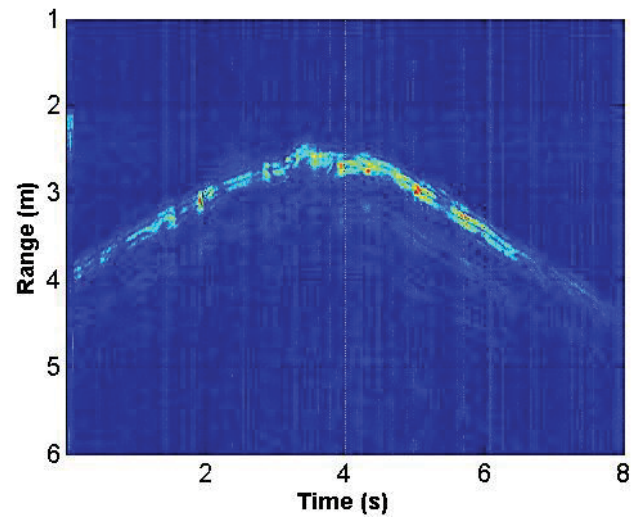
Figure 3.6 continued.

And the corresponding Boulic model is presented in Figure 3.6 (b). The maximum μ -D frequency generated from the left foot, right foot and torso are estimated to be around 32.1 Hz, 32.1 Hz and 8.7 Hz, respectively. The sliding window length of 45 pulses is used for both STFT and STSSM. Similar to the previous experiments, FFT is first applied to each reflected pulse along fast time at dc to form the slow time signal $y(n)$, and STFT is applied to the slow-time signal $y(n)$ to acquire the spectrogram, as shown in Figure 3.6 (c). A model order of 9, for the STSSM, is carried out on $y(n)$ at the center range-gate in the time direction over the sliding window of 45 pulses. As demonstrated in Figure 3.6 (d), the μ -D trajectories of left foot, right foot and torso identified in the spectrogram with STSSM. The monitored maximum μ -D frequencies with STSSM for left foot, right foot and torso are 33.3 Hz, 32.0 Hz and 8.6 Hz, respectively. As a result, the difference between Boulic model and results obtained from UWB radar with STSSM is within $\pm 3.7\%$. The comparison details are listed in Table 3.4. As shown in Figure 3.6 (c), STFT provides very coarse μ -D frequencies in the spectrogram. Due to strong reflection from torso, the corresponding μ -D frequencies around 8 Hz demonstrate high intensity in the spectrogram, while μ -D frequencies from limbs around 30 Hz show relatively low intensity and are difficult to be distinguished. Compared with STFT, STSSM again demonstrates a better performance in μ -D frequencies identification. In the third experiment, subject 2 of height 1.75 m walked at 30° (instead of 60° used in the previous example) to the radial direction of radar system. As shown in Figure 3.7 (a), the subject traversed the range from 2.7 m to 4.0 m and the detected walking velocity from HRRP is 0.40 m/s. The corresponding Boulic model is presented in Figure 3.7 (b). The maximum μ -D frequency generated from the left foot, right foot and torso are estimated to be around 36.7 Hz, 36.7 Hz and 9.5 Hz, respectively. The sliding window length of 45 pulses is used for both STFT and STSSM. The spectrogram acquired with STFT is shown in Figure 3.7 (c). Though, STFT highlights the μ -D frequencies due to torso in spectrogram of Figure 3.7 (c), it is still challenging to distinguish the μ -D frequencies from other body joints. The model of STSSM is now set to 9. As demonstrated in Figure 3.7 (d), the μ -D trajectories of left foot, right foot and torso identified in the spectrogram with STSSM. The monitored maximum μ -D frequencies with STSSM for left foot, right foot and torso are 34.0 Hz, 34.7 Hz and 9.8 Hz, respectively. As a result, the difference between Boulic model and results obtained from UWB radar with STSSM is within $\pm 7.4\%$. The comparison details are listed in Table 3.5. The deviations are mainly due to the inconsistent walking

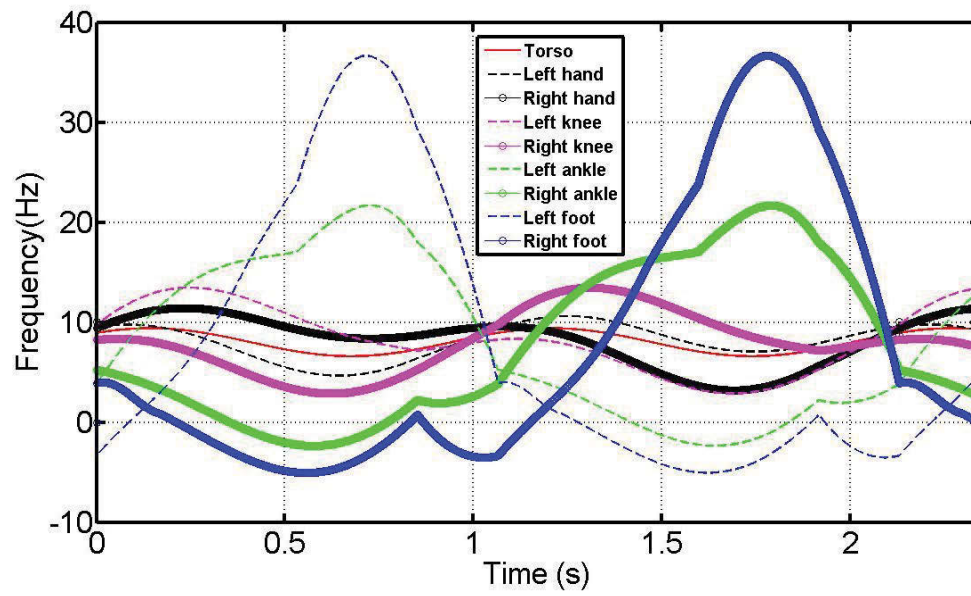
Table 3.4 μ -D signatures of walking target with height 1.71 m and speed 0.37 m/s

	Boulic Model (Hz)	UWB Radar (Hz)	Difference (%)
Left foot	32.1	33.3	3.7
Right foot	32.1	32.0	-0.3
Torso	8.7	8.6	-1.1

Figure 3.7 (a) HRRP of walking subject 2 (b) Boulic model of subject at 30° to the radial direction, (c) spectrogram using STFT when sliding window length of 45 pulses, (d) spectrogram using STSSM when sliding window length of 45 pulses.



(a)



(b)

Figure 3.7 continued.

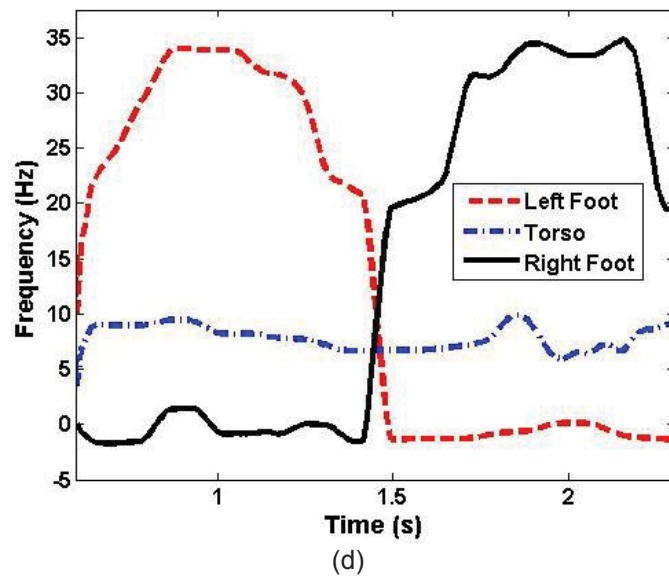
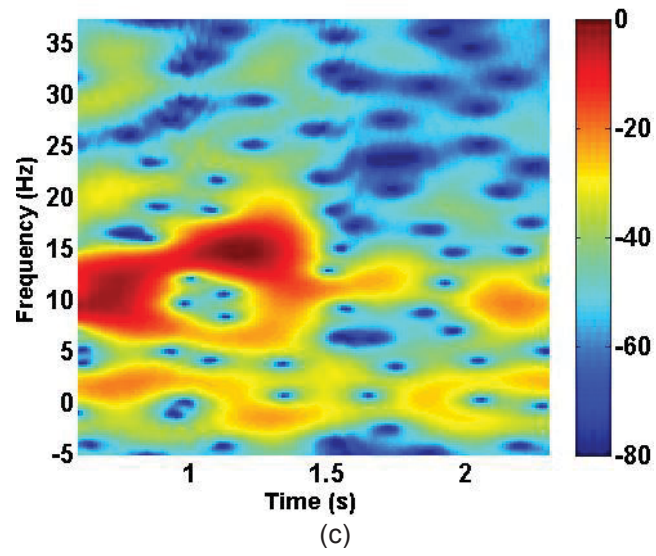


Figure 3.7 continued.

Table 3.5 μ -D signatures of walking target with height 1.75 m and speed 0.4 m/s

	Boulic Model (Hz)	UWB Radar (Hz)	Difference (%)
Left foot	36.7	34.0	-7.4
Right foot	36.7	34.7	-5.5
Torso	9.5	9.8	3.2

velocity of subject during the experiment, which caused the difference of maximum μ -D frequencies between Boulic model and experimental results for both left and right foot.

In the fourth and final experiment, subject 2 of height 1.75 m walked at 60° to the radial direction of radar system. As shown in Figure 3.8 (a), the subject traversed the range from 2.4 m to 3.5 m and the detected walking velocity from HRRP is 0.40 m/s. The corresponding Boulic model is presented in Figure 3.8 (b). The maximum μ -D frequency generated from the left foot, right foot and torso are estimated to be around 36.7 Hz, 36.7 Hz and 9.4 Hz, respectively. The sliding window length of 45 pulses is used for both STFT and STSSM. The spectrogram acquired with STFT is shown in Figure 3.8 (c). The model of STSSM is similarly set to 9. As demonstrated in Figure 3.8 (d), the μ -D trajectories of left foot, right foot and torso identified in the spectrogram with STSSM. The monitored maximum μ -D frequencies with STSSM for left foot, right foot and torso are 35.2 Hz, 36.6 Hz and 10.0 Hz, respectively. As a result, the difference between Boulic model and results obtained from UWB radar with STSSM is within $\pm 6.4\%$. The comparison details are listed in Table 3.6. Due to weak reflections from human feet, it is difficult to identify μ -D frequencies from left and right foot with STFT, as shown in Figure 3.8 (c). Comparatively, STSSM clearly detected the μ -D trajectories for both left and right foot of human subject.

These experimental results, and their correlation with Boulic model that integrate motion dynamics, have clearly demonstrated that STSSM has the capability to identify the motion of body joints, i.e., left foot, right foot and torso, and extract physiological gait characteristics from radar measurements. The curves show peak frequency values that match closely the estimates of Boulic model. The deviations are due to the variations of human walking velocity during the experiment. The identified regions by the detection trajectories are in good agreement with Boulic model. The differences of curve shapes between monitored trajectories and Boulic model are highly due to the coarse Doppler resolution and the strong intensity from the torso that obscures the nearby body part motions, the low STSSM model order enables tracking of the stronger signals. Though, the reflections from human feet are relatively weaker compared with the torso, μ -D frequencies from human feet were successfully identified in both simulation and experimental results processed with STSSM. The performance of STFT and STSSM were compared in the conducted experiments. STSSM outperforms STFT in μ -D frequencies detection especially for left and right foot. Subsequently, the capability of μ -D identification using UWB radar and

Figure 3.8 (a) HRRP of walking subject 2 (b) Boulic model of subject at 60° to the radial direction, (c) spectrogram using STFT when sliding window length of 45 pulses, (d) spectrogram using STSSM when sliding window length of 45 pulses.

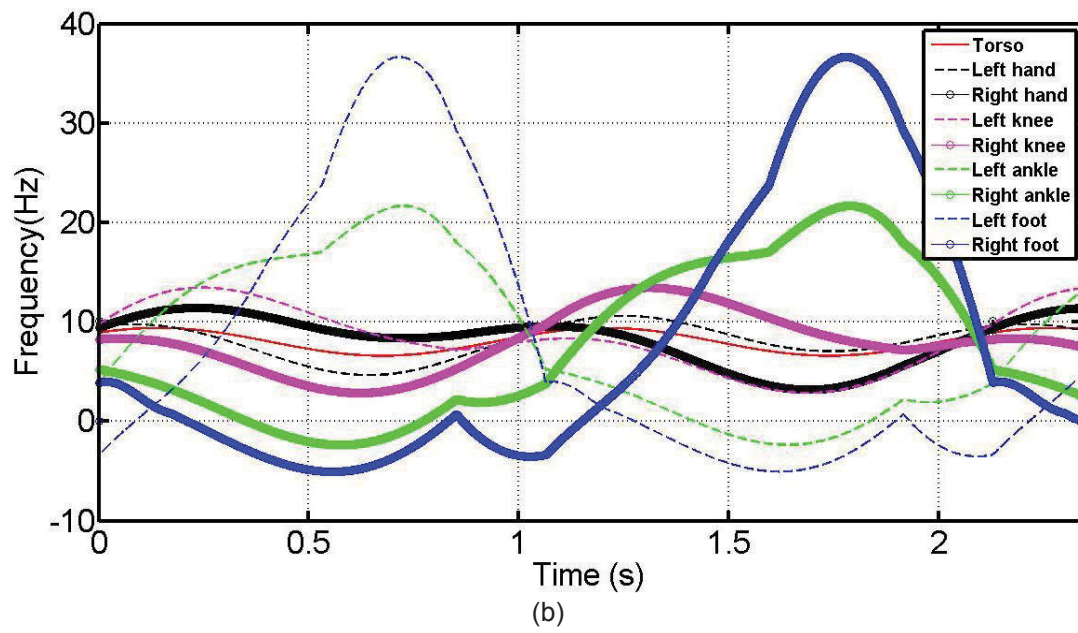
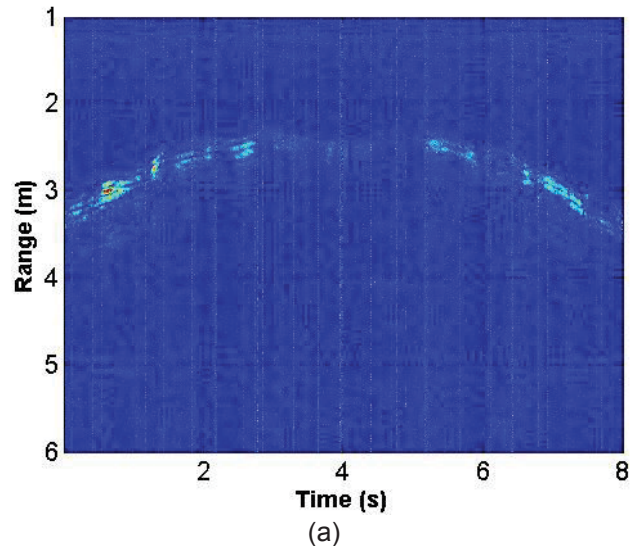


Figure 3.8 continued.

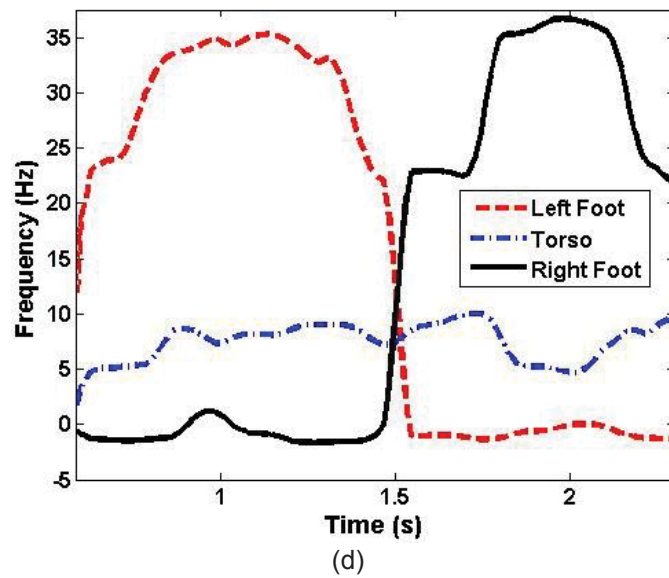
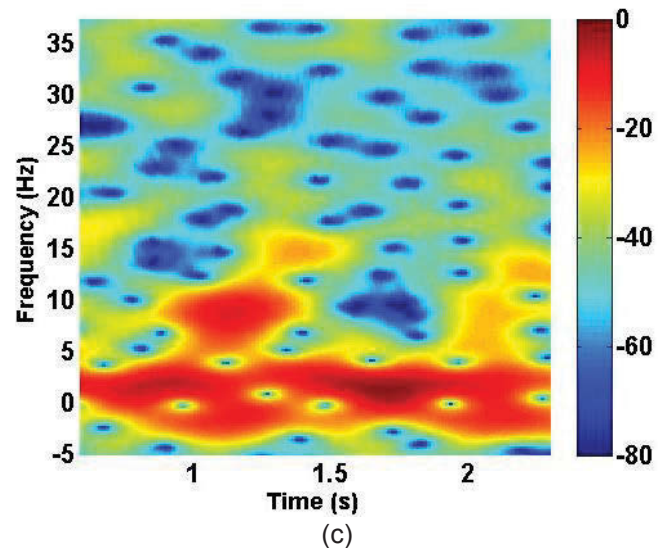


Figure 3.8 continued.

Table 3.6 μ -D signatures of walking target with height 1.75 m and speed 0.40 m/s

	Boulic Model (Hz)	UWB Radar (Hz)	Difference (%)
Left foot	36.7	35.2	-4.1
Right foot	36.7	36.6	-0.3
Torso	9.4	10.0	6.4

processing with STSSM has been validated. It appears that a STSSM with model order around 8, and a sliding window size around 45 pulses are adequate to unravel the torso and foot motions process parameters. The other weaker signals from body joints such as knees, ankles, toes, etc could be detected with a larger model order. However, due to the low Doppler resolution their detections via STSSM are inconsistent and cannot be tracked; thus, they are not considered in the work. Thus, it appears that a two-dimensional (2-D) STSSM might be an appropriate method to retrieve motions from knees, ankles toes, etc using low PRF UWB data which is currently under investigation.

3.7 Conclusion

In this chapter, UWB radar system was applied toward human gait analysis. Using the developed UWB radar prototype, we created a library of a wide variety of μ -D signatures for human body parts. State space method was investigated to extract motions from several body joints. The μ -D frequencies from each body joints that exhibit adequate returns were experimentally extracted with STSSM using the UWB radar system. In the human walking experiment, the μ -D trajectories from left foot, right foot and torso of different subjects at line of sight and at direct and oblique directions were successfully retrieved with a discrepancy of less than $\pm 8\%$ compared to results from the Boulic model. The differences between simulated and experimental results are revealed: (1) in the experiment, target motions did not exactly follow the Boulic model assumed in the EM scattering phantom, (2) UWB radar showed a bi-static architecture and the incident wave was not perpendicular to the human chest wall as assumed in the scattering model, (3) EM analysis are based on CW radar. Nonetheless, these preliminary results are still encouraging and the phantom models can still be improved in the future for closer agreement with experimental data. Feasibility of detecting other body parts from coarse PRF data is currently under investigation using advanced STSSM methods.

CHAPTER FOUR ³

ALTERNATIVE ULTRA-WIDEBAND TRANSCEIVER BASED ON STEPPED-FREQUENCY CONTINUOUS WAVE OPERATION AND COMPRESSIVE SENSING

4.1 Background

Ultra-wideband (UWB) technology has been developed for over 50 years since the early work of 1960 [88] to analytically verify the transient behavior of a class of TEM-mode microwave networks. UWB has been defined by the Federal Communications Commission (FCC) as a system that operates with a minimum fractional bandwidth of 20%, or with a minimum -10-dB bandwidth of 500 MHz [89]. However, the two fields in which UWB technology has been extensively investigated are UWB communications and UWB radar systems. Although the topic of this chapter is about UWB radar systems, it is worth mentioning that many researchers have been working to combine the radar and communications aspects of UWB technology into one system by using the so called orthogonal frequency division multiplexing (OFDM) UWB waveforms, which represents a new generation of the radar systems [90].

For a radar system, it is well known that the range resolution is inversely proportional to the bandwidth of the radar signal. The ability to achieve high range resolution results in a number of advantages including improved range accuracy, reduced clutter within the cell, high resolution range profile (HRRP), and aiding in target classification [91]. Therefore UWB radar systems have been increasingly attracting attention compared to their narrowband counterparts. In the last few years, for example, various UWB radar systems have been successfully developed and widely used for many interesting applications. One of the very fascinating application areas for UWB radar has been in the area of precise indoor localization. UWB localization system introduced in [92] utilizes a short pulse of 300-ps width, which is modulated by an 8-GHz local oscillator and is transmitted through a monopole antenna. This signal is received by several sub-stations and a time difference of arrival (TDoA) algorithm is utilized to triangulate the precise location of the transmitter. Besides the high resolution in the range dimension, UWB radar systems can also achieve high resolution in the azimuth dimension by using an antenna array in a SAR way. The ability to obtain a 2-D image of the observed scene makes it possible to apply UWB radar systems to ground penetrating detection [93], and through wall imaging [94].

³ I worked on this chapter with Haofei Wang, Quanhua Liu, Lixiang Ren, Erke Mao from Beijing Institute of Technology, and Vinh Dang, Ozlem Kilic from The Catholic University of America.

More applications have been recently demonstrated like in [95], a UWB radar has been mounted on an aerial vehicle to provide navigation information in global positioning system (GPS)-denied environment by measuring the range and Doppler of the scatterers on the ground.

Usually, UWB radar systems operate either in time domain or in frequency domain. The time domain UWB radar works with a single very short pulse so that high range resolution can be acquired. This kind of time domain UWB radar features a low power consumption and simple transmitter architecture. However, receiving (retrieving) the short-duration UWB signals and preserving their pulse waveforms present a considerable challenge, especially when the reflected signal (echo) must be analyzed to measure the target characteristics. For instance, in the application of precise indoor localization, the duration of the transmitted pulse is usually shorter than 1 ns, so that the TDoA between different receiving sub-stations can be exactly measured. In order to record the received short pulse precisely, Nyquist sampling theorem dictates that we need an ADC circuitry that must achieve a capture rate greater than 2 Giga-samples per second (GSPS). Take the ADC chips from the TI Corporation as an example. Currently, the highest speed ADC chip commercially available from the TI Corporation is the ADC12J4000. The specifications of this chip are shown in Table 4.1; the specifications of the TI ADC chip ADS7871 used in the frequency domain UWB radar (that will be subsequently utilized in this work) are also listed as well in Table 4.1 for comparison. Considering the power dissipation, cost and resolution bits that the ADC12J4000 chip can achieve, even though it is feasible and lots of progress has been achieved along directly sampling the short pulses by using a high speed ADC, it is still relatively expensive to use such chips.

Table 4.1 Parameters of two TI ADC chips

Part Number	Sample Rate	Power	Resolution	Cost
ADC12J4000	4 GSPS	2 W	12 Bits	\$1944.99
ADS7871	48 KSPS	8.5 mW	14 Bits	\$5.25

Many researchers have put forward alternative solutions to circumvent the need for fast and expensive ADCs. For example, G.T. Ruck [96] proposed a UWB receiver, which first divides the received wideband signal in either frequency domain or time domain and then performs signal digitization with low speed low cost ADCs. In [97], a UWB pulse signal is sub-sampled upon extending (stretching) its time scale while maintaining its pulse shape so that the extended pulse signal can be handled by low speed ADC circuits. Additionally, during the past few years, extensive effort was devoted to address this problem by using equivalent time sampling method to digitize extremely fast repetitive waveforms [98]. Equivalent time sampling technique is quite efficient in reconstructing a periodic input waveform by taking a specified number of samples with low speed ADCs, then progressively shifting the sampling clock timing after each signal

cycle and subsequently taking a new set of samples until the original waveform is fully sampled. The signal is assumed quasi-static; i.e. it does not change within the sampling time.

Although the solutions mentioned above can alleviate the challenging requirements for fast ADCs, all of them concentrate only on modifying the architecture of the radar receiver. Such an approach ends up with a very complex and bulky receiver; while utilizing a simple transmitter structure. Besides, these additional devices do not always work ideally as expected, which in turn influences the performance of the receiver in practice. For example, both clock jitter and drift cause significant system noise that would affect the quality of the sampled UWB signal.

In order to simplify the architecture of the UWB radar system and balance the complexity of the transmitter and receiver, we propose, as an alternative, to operate in the frequency domain rather than time domain and divide the spectrum into several bands (channels) by using a stepped-frequency continuous wave (SFCW) at the transmit side. Unlike the time domain impulse UWB radar, which transmits the whole bandwidth instantaneously, SFCW radar transmits a series of discrete tones in a stepwise fashion to attain a large effective bandwidth. The waveform for stepped-frequency radar consists of a group of N coherent pulses whose frequencies are increased monotonically from one pulse to the next by a fixed frequency increment Δf as shown in Figure 4.1. Assuming the carrier frequency of the first pulse is f_0 , the frequency of the n th pulse is then $f_{n-1} = f_0 + (n-1)\Delta f$. The time interval between adjacent pulses is τ , and groups of N pulses are called a burst. The burst time, i.e., the time corresponding to transmission of N pulses, is called the coherent processing interval (CPI) as in conventional radars [88]. Compared with impulse UWB radar, the SFCW radar has a narrow instantaneous bandwidth so that lower-speed ADCs can be used and the hardware requirements for the receiver become less stringent. Additionally, the receiver instantaneous bandwidth would be much smaller, resulting in a lower noise bandwidth and a higher signal-to-noise ratio (SNR). However, it is necessary to receive N pulses before any processing is initiated, thus the conventional SFCW radar suffers from a serious drawback that the data acquisition time to step over many frequencies is too long for many applications.

In order to speed up the process, we propose elegant SFCW radar which can achieve high data acquisition speed by utilizing two strategies: first is to divide the spectrum into bands (channels) and transmit these bands in parallel; second is to implement compressive sensing (CS) to enable a significant reduction in the number of measurements. CS has been successfully applied to UWB radar to acquire short-duration pulses with a sub-Nyquist sampling rate [99].

To implement the first strategy, we divide the spectrum into several bands (channels) and transmit a set of frequencies simultaneously via one antenna. Subsequently on the receive side, after a de-multiplexer, the echo of each pulse (in a certain channel) can be easily separated by mixing each received echo with

the corresponding local oscillator (LO). To implement the second strategy, instead of transmitting the entire set of pulses of a burst, we only transmit a small number of random frequencies and then reconstruct the target space by using one of the efficient CS based reconstruction algorithms [100]. CS theory renders itself more naturally and easily to SFCW radar systems than impulse radar systems as no extra devices are needed to construct the measurement matrix [101]. The detailed block diagram of this proposed multi-channel SFCW radar together with some design considerations is presented in section 4.2. In section 4.3, a brief review of the CS theory is provided, together with the analysis of the applicability of CS to our radar system. Both simulation and actual measurements have been carried out and the results are shown in section 4.4. Conclusions are drawn in section 4.5.

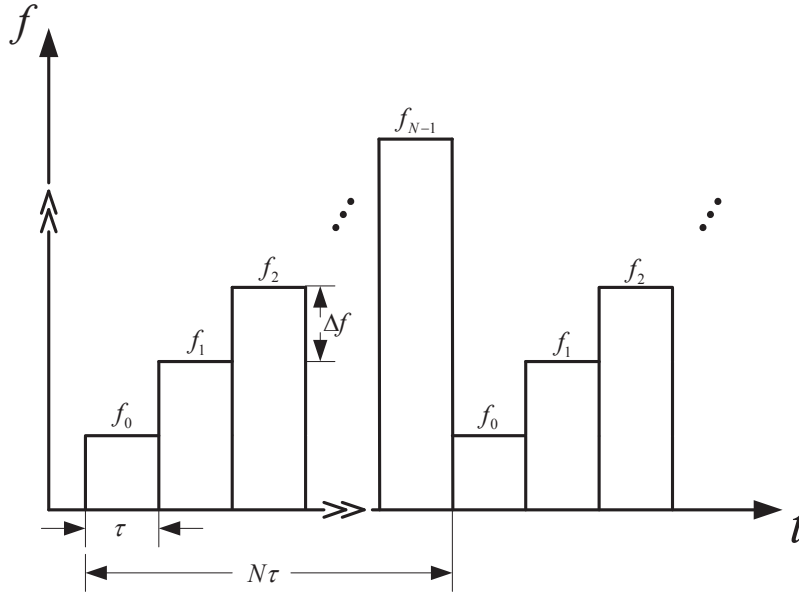


Figure 4.1 Time-frequency representation of stepped-frequency continuous wave.

4.2 Design of Two-Channel SFCW Radar System

The idea of simultaneously transmitting several frequencies originates from [102], where an eight-channel SFCW radar, called PANDORA, was constructed for applications in anti-personnel landmine detection. The total number of frequencies in PANDORA is 128, with a frequency step of 35 MHz, so the bandwidth of the radar is around 4 GHz. The PANDORA radar's initial signal is generated by one Direct Digital Synthesizer (DDS), and this signal is then mixed up by eight different local oscillator frequencies. This would require the DDS to operate over a bandwidth of 500 MHz. However, because of the spurious components dominating the DDS output spectrum, practical utilization of DDS to generate signals has been limited only to narrow frequency bands [103].

Alternatively, in the implementation of this work, to acquire a waveform with better quality, the frequency synthesizer of the radar system is based on a DDS-driven Phase Locked Loop (PLL) architecture. The utilization of PLL extends the bandwidth of the signal generated by DDS L times, where L is the multiplier factor of the PLL [104].

4.2.1 Overview of the SFCW Radar System

The block diagram of the developed two-channel SFCW radar system is shown in Figure 4.2. The two DDS channels are integrated on one board, and work simultaneously to achieve the entire ultra-wideband of 2 GHz. These two channels are synchronized by using the same 1.2-GHz reference clock. Each DDS channel synthesizes an IF signal with a bandwidth of 20 MHz, after which a 50 times PLL is used to acquire the RF stepped-frequency signal. The center frequency of each DDS channel is shifted by 1 GHz, so the total bandwidth of the stepped-frequency signal is 2 GHz. The RF stepped-frequency signal on each channel is first divided into two halves through a Mini-Circuits ZAPD-4+ power splitter. Two-half components, one from each of these two channels, are combined using a multiplexer, and then fed into a Mini-Circuits ZVE-8G power amplifier before being sent for transmission through a horn antenna. The other two-half components, (one from each channel), are split again with a Mini-Circuits ZAPDQ-4+90° power splitter to serve as the in-phase and quadrature-phase local oscillator. On the receive side, after passing through an Analog Device HMC753 wideband low noise amplifier (LNA), the combined signal is split into its four constituent components by mixing each with its corresponding local oscillator and filtering unwanted components to acquire the baseband signal. Each baseband signal is then digitized and converted to a 14 bit digital signal and stored in a PC for further processing using a low speed NI USB-6009 data acquisition card.

In the two-channel SFCW implementation, we use one reference clock to drive the two DDS chips to avoid any synchronization problem. This 1.2-GHz reference clock is divided by 24 in the first DDS chip to work as the control clock for the CPLD, which is used to generate the digital signal to control the two DDS chips. The synchronization pins on these two DDS chips are utilized to guarantee that the stepped-frequency signals are generated simultaneously by these two DDS chips. Such a system can be extended to multi-channel operations upon increasing the number of DDS circuits as well as the number of multiplexer channels.

4.2.2 Frequency Synthesizer Based on DDS-Driven PLL Architecture

In the proposed two-channel SFCW radar system (as shown in Figure 4.2), all the components are off-the-shelf modules except for the DDS board. In this subsection, we present some design details of the developed DDS board.

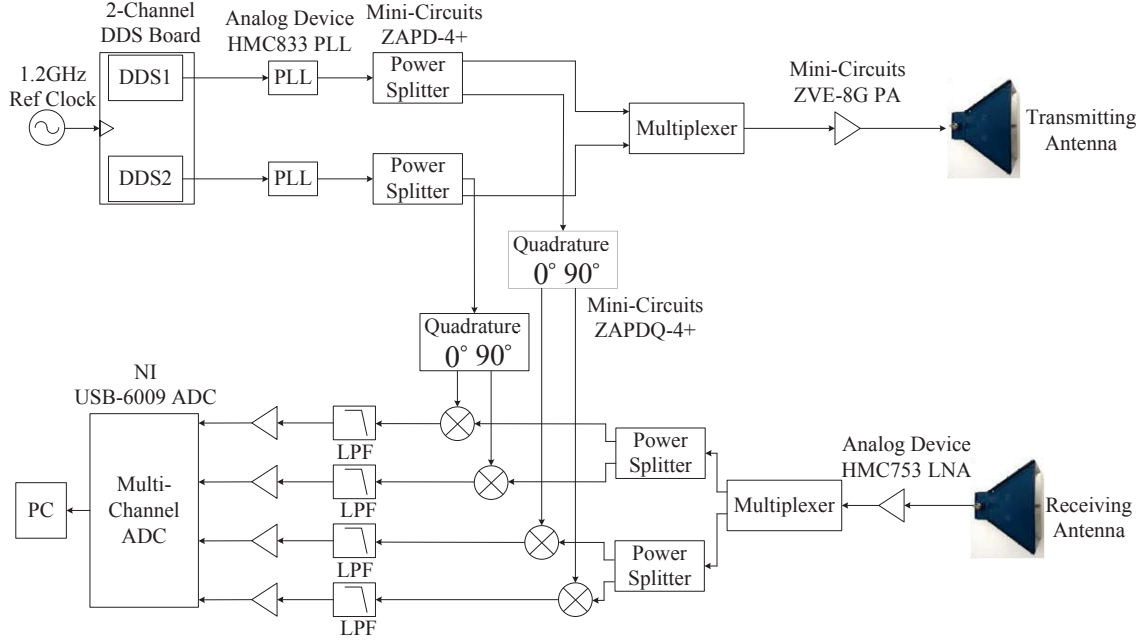


Figure 4.2 Block diagram of the multi-channel SFCW radar system.

The conventional DDS consists of a phase accumulator (PA), a sine waveform lookup table (LUT), a digital-to-analog convertor (DAC) and a low pass filter (LPF), as shown in Figure 4.3. The output frequency of the DDS is given by

$$f_{out} = \frac{F}{2^I} f_{clk}, \quad (4-1)$$

where F is the frequency control word with I -bit width, and f_{clk} is the frequency of the DDS system clock. Typically, the phase accumulator is truncated to reduce power dissipation and the die area. This truncation mechanism introduces a series of spurious components and degrades the spectral purity of the DDS output spectra. The truncation resultant spur levels could be lowered by extending the bit width of F and phase accumulator output. In practical systems, there should be a tradeoff between spur levels and device complexity. We choose here the Analog Device AD9914, which can achieve 64-bit width fine-tuning resolution by using a programmable modulus mode to generate the stepped-frequency signal.

Besides the truncation resultant spurs, DAC images may introduce even higher spurs on the DDS output frequency spectra (i.e. image frequencies). The worst case spurs occur when the images of the DAC harmonics fold back such that they are close to the DAC fundamental frequency. The frequency of DAC images is

$$f_{image} = Qf_{clk} \pm Tf_{out}, \quad (4-2)$$

where Q and T are integer multiples of f_{clk} and f_{out} , respectively. In the design, the

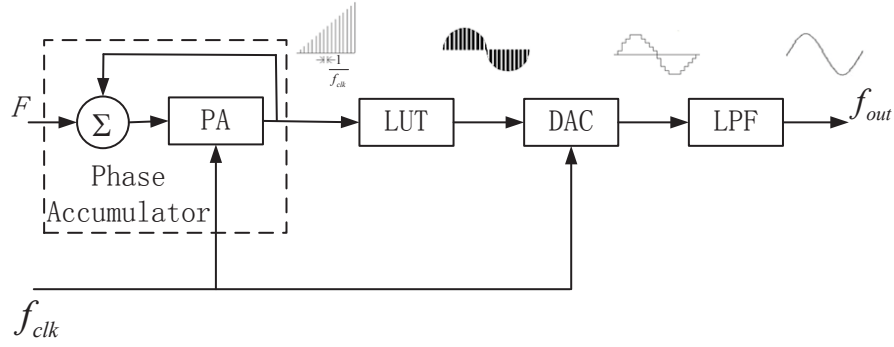


Figure 4.3 Block diagram of a DDS with the output of each stage illustrated.

DDS output frequency is carefully chosen by using an effective frequency planning method [104]. With this method, the worst DAC images are placed well off from the DDS output frequency and are attenuated by a band pass filter. The developed two-channel DDS board is shown in Figure 4.4. The two AD9914 chips can be configured with different waveform parameters using an Altera Complex Programmable Logic Device (CPLD).

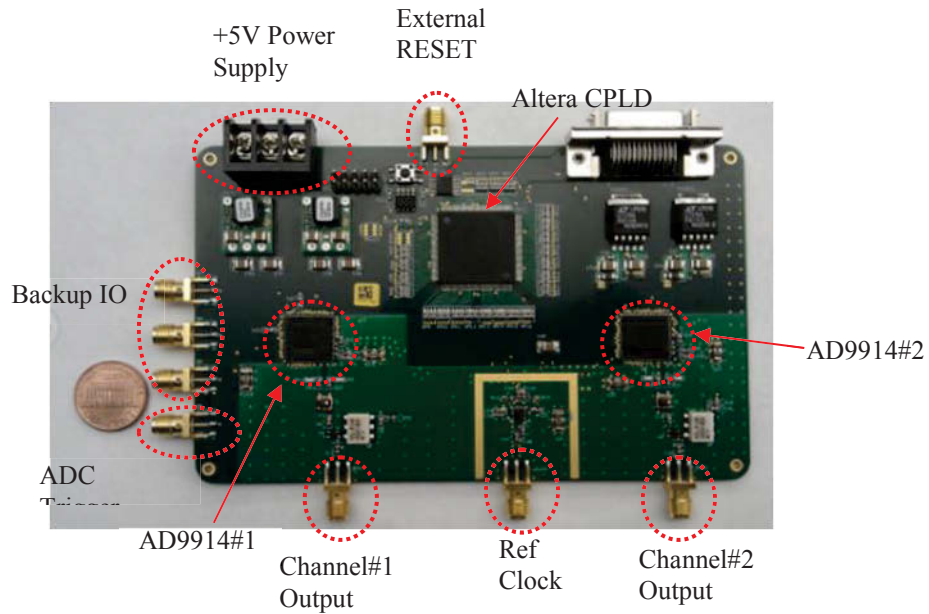


Figure 4.4 Photograph of the two-channel DDS board.

4.3 Application of CS Theory to SFCW Radar

It is well known that CS is a signal processing technique which enables a sparse signal to be recovered using a far fewer number of measurements than what is required by the Nyquist sampling theorem [105-107]. Since its first introduction to solve sparse vector recovery problems within mathematical applications, CS has

been successfully applied in many fields, such as data compressive sensing [108], channel coding [109], and magnetic resonance imaging applications [110, 111]. Recently, many attempts have been undertaken to apply CS in a variety of radar specific tasks [112-121]. In [112-114], CS was applied for the reduction of the number of measurements associated with synthetic aperture radar (SAR). Similarly, CS was studied in the spatial domain to achieve target localization by using a MIMO array, which allows for a dramatic reduction in the number of elements needed [115, 116]. The radar system introduced in [117] merged the OFDM waveform and CS together and inspected the effects of waveform bandwidth and measurement matrix on the reconstruction of the original signal. A novel CS data acquisition and imaging approach was proposed for stepped-frequency ground penetrating radar in [118]. In [119, 120], CS was utilized for imaging targets behind walls using wideband signals in SFCW radar, and in [121] was applied to joint direction of arrival (DoA)-range-Doppler tracking of moving targets. The CS theory can also be utilized for the detection of frequency hopping (FH) signals [122]. Based on [122], the FH signals can be identified and the hopping frequencies can be estimated with a tiny number of measurements.

4.3.1 Brief Overview of Compressive Sensing

Generally, let \mathbf{x} denote a desired signal of N samples, which can be represented in an orthonormal basis Ψ ($N \times N$) in terms of $\mathbf{x} = \Psi \mathbf{s}$ where \mathbf{s} is the $N \times 1$ column vector of weighting coefficients. The signal \mathbf{x} is K -sparse; that is, all but K of its entries are zero. In the spirit of CS, instead of recording the N entries in \mathbf{x} directly, we record a smaller number M ($K < M \ll N$) of linear measurements of \mathbf{x} . Since these measurements are linear, we can represent the measurement vector \mathbf{y} as

$$\mathbf{y} = \Phi \mathbf{x} = \Phi \Psi \mathbf{s} = \Theta \mathbf{s}, \quad (4-3)$$

where the measurement vector \mathbf{y} is an $M \times 1$ vector, Φ is an $M \times N$ measurement matrix. We define the sampling matrix (or projection matrix, mapping matrix, or dictionary) $\Theta = \Phi \Psi$ with a size of $M \times N$. The measurement matrix Φ must allow the reconstruction of the length- N signal \mathbf{x} from $M \ll N$ measurements, since this problem generally appears ill-conditioned with $M < N$. However, if the measurement matrix Φ and the orthonormal basis Ψ are mutually incoherent, this problem becomes well-conditioned [123]. Typically, Φ is designed in the form of randomized characteristics. In many cases, it is common to select Φ as a binary matrix containing a single randomly positioned 1 in each row, while Ψ is chosen as a $N \times N$ discrete Fourier transform (DFT) matrix. It is worth noting that the measurement process is not adaptive, meaning it is fixed and does not depend on the signal \mathbf{x} . CS allows the recovery of a K -sparse signal \mathbf{x} from M ($\approx K$) measurements with high probability. The CS reconstruction problem is formulated as an optimization problem as follows:

$$\hat{\mathbf{s}} = \min \|\mathbf{s}\|_1, \text{ such that } \mathbf{y} = \Phi \Psi \mathbf{s}' = \Theta \mathbf{s}'. \quad (4-4)$$

The readers can refer to [123] for further details of the fundamental principles of CS theory.

4.3.2 CS-based Stepped-Frequency Signal Processing

Let P be the number of channels of a multi-channel SFCW radar system. Assume that the entire bandwidth of the system is sampled by N frequencies, ranging from f_0 to f_{N-1} , with a center frequency f_c . The frequency bins f_n are uniformly distributed with a step size Δf . The target space is divided into multiple range bins r_l from 0 to r_{N-1} , where r_{N-1} is the maximum unambiguous range. The relationship between the received baseband signal $y(f_n)$ from all the channels and the range profile $x(r_l)$ can be expressed as a Fourier transform as follows:

$$y(f_n) = \sum_{l=0}^{N-1} x(r_l) \exp(-j2\pi f_n 2r_l / c). \quad (4-5)$$

Equation (4-5) can be rewritten in a matrix form as $\mathbf{y} = \Theta \mathbf{x} = \Phi \Psi \mathbf{x}$, where \mathbf{y} and \mathbf{x} are the column vectors obtained by stacking $y(f_n)$ and $x(r_l)$, respectively. Ψ ($N \times N$) is the Fourier basis function where each element is defined as $\exp(-j2\pi f_n 2r_l / c)$ and the measurement matrix Φ is chosen as the $N \times N$ identity matrix.

In the CS-based approach, due to the sparseness of the target space, the baseband signals, \mathbf{y}^{CS} , are measured at a random subset N^{CS} ($< N/P$) frequencies for each channel. We see a comparison in Figure 4.5, where Figure 4.5 (a) shows the conventional measurement scheme using full data samples and Figure 4.5 (b) illustrates the measurement pattern in the CS-based approach. By employing CS, it is observed that the data acquisition time decreases by a factor of $(N/P)/N^{\text{CS}}$. Accordingly, the reduced measurement matrix Φ^{CS} is constructed with a single randomly positioned 1 in each row, in which the positions of 1s correspond to the selected frequencies. In other words, Θ^{CS} contains a random set of PN^{CS} rows of the $N \times N$ discrete Fourier transform (DFT) matrix. The reconstruction of the range profile is formulated as the convex optimization problem: $\min \|\mathbf{x}\|_1$ such that $\mathbf{y}^{\text{CS}} = \Theta^{\text{CS}} \mathbf{x}$, which can be solved by the basis pursuit algorithm [100]. In this article, the min- l_1 with equality constraint solver in the sparse constraint optimization package l_1 -MAGIC [124] is employed to solve the above equation.

4.4 Simulation and Experimental Results

For demonstration, we utilize the previously described two-channel DDS board, and preliminary simulation and experimental results of this two-channel SFCW radar are presented in this section. The radar parameters for the setup are shown in Table 4.2. Given the bandwidth and frequency step, targets can be resolved with a range resolution of 7.5 cm and a maximum unambiguous range of 7.5 m.

4.4.1 Simulation Results

In the simulations, two horn antennas are utilized as the transmitter and receiver, respectively. The scene consists of a perfect electric conductor (PEC) trihedral

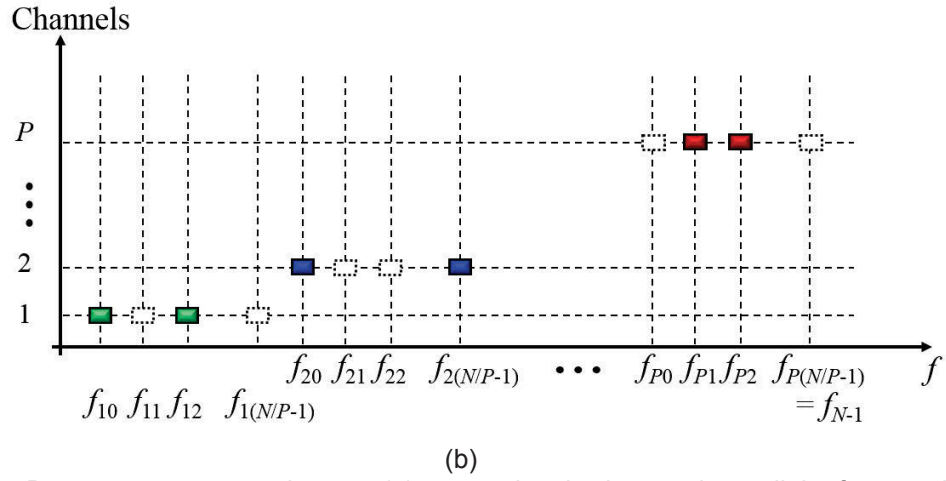
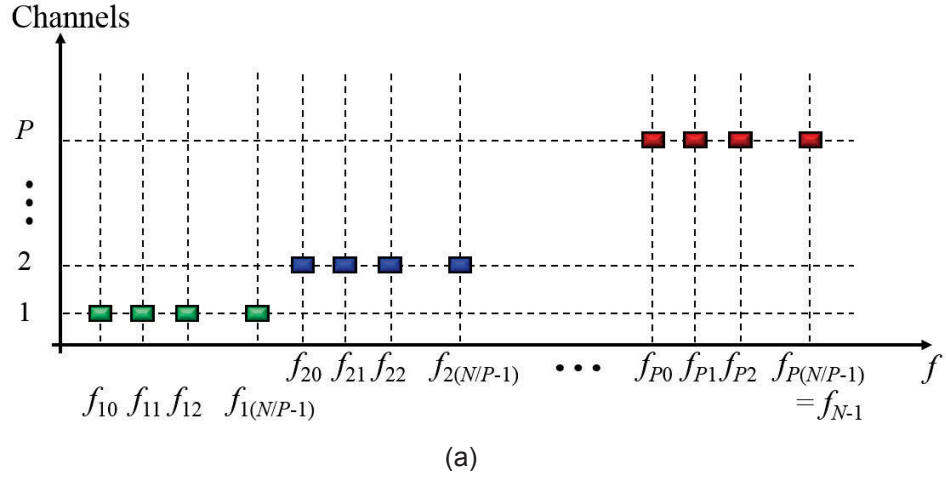


Figure 4.5 Data measurement schemes: (a) conventional scheme where all the frequencies are measured on each channel and (b) CS scheme where only randomly selected frequencies are measured on each channel. The filled rectangles indicate the selected frequencies. The frequencies are indexed by (pq) pairs where p denotes the channel index and q denotes the frequency index on that channel.

Table 4.2 Parameters of the two-channel SFCW radar system

Specification	Values
Number of Channel	2
Center Frequency	3 GHz
Bandwidth	2 GHz
Frequency Step Size	20 MHz
Number of Frequencies	100

corner reflector positioned at a distance of 1.36 m away from the antennas. A sketch of the system considered is shown in Figure 4.6, including an image of the real trihedral corner reflector shown in the upper left of Figure 4.6 for illustration. The length of each side of the corner reflector is 65 cm. The S21 parameter is measured for each frequency. For validation purpose, the full frequency domain S21 data is measured once and the results of the CS based method are created by using a few randomly selected measurements according to the measurement scheme in Figure 4.5 (b).

In order to evaluate the accuracy, the simulation results of the CS-based method are compared to the results of the conventional inverse discrete Fourier transform (IDFT) method. The robustness of the CS-based approach is validated through two parametric experiments: (i) varying the compressive sensing ratio (CSR), i.e. the ratio between the reduced measurement set and the full data set, and (ii) varying the SNR. For quantitative evaluation, a relative error is defined using a vector norm as follows:

$$e(\%) = \frac{\|\mathbf{x}_{CS} - \mathbf{x}_{IDFT}\|_2}{\|\mathbf{x}_{IDFT}\|_2} \times 100, \quad (4-6)$$

where \mathbf{x}_{IDFT} is the range profile synthesized using IDFT and \mathbf{x}_{CS} is the range profile reconstructed using CS.

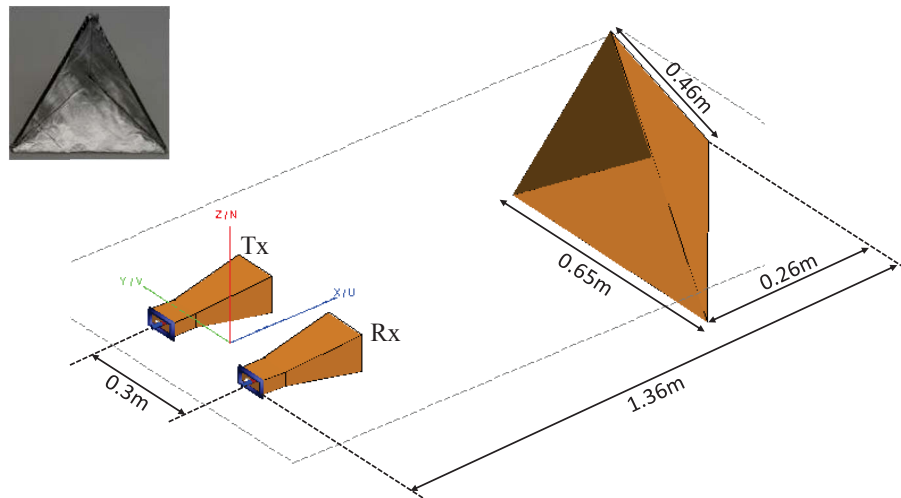


Figure 4.6 Simulation geometry.

(i) *Effect of Compressive Sensing Ratio*

The simulation is performed for $N^{CS} = 40, 30, 20$, and 10 frequencies on each channel, which correspond to the CSRs of 80%, 60%, 40%, and 20%, respectively. The synthesized HRRPs of the target by using CS method with varied CSRs are shown in Figure 4.7. For comparison, the IDFT result by using all the frequency points is also shown with a dashed line in Figure 4.7. The first small peak corresponds to the coupling between the transmitting antenna and the receiving antenna. Besides, with a high range resolution of 7.5 cm of the developed radar system, the echoes reflected by the edge and vertex of the corner reflector can be easily resolved. It can be observed that the quality of CS reconstruction suffers some degradation (i.e. the relative error increases from 1.90% to 17.62%) when the CSR is reduced from 80% to 20%, but the differences between the CS results and the IDFT results are almost indiscernible for as low as 40% CSR.

(ii) *Effect of SNR*

To evaluate the robustness of the CS based method in the presence of noise, the measured baseband signals are corrupted by adding additive white Gaussian noise (AWGN). The simulation is performed for SNR levels of 20dB, 15dB, 10dB, and 5dB, at a fixed CSR of 40%. The SNR here refers to the ratio between the power of the baseband signal and that of the noise in the output of the receiver. The reconstructed HRRPs of the target are shown in Figure 4.8. It can be observed that the quality of the range profiles deteriorates rather quickly (i.e. the relative error sharply increases from 12.62% to 42.87%) when the SNR is reduced from 20 dB to 5 dB. The degradation of the SNR leads to lowering of the sparsity of the target space, which can be obviously seen from the IDFT results. Nevertheless, the target can still be located at the correct position.

Based on the simulation, it is clear that the CS based algorithm can successfully reconstruct the HRRP of a target using only a small number of random measurements in a high SNR environment. However, poor SNR can result in apparent differences (errors) between the reconstructed signal using CS method and that using IDFT method. Figure 4.8 indicates that even with SNR of 5 dB, the position of the target can still be correctly located, which is luckily more relevant in many radar applications like precise indoor location [99].

4.4.2 Experimental Results

In this section, the CS based signal recovery algorithm is extended to real experimental data. Actual measurements are carried out by using the developed two-channel SFCW radar system. Typically in the experiment, the full frequency domain data is measured and the results of the CS based method are created by using a few randomly selected measurements.

To duplicate the simulation, a similar setup is utilized in the experiment as shown in Figure 4.9, where two horn antennas are used as the transmitter and receiver, respectively. A trihedral corner reflector is placed at a distance of 1.36 m away from the antennas similar to the simulation. The dashed line in Figure 4.10 is the

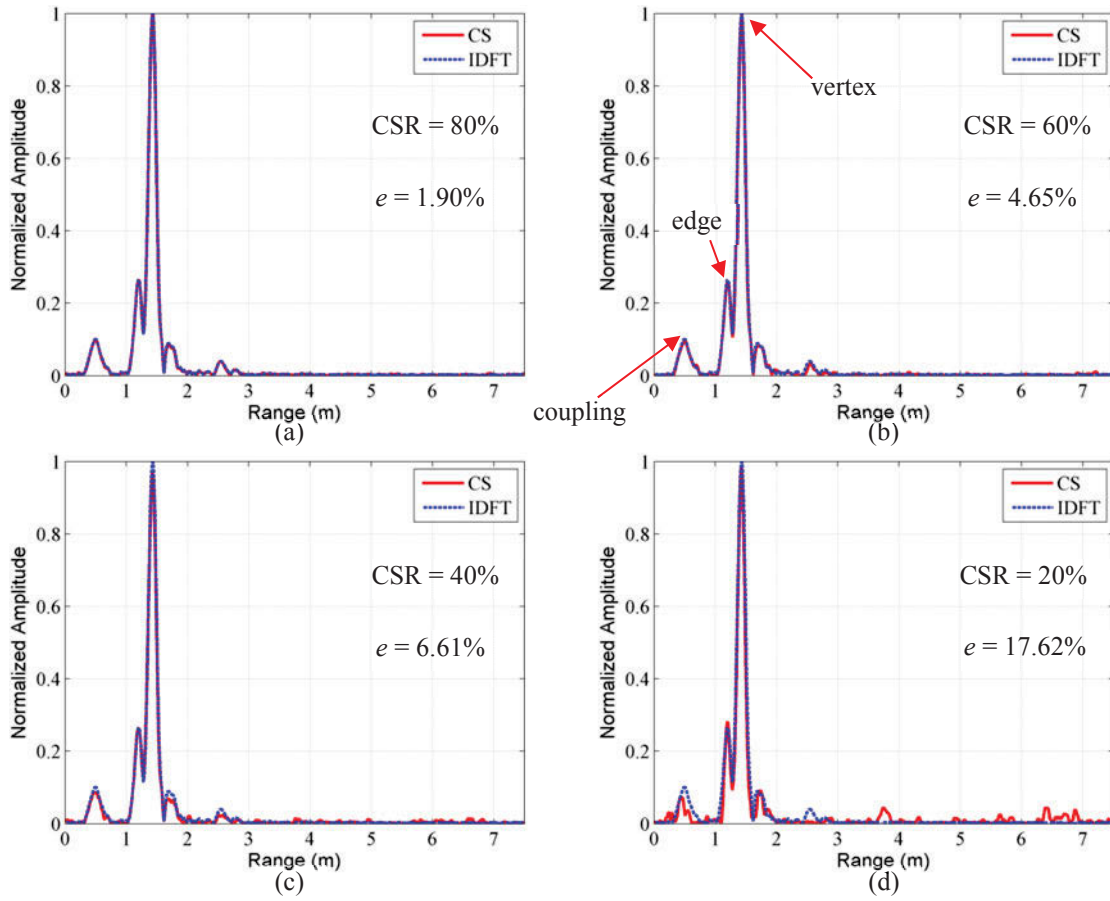


Figure 4.7 Synthesized HRRPs of the target at various CSRs.

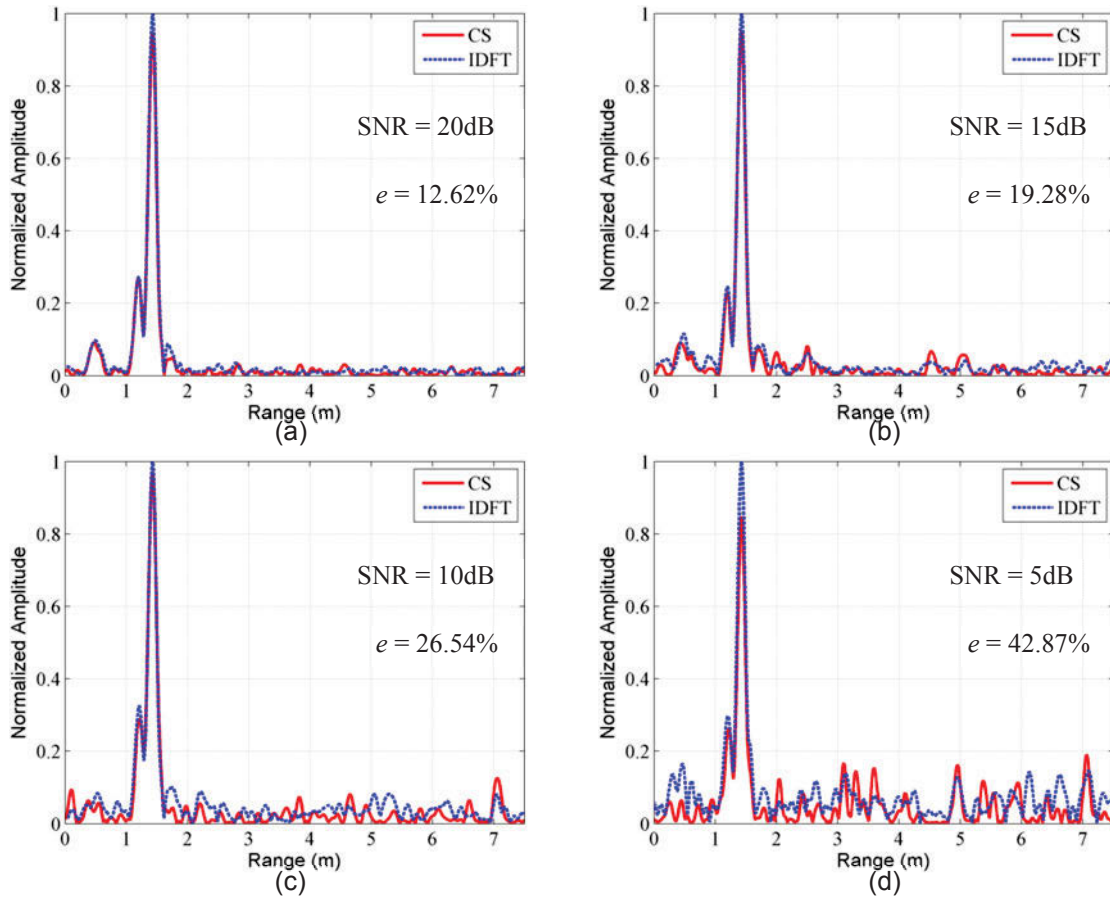


Figure 4.8 Synthesized HRRPs of the target for various SNR levels at CSR of 40%.

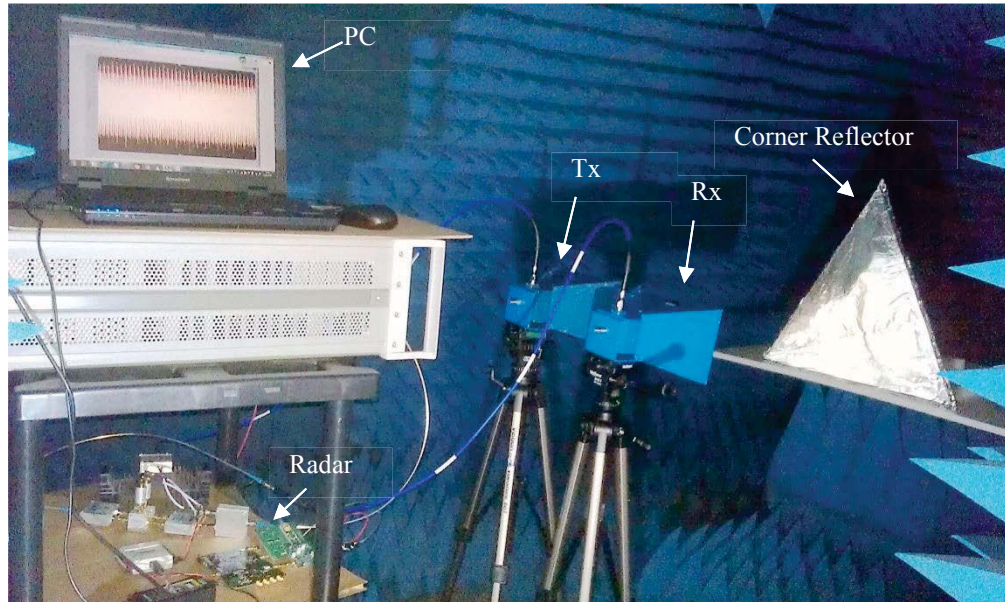


Figure 4.9 Experimental setup.

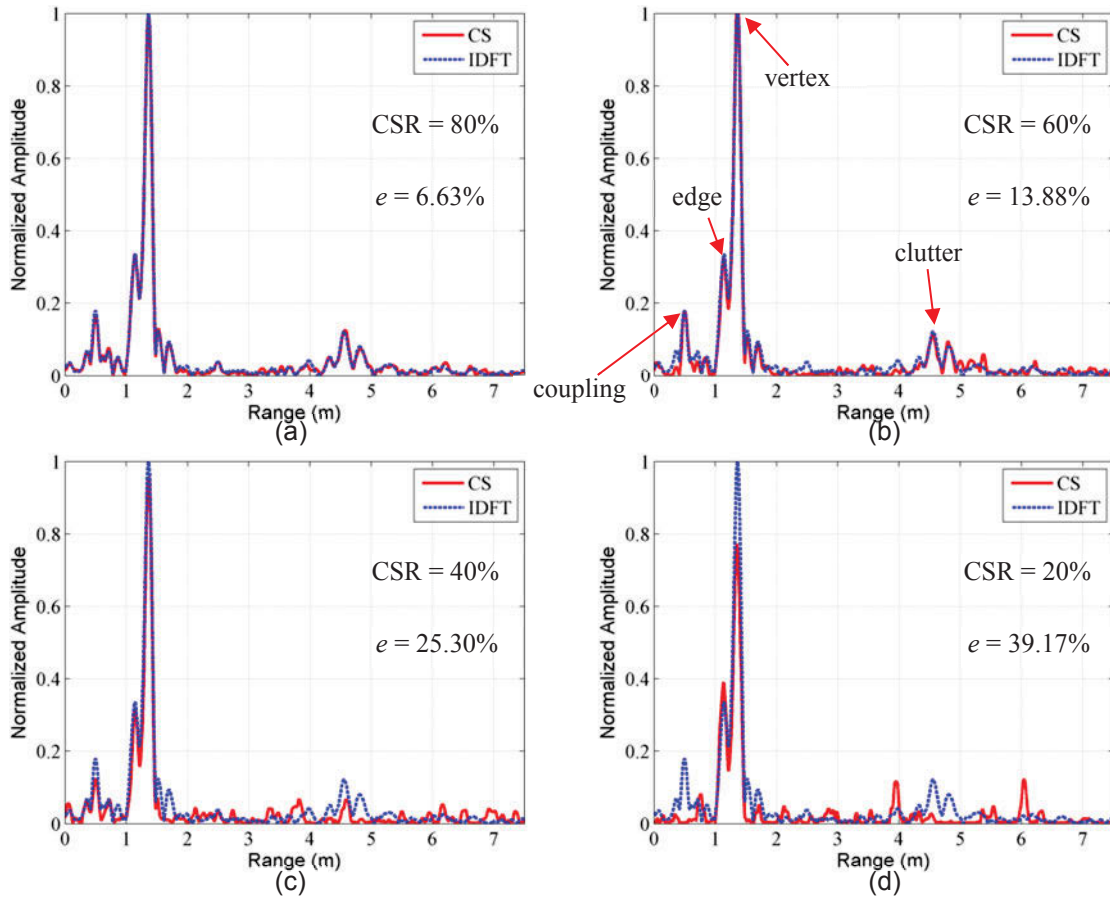


Figure 4.10 Synthesized HRRPs of the corner reflector at various CSRs.

result of IDFT method using all the 101 frequency measurements. As seen from the IDFT result, not only the peak corresponding to the corner reflector but also some lower-energy peaks caused by the Tx-Rx coupling effect and clutter can be clearly observed. Compared with the simulation results of varying CSRs, however, the CS method for the actual measurements degrades quicker for low CSRs. The reason is the presence of the interferences, i.e. clutter in the scene and system noises, resulting in a target space which is not as sparse as assumed in the simulations. However, the corner reflector can still be readily detected even when only 20% of the total frequency points are used in the CS method.

4.5 Conclusion and Future Direction

In this chapter, we provided an alternative design of a multi-channel SFCW radar system in detail, which can transmit a set of frequencies simultaneously via one UWB antenna over multiple channels operating in parallel. Instead of collecting data for all frequencies, only a random subset of frequencies is transmitted and the target space is reconstructed by using a CS based algorithm with sub-Nyquist sampling. These two strategies can reduce the data acquisition time by an order of magnitude. Both simulation results and actual measurements indicate that the CS based signal processing method allows for a reduction in the number of transmitted frequency points while still attaining performance comparable to that of the traditional IDFT method which need to process the full set data. At present, the simulation and experimental results are based on a two-channel SFCW radar system. However, four-channel SFCW radar is currently being constructed to achieve higher resolution. This SFCW radar system has great potential in practical applications, including through-wall imaging, human gait analysis and vital sign detection. These preliminary results are very encouraging given that they are based on utilizing CS to use only sub-Nyquist sampling, and avoid the need for fast ADC chips.

CHAPTER FIVE ⁴

NON-INVASIVE DETECTION OF CARDIAC AND RESPIRATORY RATES FROM STEPPED FREQUENCY CONTINUOUS WAVE RADAR MEASUREMENTS USING THE STATE SPACE METHOD

In this chapter, we discuss the design of stepped frequency continuous wave (SFCW) radar, which transmits long duration pulses with higher average power and much narrower instantaneous bandwidth than UWB waveforms, to facilitate comparable signal resolution. FFT spectrograms, typically used in the extraction of vital signs from radar measurements, produce several spurious peaks at harmonics and inter-modulation frequencies of respiration and heart rates, thereby increasing the uncertainty of these estimates, especially the heart rate. We apply a signal processing algorithm based on the state-space method for the extraction of cardiac and respiration rates from the data measured on a human subject using SFCW radar. Results show that accurate estimates of vital signs can be obtained without producing inter-modulation products that plague signal resolution in FFT spectrograms.

5.1 Background

A major challenge for non-invasive biomedical radar systems is to detect the heartbeat of a subject with high accuracy. Continuous wave (CW) radar, although bestowed with relatively simple hardware architecture, is typically narrow-band and suffers from limitation in spatial resolution [17, 18]. In order to provide both range information of target and accurate vital signs estimation, UWB radar has been studied extensively (cf. [38]). However, UWB radar systems require fast ADCs, and due to the low transmitted power, the radar needs long integration times to extract the signals of interest. Stepped Frequency Continuous Wave (SFCW) radar is an alternative technique useful to remotely monitor human subjects. Compared with continuous wave (CW) radar systems, SFCW radar systems have the advantages of localization capability and the potential to monitor multiple subjects in real time. SFCW radar can detect moving or stationary targets inside or outside buildings, and render both down-range and cross-range data [125, 126]. SFCW radar system can approximate UWB pulses in frequency domain, and therefore should have similar capabilities as UWB systems. SFCW radar is easier to build than UWB radar, requires low-speed

⁴ I worked on this chapter with Haofei Wang, Quanhua Liu from Beijing Institute of Technology, Krishna Naishadham from Georgia Institute of Technology, and Yun Seo Koo, Yazhou Wang from Qorvo.

ADCs as it has narrow instantaneous bandwidth, and interestingly, frequencies can be skipped, which is great for jamming. It also produces relatively strong received signals as it transmits long-duration waveforms; hence it possesses higher signal-to-noise-ratio (SNR) than UWB radar in vital signs detection. It is easier to calibrate the signal distortion caused by any imperfection of the SFCW radar system hardware, and it is more flexible to design the antennas since both dispersive and non-dispersive characteristics are acceptable. However, its computational complexity in retrieving data increases in comparison to UWB, because for one scan, we have to step over many frequencies, measure returned signal and then evaluate its inverse FFT.

To ensure the accuracy of detecting demodulated respiration and heartbeat signals, various phase-based detection algorithms have been proposed [3]. Typically, range is sampled at the ADC rate and cross-range is sampled at the frame repetition frequency, which are referred to as fast-time and slow-time, respectively. Conventionally, SFCW radar monitors vital signs of a person in a non-contact manner by applying FFT to the phase of the compressed pulse on slow-time samples along traversed range bins. While the torso displacement caused by respiration can be directly extracted from the phase variation, it is still challenging to detect the heart rate and its amplitude in a similar manner with high accuracy. The difficulty is that harmonics of respiration and the intermodulation between respiration and heartbeat signals may become dominant and cause errors in heart rate detection. In [34], a filter based on moving target indicator (MTI) is utilized to cancel the harmonics of respiration signal. However, intermodulation frequencies stay unsuppressed and the desired heartbeat signal could be masked when it is in the neighborhood of these frequencies. State space method (SSM) is robust and cost-effective in signal parameter estimation, and it has been used successfully in target identification [50] and electromagnetic wave-based target feature extraction [51] from polarimetric radar measurements in low SNR environment.

In this chapter, an SFCW radar system will be described in detail, including block diagrams and the novel signal model for vital signs detection based on SSM. SSM will be applied to extract respiration and cardiac rates from subjects in different scenarios and its performance will be compared with that of conventional FFT method to demonstrate its advantage in suppressing harmonics and intermodulation frequencies. All the measured results from SFCW radar will be validated with data from commercial wearable sensors.

5.2 SFCW Radar

The block diagram of a homodyne SFCW radar system is shown in Figure 5.1. A frame of stepped frequency continuous waveform consists of N pulses, whose frequencies are linearly increased from pulse to pulse with a fixed frequency step Δf . The transmitted signal is composed of a series of frames. The mathematical

expression for a frame of the transmitted stepped-frequency signal can be formulated as

$$s(t) = \frac{1}{\sqrt{T}} \sum_{n=0}^{N-1} \text{rect}\left(\frac{t-nT}{T}\right) \exp[j2\pi(f_0 + n\Delta f)t] \quad (5-1)$$

where $\text{rect}(\cdot)$ denotes rectangular function, T is the pulse repetition time, and f_0 is carrier frequency of the first pulse.

Considering the range between the static part of the target and radar as R_0 , the instantaneous range detected with the m^{th} frame can be expressed as

$$R(m) = R_0 + R_v(mT_N) \quad (5-2)$$

where $R_v(mT_N)$ is the time-varying distance between the target and radar caused by torso displacement, and $T_N = NT$ is the total time of a frame. We assume that the instantaneous range does not change during the period of a frame, which is reasonable given that the time duration of a frame is much shorter than the period of the vital signs of a human subject. Then, the received signal for the m^{th} frame can be expressed as

$$s_r(t) = a s(t) [t - 2R(m)/c] \quad (5-3)$$

where a is the amplitude of the back-scattered signal and c is the speed of light. The received signal is down-converted with its corresponding carrier frequency and then sampled in the baseband. The normalized sample of the baseband signal is

$$s_b(m, n) = \exp[j4\pi f_0 R(m)/c] \cdot \exp[-j4\pi n\Delta f R(m)/c] \quad (5-4)$$

The pulse compression can be readily realized by performing IFFT on each frame, after which we can acquire the m^{th} high range resolution profile (HRRP), expressed as

$$S_b(m, k) = \exp[j4\pi f_0 R(m)/c] \exp[-j\pi(N-1)(k_m - k)/N] \cdot \frac{\sin[\pi(k_m - k)]}{\sin[\pi(k_m - k)/N]} \quad (5-5)$$

where $k = 0, 1, \dots, N-1$ denote samples along fast-time range, $k_m = \lceil 2RN\Delta f/c \rceil$, and $\lceil \cdot \rceil$ is a ceiling function. According to (5-5), the vital signs can be acquired by extracting the phase information of the k_m -th sample for each compressed pulse along slow-time range bin. It is worth mentioning that with the increased bandwidth in a wideband radar system, amplitude and phase distortion will be significant, which may cause dispersion of HRRP and elevation of the side-lobe level. Assuming the distorted amplitude and phase for each frequency point are a_n and ϕ_n , respectively, then (5-4) can be modified as

$$s_b(m, n) = a_n \exp\left[j\frac{4\pi f_0 R(m)}{c}\right] \exp\left[-j\frac{4\pi n\Delta f R(m)}{c} + \phi_n\right] \quad (5-6)$$

a_n and ϕ_n can be measured with a closed-loop configuration of the SFCW radar system, or by placing an ideal point target along the line of sight of the radar. In this manner, the amplitude and phase distortions can be compensated for in the signal processing, i.e. *calibrated*.

Suppose that N pulses are collected by SFCW radar and the sequence of phases extracted from these pulses is given by $y(n)$, $n = 0, 1, 2, \dots (N-1)$. The steps in applying SSM to $y(n)$ are summarized in Chapter 2 from (2-23) to (2-33). Moreover, SSM can be used in combination with phase compensation methods to detect vital signs of targets with random motions [31].

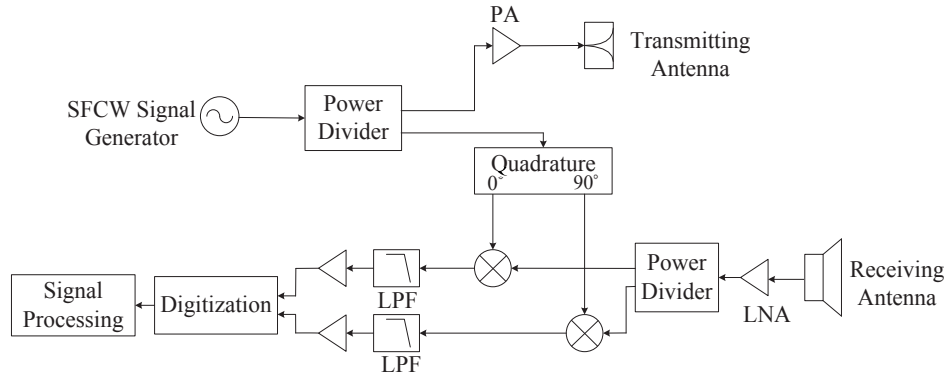


Figure 5.1 Block diagram of SFCW radar system.

5.3 Two-Channel SFCW Radar System Integration

The first generation of two-channel SFCW was built from off-the-shelf discrete components. However, this radar prototype is not suitable for portable application and scenarios requiring hand-held devices, e.g., battle field triage and behind-wall detection. The second generation of SFCW radar is integrated on FR4 boards and Rogers 4350 laminate and separate boards can be stacked up. The components used for the integrated boards are listed in Table 5.1.

The SFCW radar with PCB stack-up configuration is shown in Figure 5.2. It has five layers, transceiver board, diplexer board, PLL, dc supply and DDS board. Figure 5.3 shows the layout of the transceiver board and fabricated transceiver board. To avoid the EMI problem, the RF components on the transceiver board are sparsely populated on the Rogers 4350 laminate. The diplexer board with LNA and PA is presented in Figure 5.4. Since this radar system is geared towards wide bandwidth, two branches of the diplexer are designed to cover pass-bands of 2-3 GHz and 3-4 GHz. For wideband filter design, strong coupling between microstrip parallel line is needed, which requires small gap size between parallel lines. Considering the fabrication capability of manufacturer, we design the diplexer on FR4 board with 63 mil thickness.

Table 5.1 Components used for SFCW radar

Component	Model	Vendor	Specifications
Gain block	HMC589A	Analog Devices	dc-4 GHz, gain 21 dB, P1dB output 21 dBm
Gain block	MGA-30789-BLKG	Broadcom	2-6 GHz, gain 8.8 dB, P1dB output power 25 dBm
Power amplifier	TGA2597-SM	Qorvo	2-6 GHz, 24 dB gain, P1dB output power 32 dBm
Low noise amplifier	HMC639	Analog Devices	0.2-4 GHz, noise figure 2.3 dB, P1dB output power 22 dBm
Mixer	HMC213	Analog Devices	double-balanced mixer, 1.5-4.5 GHz, conversion loss 9 dB
Quadrature splitter	QCS-332+	Mini Circuits	2 Way-90° 50Ω 2500 to 4500 MHz
Splitter	GP2Y1	Mini Circuits	2 Way-0° 1550 to 4400 MHz

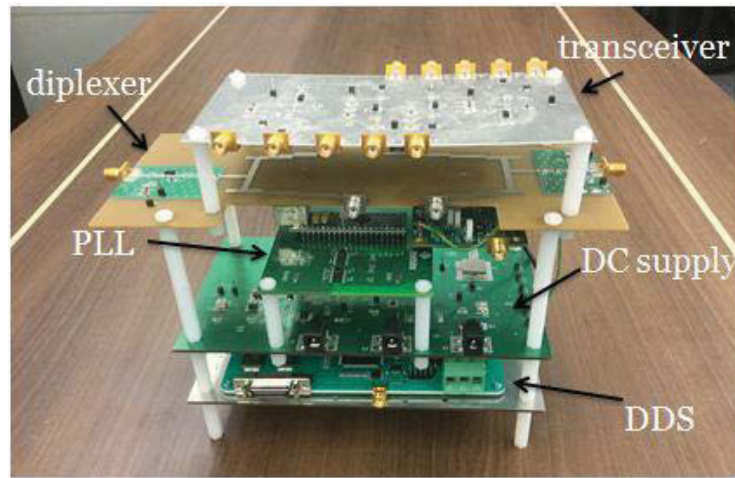


Figure 5.2 Stack-up implementation of two-channel SFCW radar system.

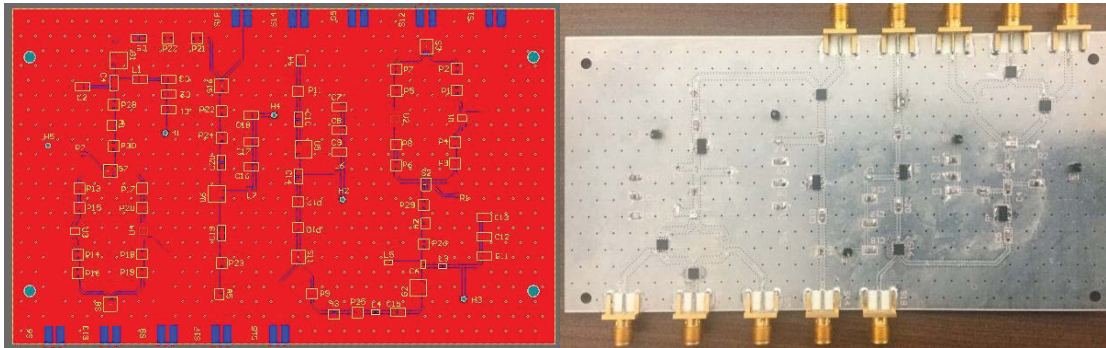


Figure 5.3 (a) Layout of transceiver board; (b) fabricated transceiver board.

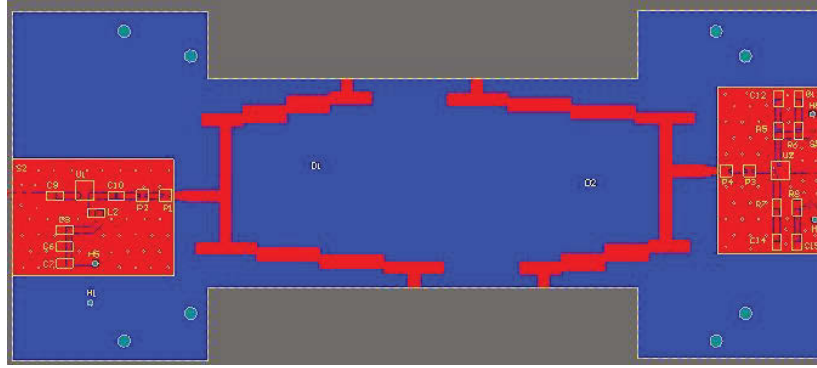


Figure 5.4 Layout of diplexer board with LNA and PA.

Table 5.2 Dynamic range analysis of the transceiver

Parameters	Values
Transmitter Total Power (dBm)	30
Rx 1dB Compression Point (dBm)	12
Rx Thermal Noise Floor (dBm/MHz)	-114
Receiver Bandwidth	2
Receiver Thermal Noise Floor (dBm)	-81
Receiver Noise Figure (dB)	4
Receiver Noise Floor (dBm)	-77
Required SNR (dB)	6 (for acceptable image quality)
Receiver Sensitivity (dBm)	-71
Receiver Dynamic Range (dB)	83

The dynamic range analysis of the radar transceiver is shown in Table 5.2. The thermal noise floor of the receiver is -114 dBm/MHz. The radar receiver has a bandwidth of 2 GHz and therefore, the noise floor of the radar receiver is -81 dBm. The receiver has a noise figure of approximately 4dB, which is mainly due to the cable loss, connector and the noise figure of low noise figure. This radar system is designed for 2-D imaging and localization purpose as well. The minimum SNR required to reconstruct an acceptable imaging quality is 6dB. Subsequently, we can acquire the radar receiver sensitivity to be -71 dBm. Since the receiver 1dB input compression point is 12 dBm, the receiver has a dynamic range of as large as 83 dB.

5.4 Experimental Results

A frequency synthesizer, based on direct digital synthesizer-driven wideband PLL architecture has been designed, which can achieve fast frequency hopping. Commercially available belt sensor and pulse sensor have been used as references for respiration and cardiac rates, respectively. The experimental setup is shown in Figure 5.5.

5.4.1 Subject holds breath

In this experiment, the subject is holding breath and sitting 1 m away from the radar. The directly demodulated heartbeat signal of this subject is shown in Figure 5.6, which matches reasonably well with the reference measurement in peak location. Figure 5.7 shows the detected heart rates estimated using FFT and SSM, and both methods show good performance since there is no thorax motion caused by respiration. However, SSM is observed to have a cleaner spectrum with no spurious peaks. Furthermore, SSM clearly filters the heart rate of the subject even in the presence of random body motion noticed in the FFT spectrogram in Figure 5.7 (a).

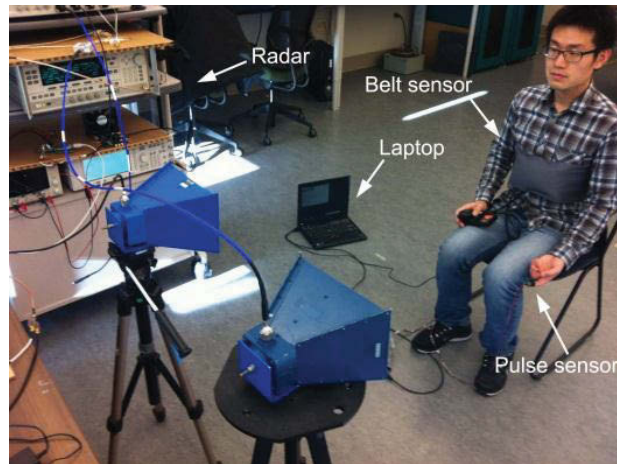


Figure 5.5 Experimental setup.

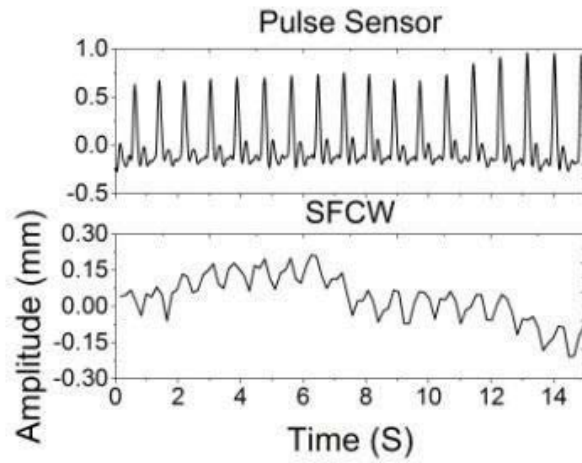


Figure 5.6 Demodulated heartbeat signal of the subject.

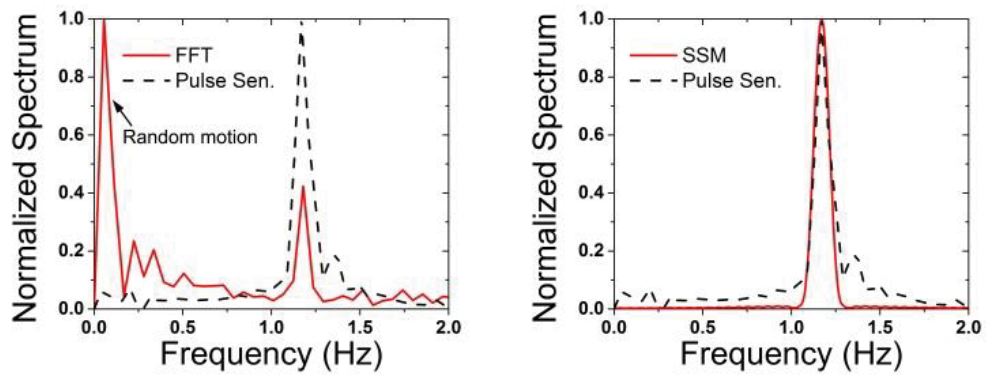


Figure 5.7 Detected heart rate of Subject 1 (a) with FFT, (b) with SSM.

5.4.2 Subject breathes normally

In this scenario, the subject is sitting 1 m away from the radar and breathes normally during the experiment. It is shown in Figure 5.8 (a) that due to low SNR and harmonics of respiration, the heart rate cannot be detected with conventional FFT method. However, as shown in Figure 5.8 (b), using SSM the heart rate can be clearly detected without introducing unwanted intermodulation products, and the error of detected heart rate in comparison with the pulse sensor is 1.2%.

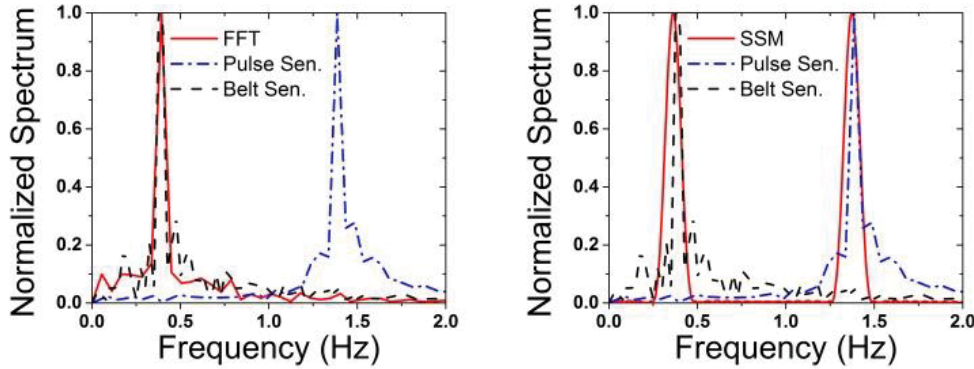


Figure 5.8 Subject breathes normally. Detected vital signs of subject (a) with FFT and (b) with SSM.

5.4.3 Subject facing radar at different angles

The heart rates of the subject facing radar from different angles (shown in Figure 5.9) are detected using SSM. The subject breathes normally and stays 0.6 m away from the radar. As summarized in Table 5.3, using SSM we observe low error when the subject is facing the radar with his back (1.5%) or front (1.6%), and greater error (5.7%) in Position (d) for side-on illumination, where the subject has lower radar cross section (RCS). At right 45° (Position (a)), the lowest error is obtained, since the subject's heart is closest to the radar at this position, while at left 90° (Position (d)), the highest error results since the subject's heart is farthest from the radar. In general, we corroborated that the SSM is capable of accurately identifying the cardiac rates of subjects at different sedentary positions without introducing spurious intermodulation.

5.5 Discussion and Summary

An SFCW radar system samples the frequency domain, while UWB radar samples the time domain, to retrieve the backscattered signal. The difficulty in building UWB radar is in the receiver design, as it requires fast ADCs, while in SFCW radar; it is in the transmitter design as it requires a stable, accurate stepped frequency generator. Both radars should have similar capabilities.

In extracting vital signs from radar measurements, typical FFT transform methods are not accurate enough for heart rate extraction. In this chapter, the

state space method, originally developed for radar signal processing and target identification, has been successfully applied to extract respiration and heart rates. Experimental results have successfully verified advantages of SSM over conventional FFT method in the avoidance of unwanted harmonics and intermodulation products. The validity of SSM has been established by the relatively small error ($< 1.2\%$) observed in the heart rate estimates for a sedentary breathing subject, and even in the presence of controlled body motion with the breathing subject facing the radar at different angles.

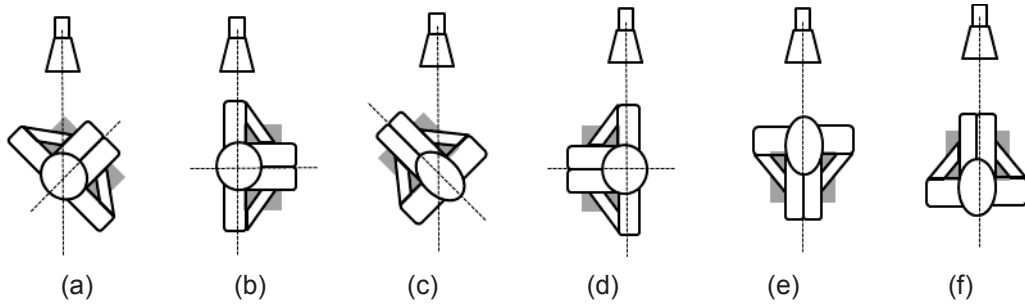


Figure 5.9 Subject at different positions. (a) right 45°; (b) right 90°; (c) left 45°; (d) left 90°; (e) back and (f) front.

Table 5.3 SSM error in heart rate for subject (Right means the body turned right relative to the zero position (front))

Angles	Error (%)
a) Right 45°	0.4
b) Right 90°	3.2
e) Back	1.5
c) Left 45°	3.4
d) Left 90°	5.7
f) Front	1.6

CHAPTER SIX ⁵

COMPARISON STUDY OF NON-CONTACT VITAL SIGNS DETECTION USING A DOPPLER STEPPED-FREQUENCY CONTINUOUS WAVE RADAR AND CAMERA-BASED IMAGING PHOTOPLETHYSMOGRAPHY

In this chapter, we compare the performance of radar and optical (camera-based) techniques in detecting vital signs such as respiratory rate, heart rate, and blood oxygen saturation (SpO_2). Specifically, we investigate the application of ultra-wide band (UWB) stepped-frequency continuous wave (SFCW) radar and imaging photoplethysmography (iPPG) techniques to measure vital signs. The radar performance can be enhanced by using phase information of backscattered signals instead of its amplitude. On the other hand, the iPPG system can be enhanced by using more than one camera and utilizing very selective narrow-band filters coupled with good illumination. In either system, use of advanced signal processing is required to improve accuracy. Generally, heart and respiratory rates can be accurately read by either microwave radar or optical techniques with 500 lx illumination level to have $< \pm 2\%$ error up to 2 m distance between the subject and the system, but optical technique errors increase significantly to $< \pm 15\%$ for < 200 lx. However, each system has its own unique advantages as the radar can be used for seeing-through walls and optical technique is uniquely capable of measuring SpO_2 at this time.

6.1 Background

The respiratory rate (RR), heart rate (HR), and blood oxygen saturation (SpO_2) are critical physiological parameters for human health monitoring. The conventional contact techniques, including electrocardiography (ECG), and photoplethysmography (PPG) may cause discomfort and epidermal stripping, as may be the case in the application of baby apnea monitors or in patients with significant burn wounds. There is a need, then, to develop accurate and efficient non-contact vital sign detection methods that can be used in a diverse number of scenarios, including infant sleep apnea monitoring, daily elderly care, and even round-the-clock monitoring of patients with suicidal ideation.

For Radars, several accurate non-contact methods using various types of

⁵ I worked on this chapter with Lingqin Kong from Beijing Institute of Technology, Haofei Wang from Tsinghua University, Paul Theilmann from MaXentric Technologies Inc., and Farnaz Foroughian from University of Tennessee, Knoxville.

Doppler radar have been proposed recently for the remote triage monitoring of HR and RR [3, 4, 6-14, 16-18, 23, 25, 28-35, 44, 127]. For example, Continuous Wave (CW) radars have been successfully implemented for vital sign monitoring [7-14, 17, 18, 31, 32] and can be extended to long distances, up to 69 meters [16].

However, despite its relatively simple hardware, CW radar transmitting single-tone frequency has a narrow bandwidth; hence its spatial resolution is limited. Additionally, these CW radars necessitate the calibration of the dc offset and require balancing in-phase (I) and quadrature-phase (Q) channels for satisfactory performance [128, 129].

Meanwhile, UWB radars are widely used in many non-contact scenarios such as locating subjects under physical barriers including debris and behind walls. They have also been used to monitor athletes' vital signs remotely [23, 33, 34, 44]. UWB impulse radar transmits a wide-band signal, such as a narrow pulse in the time domain, providing both range and accurate Doppler information of the target. For achieving even higher accuracy, tracking of phase variations of the reflected signals, instead of only their amplitudes, can be used. In [48], for example, a complex signal demodulation and an arctangent method were extended to UWB radar signal processing based on the phase variations of backscattered pulses caused by cardiac motion. However, the transmitted power of UWB radar is limited and is accompanied by relatively high noise accumulated over its wide band causing a low signal-to-noise ratio (SNR), making it difficult to detect. Additionally, UWB impulse radar requires high-speed analog-to-digital converters, which inevitably increases its complexity in system design and hardware cost.

Alternatively, Frequency-Modulated Continuous Wave (FMCW) radar, which overcomes both the drawbacks of CW and UWB impulse radars, has also been successfully applied to non-contact vital sign detection and subject localization [4, 25]. Since it transmits a CW signal, a relatively high power can be transmitted with high SNR and without a need for high-speed analog to digital converters (ADCs). However, it still requires calibration to compensate for the non-linearities in frequency sweeping [26, 27].

On the other hand, stepped-frequency continuous wave (SFCW) radar has been utilized for short-range vital signs monitoring [28-30, 35, 127]. Compared with a CW radar system, SFCW radar is capable of localization, thereby allowing for multiple subjects monitoring in real time. Generally, SFCW can be designed to have similar performance as it provides UWB pulses in the frequency domain; hence should provide comparable capabilities as UWB systems. However, it utilizes low-speed ADCs because of its narrow instantaneous bandwidth. Furthermore, some of its frequencies can be skipped or even randomly selected, which enables compressive sensing implementation for even faster detection [30]. SFCW transmits relatively long duration signals, hence their received signals are significantly stronger than UWB radar and should have higher SNRs in vital signs detection. Furthermore, compared with FMCW radar, it is easier to

calibrate signal distortion caused by any imperfection of the SFCW radar system hardware.

Alternatively, HR and RR can be measured using imaging PPG (iPPG). IPPG is an optical method that measures the small changes in skin color that are the result of changes in blood volume in arteries and capillaries caused by the cardiac cycle. IPPG utilizes imaging devices such as cameras to measure these changes and provide information on cardiovascular status. IPPG is based on the principle that blood absorbs more light than its surrounding tissues. Therefore, by measuring variations in reflected light, as caused by variations in blood volume, we may be able to ascertain HR and RR. Hence, variations in blood volume affect light transmission/reflection [130] and are related to HR and RR. In [131], the feasibility of HR and RR detection using a simple webcam was demonstrated. Both HR and RR have been successfully identified using a color camera in a well-lit room [132]. This method was also shown to be effective in the detection of multiple subjects' HR and RR [133].

Moreover, a method has been developed to measure SpO_2 at optical frequencies using two cameras under regular lighting conditions [130]. The two cameras capture two PPG signals simultaneously at two different wavelengths and these signals are successfully utilized to measure SpO_2 and even HR and RR. The HR and RR measurements demonstrated a high level of confidence [134]. Similarly, SpO_2 results were compared to the traditional method, known as the finger blood volume pulse (BVP), as it was found to have consistent and comparable measurements [130].

The accuracy of radar techniques may suffer from the orientation or motion of either the subject or the radar, which could be rectified by utilizing motion cancellation techniques that are based on optical techniques. In [135], for example, an experiment was conducted to monitor the vital signs of a human subject lying on the ground using CW radar. The HR and RR were clearly identified in the supine and side positions. Meanwhile, in [136] and [137], the performance of a Doppler radar was validated by detecting the vital signs of subjects with different orientations, whereas the work of Li *et al.* indicated that the best accuracy in heart rate monitoring was observed when measuring from the back of the subject. It is an objective to develop a position-free vital signs monitoring process. In [138], the 8th-level decomposition of Bior2.4 for position-free vital signs detection shows high performance in providing the heartbeat signal in time domain where high accuracy is obtained in terms of heartbeat rate. In order to improve the quality of detecting the respiration signals, the self-correlation and adaptive line enhancer (ALE) methods were proposed in [139] to minimize the interferences of any moving objects around the human subject and it could be extended for alignment problems as well.

Many researchers compared their measurements to that using a reference sensor. In the work of Kuutti *et al.* [137], for example, the mean ratios of the pulse rates detected from the radar system, respiration reference sensor and ECG were 110% (i.e., +10% error for respiration) and 99% (i.e., -1% error for

heart beat). The error could be related to motion, and a motion cancellation system needs to be used for real time measurements. To address the random body motion cancelation, a hybrid radar-camera system has been developed for accurate human vital signs monitoring [31], where a camera is used to measure the scene's phase information and an adaptive phase compensation algorithm is used to cancel subject's motion with respect to the radar.

Recently, we have been focusing on developing non-contact vital signs detection using UWB radar systems [49, 52, 53, 140-142]. Additionally, in search for a viable method to remotely detect SpO₂, we have investigated iPPG technique [130]. Both methods were briefly compared as well [143]. Here, we extend this work to provide a detailed comparison between these two techniques, shed some light on their capabilities and limitations, additionally, results were compared to contact measurement methods to validate measurements and present comprehensive error analysis.

This chapter is organized as follows: in Chapter 6.2, we describe in detail the basic principles of vital signs detection and focus on major challenges to extracting vital signs. In Chapter 6.3, we describe our experimental set-up, which is composed of SFCW radar and the iPPG system in order to compare their performance. In Chapter 6.4, we present our experimental evaluation with a single sedentary subject utilizing both systems, while all results are validated with corresponding contact reference sensors. Finally, we discuss the advantages and limitations of Doppler radars and iPPG in remote vital sign detection and conclude.

6.2 Operating Principle of SFCW Radar and IPPG System

Generally, SFCW radars monitor the variations of torso displacement caused by heartbeat and respiration motions. Meanwhile, iPPG detects blood volume changes in the micro-vascular bed of tissues, which can provide valuable information about the cardiovascular system. The operating principles of both SFCW radar and iPPG system for vital signs monitoring are briefly described here.

6.2.1 SFCW radar

The SFCW radar transmits a series of frames, where each frame is comprised of N pulses. The radar linearly steps up the frequencies of these pulses by a fixed frequency step Δf . The transmitted signal in one frame can be represented by

$$s_{Tx}(t) = \frac{1}{\sqrt{T}} \sum_{n=0}^{N-1} \text{rect}\left(\frac{t-nT}{T}\right) \cdot \exp[j2\pi(f_0 + n\Delta f)t] \quad (6-1)$$

where T represents the repetition time of the pulse, $\text{rect}(\cdot)$ is the symbol for rectangular function, t is the fast time sampled by ADC while the carrier frequency of the first pulse is f_0 , and n represents the frequency step.

If we assume the distance between the subject and radar transceiver is noted by $R(\tau)$, where $R(\tau)$ is function of slow time τ , i.e., the frame number, the received signal $s_{Rx}(t)$ for the subject at $R(\tau)$ can be expressed as

$$s_{Rx}(t) = a \cdot s \left(t - \frac{2R(\tau)}{c} \right) \quad (6-2)$$

where a is the amplitude of reflected signal, c is the speed of light and $R(\tau)$ is the instantaneous range of the subject. Note that $R(\tau)$ is composed of both the static distance between subject and radar and a time-varying distance due to torso displacements.

Subsequently, the received signal is mixed with its corresponding carrier frequency and down converted. Then the down-converted signal is given by

$$\begin{aligned} s_b(t) &= s_{Tx}(t) \cdot (s_{Rx}(t))^* \\ &= \frac{a}{T} \sum_{n=0}^{N-1} \text{rect} \left(\frac{t - nT - 2R(\tau)/c}{T} \right) \\ &\quad \cdot \exp \left[j \frac{4\pi f_0 R(\tau)}{c} + \frac{4\pi n \cdot \Delta f \cdot R(\tau)}{c} \right] \end{aligned} \quad (6-3)$$

where $()^*$ indicates complex conjugate. The signal is down-converted to baseband, which alleviates the sampling rate requirement for ADC. The term $4\pi f_0 R(\tau)/c$ represents the slow-time migration phase history of the subject. To acquire the high range resolution profile (HRRP), inverse fast Fourier transform (IFFT) is applied on each frame of the baseband signal to realize pulse compression. HRRP can then be expressed as

$$\begin{aligned} S_b(f) &= \frac{a}{NT} \exp \left(\frac{j4\pi f_0 R(\tau)}{c} \right) \cdot \exp \left(\frac{j2\pi(N-1)}{N} \cdot (f - N\Delta f \cdot 2R(\tau)/c) \right) \\ &\quad \cdot \frac{\sin \left[\pi (f - N\Delta f \cdot 2R(\tau)/c) \right]}{\sin \left[\frac{\pi}{N} (f - N\Delta f \cdot 2R(\tau)/c) \right]} \end{aligned} \quad (6-4)$$

The range information of the subject can be acquired with proper scaling of frequency. When HRRP reaches its peak value at $f_p = N\Delta f \cdot 2R(\tau)/c$, (6-4) becomes

$$S_b(f_p) = \frac{a}{T} \exp \left(\frac{j4\pi f_0 R(\tau)}{c} \right) \quad (6-5)$$

According to (6-5), upon extracting the phase information at f_p for each compressed pulse along slow-time range bin, vital signs can be detected. An algorithm to extract the range information and vital signs is briefly described here.

Suppose that the SFCW pulse within each frame is sampled and saved in rows, which constitutes the raw-data matrix $M(g,h)$, where $g = 1, 2, \dots, G$ denotes index of transmitted frames along slow-time dimension, $h = 1, 2, \dots, H$ denotes the index of ADC samples along fast-time dimension. The signal processing to extract range information of the subject is summarized in the following steps:

Step i) Perform IFFT over each row of the raw-data matrix $M(g,h)$. Denote this resulting HRRP matrix as $J(g,h)$.

Step ii) Determine the range bin which the subject traverses for each row of $J(g,h)$ by finding its corresponding peak values. Save these complex numbers as signal $L(g)$.

Step iii) Extract and unwrap the phase information of the signal $L(g)$. Denote this result as $\psi(g)$.

Step iv) Estimate the range history of subject as $R(g) = c\psi(g) / 4\pi f_0$.

Step v) Apply Fast Fourier Transform (FFT) spectral analysis to $\psi(g)$ for the respiratory and heart rates.

6.2.2 iPPG system

The iPPG waveform is related to the pattern of visible light absorption by blood and is comprised of dc and ac components [130]. The reflected optical signal from the tissue has a dc component that slowly varies due to respiration. Meanwhile, its ac component, which shows pronounced change, is related to the blood volume change during the systolic and diastolic phases of the cardiac cycle. The heart rate is associated with the fundamental frequency of the ac component. Figure 6.1 shows the process of evaluating vital signals (HR and RR) based on the iPPG system and the process of acquiring PPG signal. To extract HR and RR, we recorded a video zooming on the human face. The video recorded by a camera is converted to an image sequence frame-by-frame. In each frame, a region of interest (ROI) is defined to study blood perfusion underneath the skin. The ROI is tracked in successive frames using averaging to provide the average pixel intensity values. Suppose $y_k(t)$ is the intensity of the k^{th} pixel within the ROI at time t , where $k = 1, 2, \dots, K$. Then the PPG signal $p(t)$ is estimated as

$$p(t) = \frac{1}{K} \sum_{k=1}^K y_k(t) \quad (6-6)$$

Upon using FFT of PPG signal, the respiratory and heart rates can be identified. Conversely, for the measurement of SpO_2 , we record the cardiovascular pulse wave signals (PPG signals) at two different wavelengths, λ_1 and λ_2 . We use two different cameras, each attached to very narrow-band filters, with one at λ_1 and

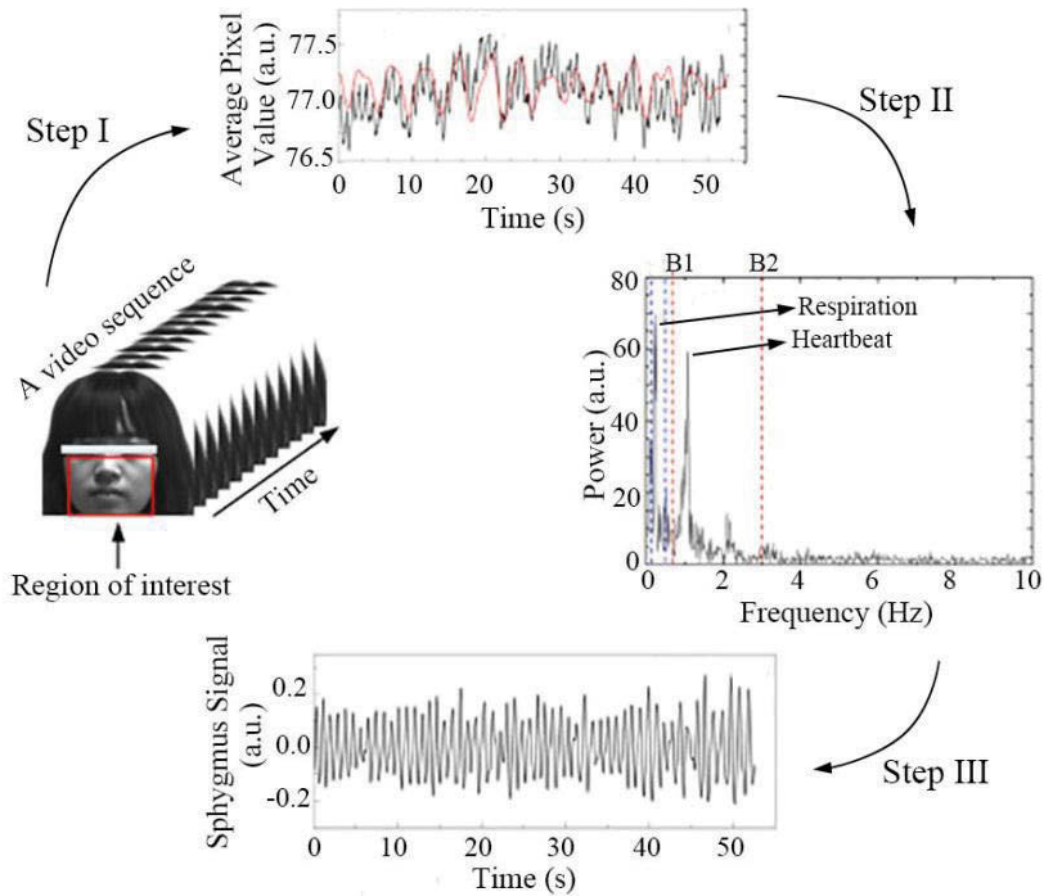


Figure 6.1 Process of extracting vital signs from video recorded by camera; Step I: take average from all pixels of each video frame and plot it in time; Step II: filter the signal with a band-pass filter; Step III: acquire the PPG signals after band-pass filtering.

the second at λ_2 . Blood oxygen saturation SpO_2 is defined as the ratio of the intensity of oxygenated hemoglobin in blood (HbO_2), to the sum of the oxygenated hemoglobin HbO_2 and the deoxygenated hemoglobin Hb , i.e.,

$$SpO_2 = \frac{HbO_2}{HbO_2 + Hb} \times 100\% \quad (6-7)$$

In our case, blood oxygen saturation can be measured using the maximum reflections at the two wavelengths, i.e., $I_{DC}^{\lambda_1}$ and $I_{DC}^{\lambda_2}$, and the maximum variables of reflections' intensity caused by pulsation, i.e., $I_{AC}^{\lambda_1}$ and $I_{AC}^{\lambda_2}$, (namely $\lambda_1= 660$ nm and $\lambda_2=520$ nm) [130], where

$$SpO_2 = A \frac{I_{AC}^{\lambda_1} / I_{DC}^{\lambda_1}}{I_{AC}^{\lambda_2} / I_{DC}^{\lambda_2}} + B = A \cdot R + B \quad (6-8)$$

$$R = \frac{I_{AC}^{\lambda_1} / I_{DC}^{\lambda_1}}{I_{AC}^{\lambda_2} / I_{DC}^{\lambda_2}} \quad (6-9)$$

The two wavelengths are selected so that the absorption coefficients of HbO_2 and Hb at one of these wavelengths differ greatly, but are approximately equal at the other wavelength (here we selected 520 nm and 660 nm). SpO_2 values are estimated by calculating the ratio of ratios, R , at 660 nm and 520 nm wavelengths according to (6-8) where the constants A and B are empirically determined by calibration. The peak-to-peak values of the PPG signals over a certain period of time after de-noising and filtering are used to determine the ac signal, I_{AC} , while the dc component, I_{DC} , is computed by averaging values of the PPG signals over the same period of time. However, the peak-to-peak value extracted from the PPG signal in each cycle also varies due to noise even when the blood saturation remains unchanged. Subsequently, a moving average window of 10 s is applied to the ac and dc components; to calculate I_{AC} , rather than utilizing a peak-to-peak value of each cardiac cycle.

6.3 Experimental Setup

The block diagram of the utilized experimental setup and its picture are shown in Figure 6.2 and its components are summarized in Table 6.1. In this setup, a camera can monitor different areas of the face. By focusing on a region of interest of a subject's face (ROI) in the captured video, the iPPG system has the capability of extracting respiratory rate, heart rate, and SpO_2 .

6.3.1 SFCW Radar Implementation

SFCW records a signal replica of chest tiny motion. To obtain accurate phase information of this recorded signal, it is mandatory to make the SFCW radar coherent and have phase control in the waveform generation and in data

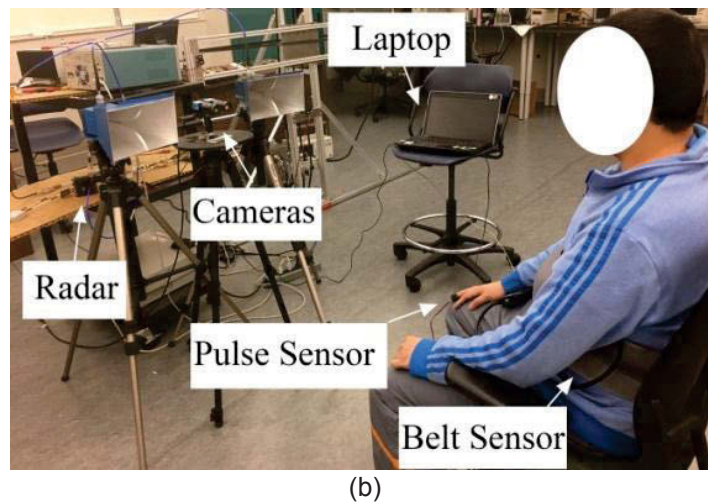
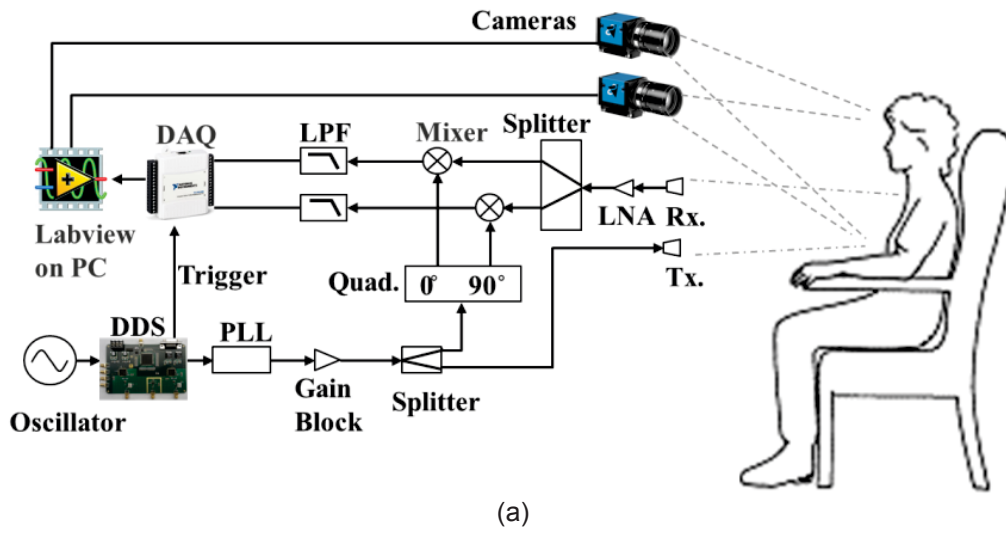


Figure 6.2 (a) Block diagram of the experimental setup. (b) Experimental setup in lab.

Table 6.1 Components used in experimental setup

Block	Manufacturer & Model	Features
PLL	Analog Device HMC833	fractional-N PLL with integrated VCO 25-6000 MHz
Oscillator	Keysight E4421B	output at 1.2 GHz, output level 3 dBm
Gain Block	Mini Circuits ZX60-V63+	0.05-6 GHz, 20 dB gain, 18 dBm output at 1 dB compression point
Splitter	Mini Circuits ZAPD-4-S+	2-4 GHz, 2 way phase difference 0o, 0.4 dB insertion loss
Quad Splitter	Mini Circuits ZAPDQ-4-S+	2-4 GHz, 2 way phase difference 90o, 0.4 dB insertion loss
LNA	Analog Device HMC753	1-11 GHz, 1.5 dB NF @ 4 GHz, 16.5 dB gain
Mixer	Mini Circuits ZX05-C60+	1.6-6 GHz, 32 dB LO to RF isolation, 6.3 dB conversion loss
DAQ	National Instrument NI 6009	Input resolution 14 bits, max sampling rate 48 kbit/s
Camera	The Imaging Source DMK23U 618	sensitivity 0.015 lux, max frame rate 120 fps
Lens	Thorlabs MVL8M23	Diameter 28.2 mm

acquisition of the baseband signal. To achieve this, a customized digital signal synthesizer (DDS) controlled by a complex programmable logic device (CPLD) and phase-lock loop (PLL) are used together to ensure the full control of the initial phase of the generated waveform [30]. Moreover, a trigger signal is generated by the CPLD to synchronize the data acquisition device (DAQ), as shown in Figure 6.3, where a sampling rate of 5 kb/s is used. The data collected from SFCW radar can be processed in real-time using LabVIEW.

The operating pass-band of one channel of the SFCW is 2 GHz – 3 GHz, a second channel can be added and will be from 3 GHz to 4 GHz. The transmitted power is -16 dBm and is transmitted through a horn antenna. According to radar equation, the received signal power can be calculated by

$$P_r = \frac{P_t \cdot G_t \cdot \sigma \cdot A_e \cdot G_r}{(4\pi d^2)^2} \quad (6-10)$$

where P_t is the transmitted power, G_r and G_t are the transmitting and receiving antenna gains, which are around 9.6 dB; σ indicates radar cross section (RCS) of human subject, which is estimated to be $0.3 \times 0.5 \text{ m}^2$; A_e represents receiving antenna aperture, which is $0.14 \times 0.24 \text{ m}^2$; d indicates the distance between subject torso and radar receiver. The thermal noise floor of the receiver is -174 dBm/Hz, or -114 dBm/MHz. Since the radar receiver has a bandwidth of 1 GHz, the noise floor of the radar receiver is -84 dBm. The receiver has a noise figure of approximately 2 dB, which is mainly due to the cable loss and the noise figure of the low noise amplifier (LNA). Subsequently, we can assume the radar receiver sensitivity to be -82 dBm. The SNR of the SFCW radar receiver (SNR_r) is calculated as

$$\begin{aligned} SNR_r &= (P_r + 82) \text{ dB} \\ &= [40 - 40 \log_{10}(d)] \text{ dB} \end{aligned} \quad (6-11)$$

6.3.2 IPPG System Implementation

In the iPPG system, two cameras mounted with different optical filters and controlled by LabVIEW capture two PPG signals from the subject simultaneously and are used to extract SpO_2 information. To ensure high system accuracy, the bandwidth of these optical filters should be as narrow as possible. Mounted filters have a full width at half maximum (FWHM) of 10 nm centered at $660 \pm 5 \text{ nm}$ and $520 \pm 5 \text{ nm}$, respectively. The use of highly selective dual cameras can efficiently suppresses the disturbance of ambient light in other bands. The empirical values of A and B in (6-8) have been experimentally derived by [130] and utilized here.

In our setup, the cameras utilized are DMK23U618 from The Imaging Source with a sensitivity of 0.015 lx. The lenses used are MVL8M23 from Thorlabs with a diameter of 28.2 mm. The cameras record a video of human facial areas and the luminance level received by cameras can be estimated as

$$I_r = \frac{I \cdot A_f \cdot \pi \cdot r^2}{4\pi d^2} \quad (6-12)$$

where I represents the illumination level; A_f represents the estimated facial area, which is around $0.1 \times 0.2 \text{ m}^2$; d indicates the distance between the subject and camera; r indicates the radius of lens, which is 14.1 mm. The SNR of cameras (SNR_c) in recoding the videos can be calculated as

$$\begin{aligned} SNR_c &= 10 \cdot \log_{10} \left(\frac{I_r}{N_p \cdot s \cdot 0.015} \right) \text{dB} \\ &= [8.3 + 10 \log_{10}(I) - 20 \log_{10}(d)] \text{dB} \end{aligned} \quad (6-13)$$

where N_p represents the number of pixels, which is 640×480 ; s indicates pixel size, which is $5.6 \times 5.6 \text{ } \mu\text{m}^2$.

Based on (6-11) and (6-13), the SNRs of SFCW radar and iPPG system were calculated and they vary as function of subject's distance d , and illumination conditions as demonstrated in Figure 6.3. SFCW radar mostly demonstrates higher SNR than iPPG system in a close range, which means higher accuracy in vital signs monitoring, while SNR of iPPG system degrades significantly under poor illumination conditions.

6.4 Experimental Results

6.4.1 Comparison between SFCW radar and IPPG System

In this experiment, data of one subject at 1 m, 1.5 m and 2 m away from the experimental system with four orientations specified in Figure 6.4 have been collected simultaneously by the SFCW radar and the iPPG system. Antennas of SFCW radar and cameras of iPPG system were mounted 110 cm above the ground. The transmitting and receiving antennas were 50 cm apart and the cameras were mounted in the middle between the transmitting and receiving antennas of the SFCW radar. Note that for the iPPG system, when the subject is at the "back" position, the ROI of the captured video is the neck not the face; while when the subject turns right or left, ROI will be the left side of the face and right side of the face of the subject, respectively. The subject (age 31, weight 82 kg and 1.8 m tall) was sedentary at the same distance from the radar receiver and iPPG system. For evaluation, one belt sensor (NeuLog, Carolina Biological Supply Company, Burlington, NC) and one blood volume pulse (BVP) sensor (PulseSensor, World Famous Electronics LLC, New York, NY) were used as references of respiration and heartbeat, respectively. The frame rate of SFCW radar is 20 Hz and the sampling rate of camera is 20 fps. Both SFCW radar and iPPG system collect data for 30 s in the experiment, while the controlled environment illumination is measured by a lux meter (Extech LT300, FLIR

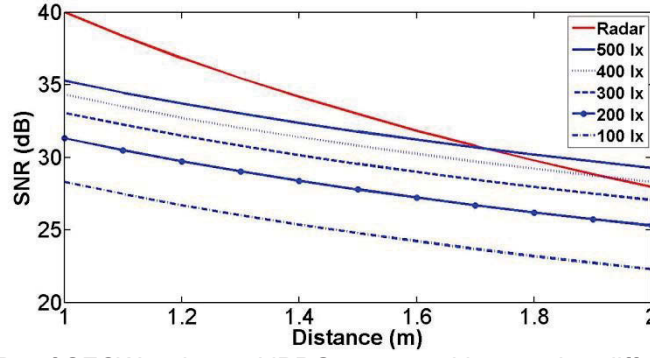


Figure 6.3 SNRs of SFCW radar and iPPG system with regard to different levels of light illumination.

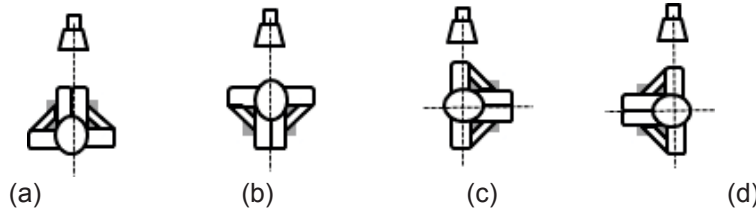


Figure 6.4 Four orientations of subject (a) front, (b) back, (c) right, (d) left.

Commercial Systems Inc., Nashua, NH). The ratio of measurement to reference sensor is calculated as follow,

$$Ratio = \frac{V_M}{V_R} \cdot 100\% \quad (6-14)$$

where V_M indicates measurement result; V_R indicates reading from the reference sensor.

When a subject is 1 m away from the experimental setup at the position “front” and the illumination level is 500 lx, the demodulated signals spectrums from both radar and optical sensor are compared with the results of the corresponding reference sensor, as shown in Figure 6.5. The respiratory and heart reference rates of a subject were 0.23 Hz and 1.35 Hz respectively during the experiment. Both radar and camera demonstrate high accuracies in respiratory and heart rates monitoring. For radar, the corresponding ratios to respiratory and heart reference rates are 100.17% and 99.63% respectively; meanwhile for camera, the ratios to respiratory and heart reference rates are 99.30% and 100%. These differences are less than 1% using either technique in vital signs detection.

The performance of radar and camera in vital signs detection for a subject seen at different orientations and at different distances with 500 lx illumination have been compared and results are shown in Figure 6.6 and 6.7. As shown, both radar and camera have ratios for both respiratory and heart rates detection within $100\% \pm 2\%$ for all orientations up to 2 m. Vital signs of a subject at these different orientations can be clearly extracted using radar, especially when subject is in

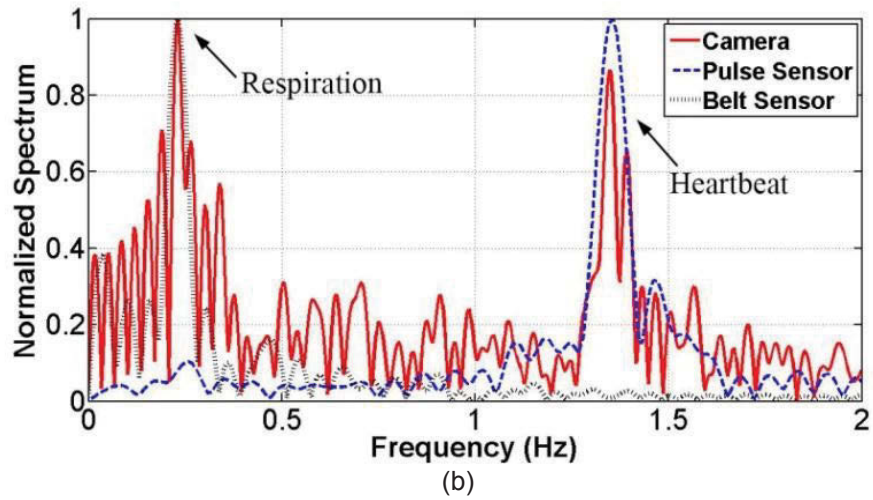
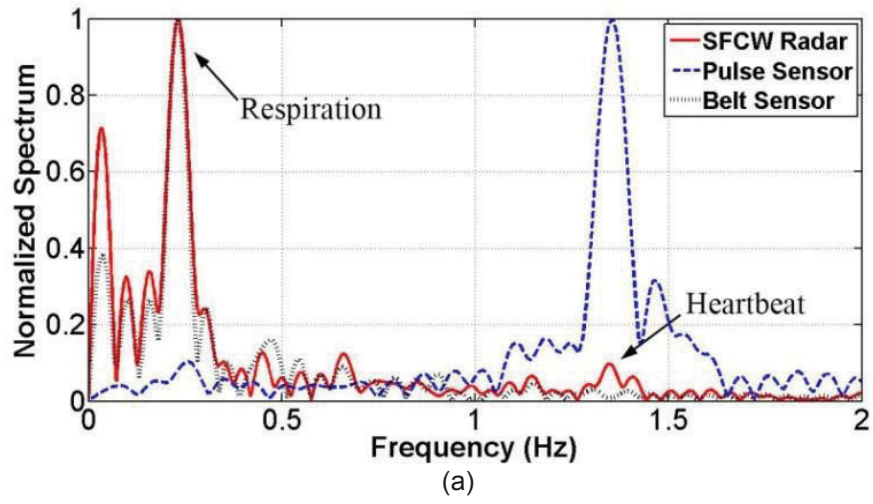


Figure 6.5 Spectra of demodulated signals from (a) SFCW radar, (b) camera with 520 nm filter when illumination level is 500 lx.

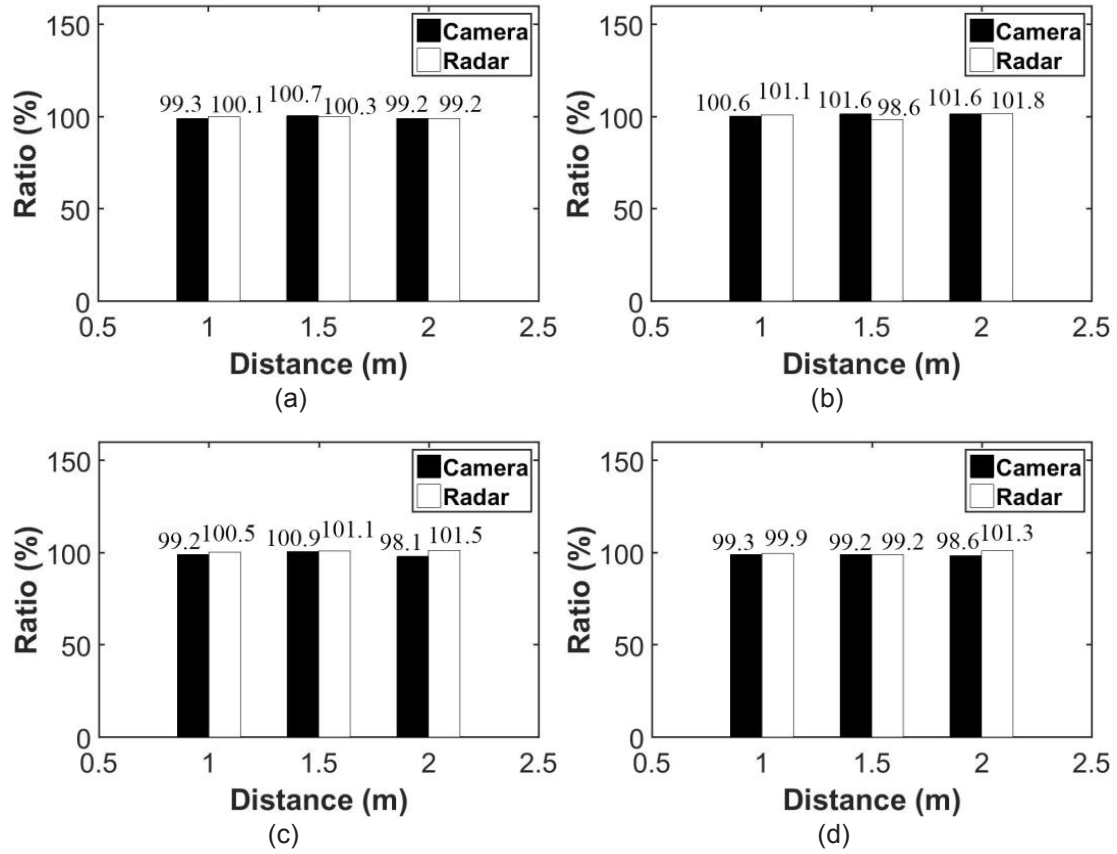


Figure 6.6 When illumination is 500 lx, comparison of ratio to reference using SFCW radar and camera in respiratory rate detection when subject is at orientation of (a) front, (b) left, (c) right, and (d) back.

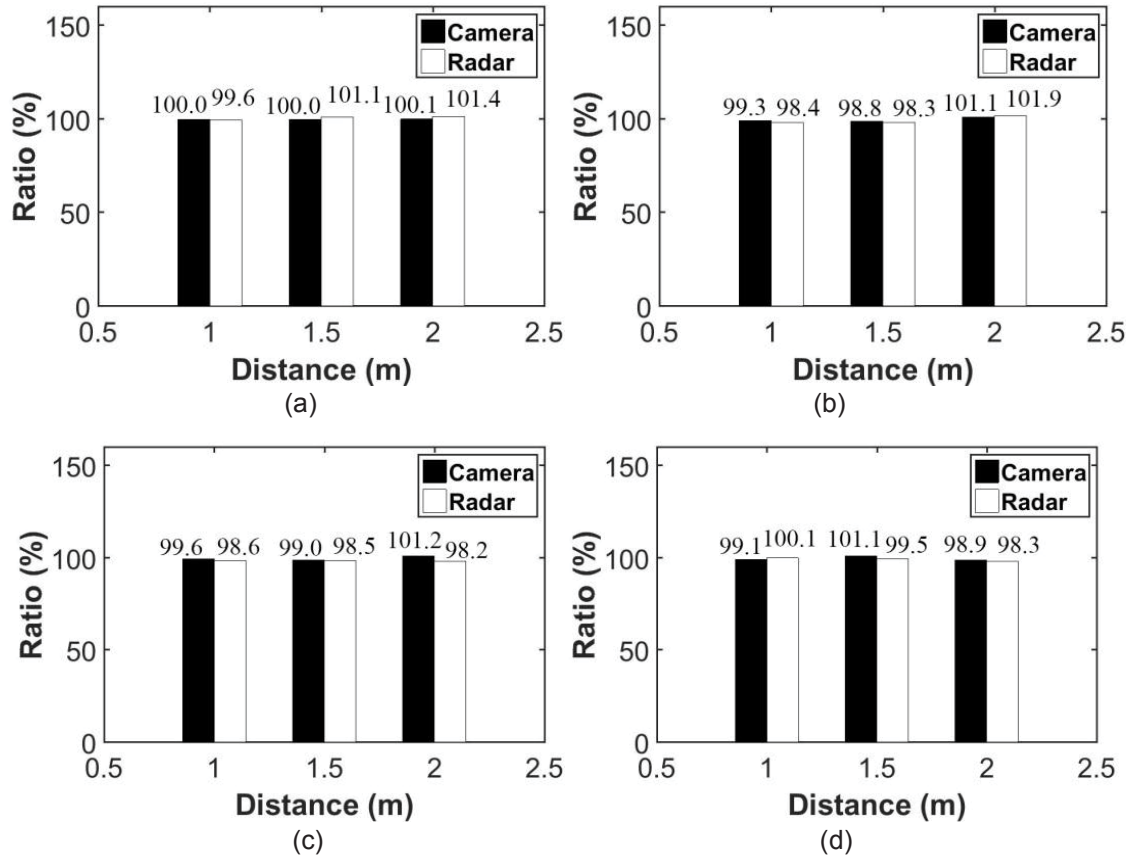


Figure 6.7 When illumination is 500 lx, comparison of ratio to reference using SFCW radar and camera in heart rate detection when subject is at orientation of (a) front, (b) left, (c) right, and (d) back.

close range. It is also observed that camera is capable of accurate vital signs monitoring as long as videos of exposed human skins are captured. This is consistent with our prediction that both radar and camera sensors possess a SNR in the range of 27 dB when the subject is 2 m away under 500 lx illumination, which ensures the accuracy of vital signs detection for both systems. To investigate the influence of illumination level on performance of camera in vital signs detection, another experiment is conducted where the subject is 2 m away for the four indicated orientations (front, right, left, and back) but under different illumination conditions. The results are summarized in Figure 6.8 and 6.9. When the illumination level drops from 500 lx to 200 lx, the accuracy of camera in respiratory rate monitoring degrades by 10% as indicated by the ratio parameter when the subject is at left or right positions, while the accuracy of heart rate detection is not greatly affected. When the illumination level is 100 lx, ratios of respiratory rates extracted by camera degrades to 70%, i.e., -30% difference to reference readings, while the ratio of heart rate is overestimated by 40% when the subject is at the “right” position. Vital signs detected by camera in low illumination level are not reliable. It is worthwhile mentioning that radar is not influenced by illumination conditions as demonstrated in Figure 6.8 and 6.9. The above experiment was then repeated to study the effect of subject distance from the setup, with the subject in “front” position. As shown in Figure 6.10 and 6.11, when the subject is at front position, respiratory and heart rates are readily monitored by camera when lighting level is above 200 lx; when lighting level drops to 100 lx, accuracies for respiratory rates significantly degrade with the increase of subject distance. As shown in Figure 6.11 (c), the ratio of respiratory rate measurement to reference degrades from 97% at 1 m, to 89.93% at 1.5 m and 115.81% at 2 m. This is consistent with the aforementioned predictions in Figure 6.3.

6.4.2 SpO₂ Measurements

As previously indicated, IPPG system is capable of SpO₂ detection as well. The empirical values of A and B in (6-8) were experimentally derived and readings from a BVP sensor (OnyxII, Nonin Medical Inc., Plymouth, Minnesota) serve as a reference. In SpO₂ detection experiments, the subjects were sedentary and stationary at a 1.5 m position away from both cameras. In this experiment, thirty subjects within 18 to 58 years old had participated. The subjects were asked to hold breath. The subjects' SpO₂ generally would fall linearly with time after 22s. Hence, we focused on this linear region and estimated the coefficients A and B with the reading of SpO₂ from a BVP sensor and measured R in (6-9) for the iPPG system. To obtain the empirical coefficients A and B , least square method was utilized to linearly fit these data. Based on [130], substituting A and B in (6-8) leads to,

$$SpO_2 = 125 - 26 \cdot R \quad (6-15)$$

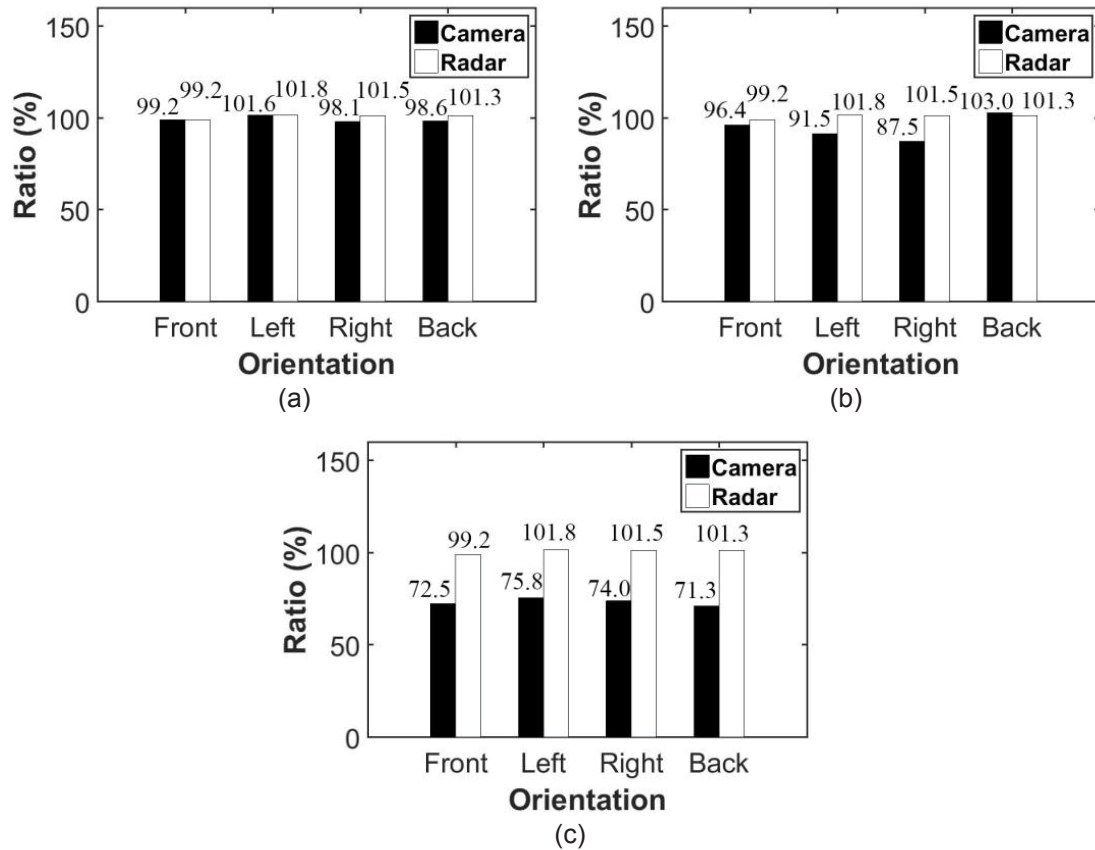


Figure 6.8 When subject is 2 m away, comparison of ratio to reference using SFCW radar and camera in respiratory rate detection when illumination level is (a) 500 lx, (b) 200 lx, and (c) 100 lx.

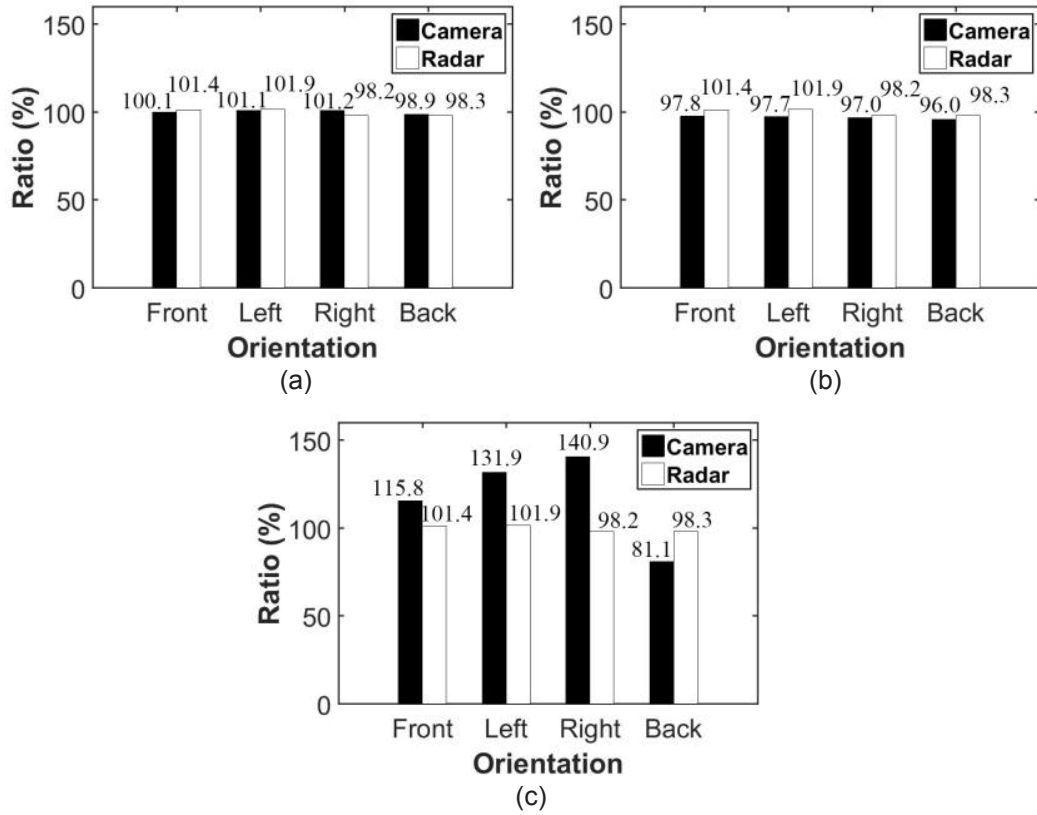


Figure 6.9 When subject is 2 m away, comparison of ratio to reference using SFCW radar and camera in heart rate detection when illumination level is (a) 500 lx, (b) 200 lx, and (c) 100 lx.

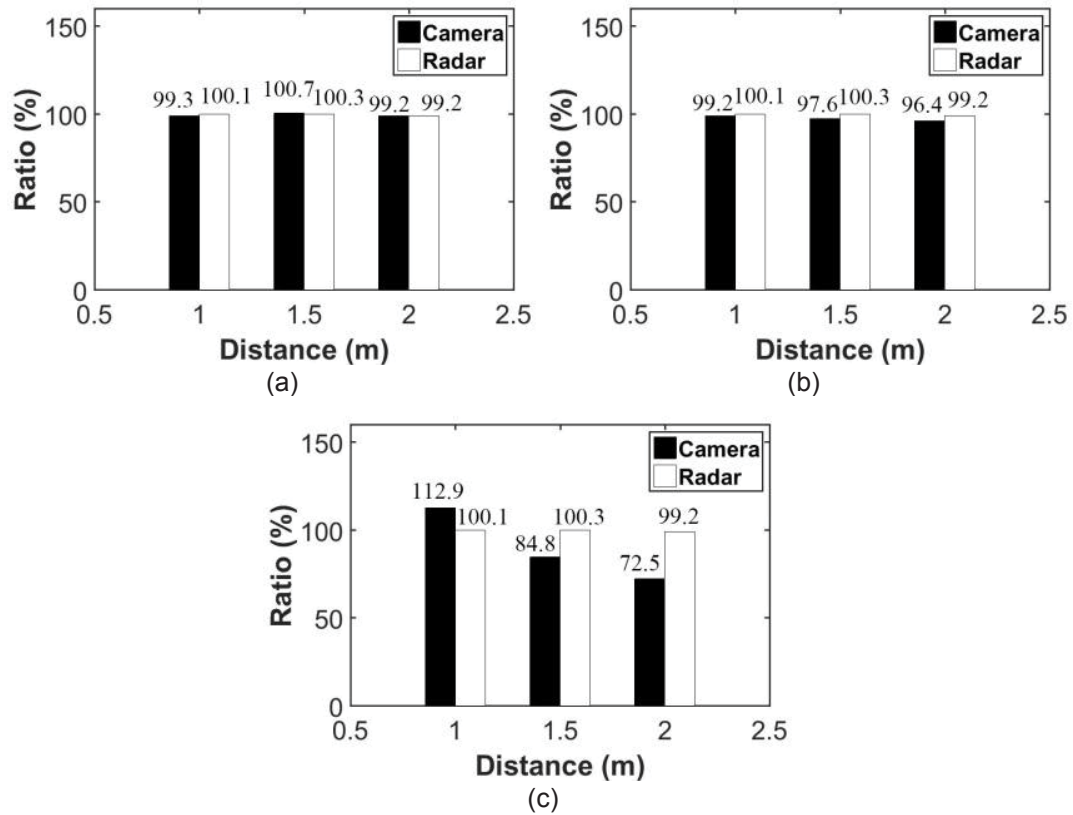


Figure 6.10 When subject is at orientation of front, comparison of ratio to reference using SFCW radar and camera in respiratory rate detection when illumination level is (a) 500 lx, (b) 200 lx, and (d) 100 lx.

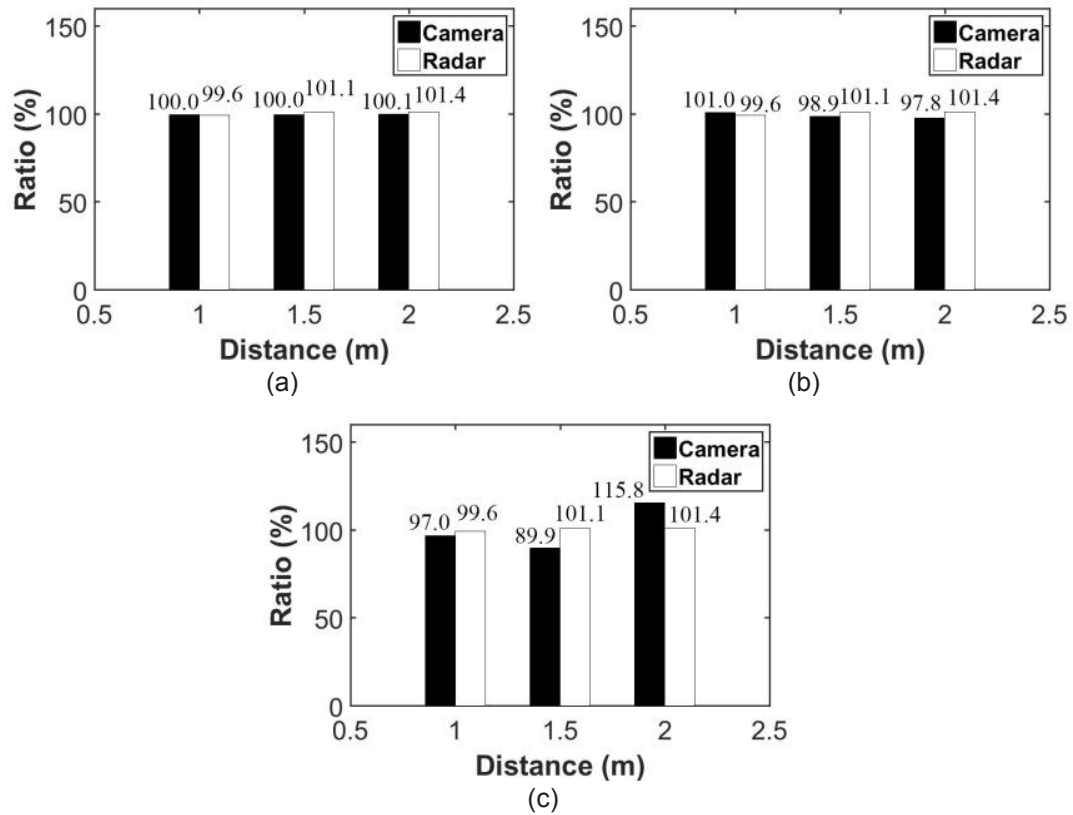


Figure 6.11 When subject is at orientation of front, comparison of ratio to reference using SFCW radar and camera in heart rate detection when illumination level is (a) 500 lx, (b) 200 lx, and (c) 100 lx.

Table 6.2 summarizes the descriptive statistics, i.e., mean bias, standard deviation of bias, upper limit and lower limit, for empirical evaluation of SpO₂ using iPPG compared to the finger BVP at different ambient light intensities [130]. It demonstrates the performance of SpO₂ detection with relatively stable ambient light intensity.

Table 6.2 Mean, standard deviation, upper and lower limits statistics for the ambient light intensity effects on SpO₂

	Ambient light intensity (lx)		
	600	460	320
<i>Mean bias (%)</i>	0.31	0.32	0.35
<i>Sd of bias (%)</i>	1.02	1.05	1.05
<i>Upper limit (%)</i>	2.3	2.02	2.2
<i>Lower limit (%)</i>	-3.1	-3.01	-3.3

6.5 Discussion

Experimental results of vital signs detection using an iPPG system and SFCW radar in close range have been presented. Both the iPPG system and SFCW radar are capable of HR and RR monitoring. However, at this time only the iPPG system has the capability of SpO₂ detection. In some scenarios, optical techniques can be used when a subject's chest is covered and only his/her face is exposed. Conversely, SFCW radar systems have the capability of non-line-of-sight (NLOS) monitoring and, as a result, can see through fog, smoke, foliage and cement walls.

However, for long distances both optical techniques and SFCW radar fail and/or have unacceptable errors. Transmitted SFCW power is relatively low, which would significantly hinder proper detection beyond a few meters for poor SNR. Similarly, optical systems would not be effective as they require extra bright illumination on a subject's face for meaningful detection. Alternatively, CW radar can be used for HR and RR to accurately extract vital signs of a subject for long distances exceeding 50 m [16].

It is worthwhile mentioning here that random motions of subjects may degrade the detection accuracy of vital signs for either radar systems or iPPG system. A camera can be used to cancel random motion, and in the iPPG system a stabilized camera can be used.

6.6 Conclusion

In recent years, researchers have presented a number of new and interesting methods for non-contact physiological parameters detection using iPPG and radar techniques. In our study, SFCW radar and iPPG technologies are briefly reviewed, discussed, and compared. The two methods were utilized for the

Table 6.3 Summary of different radar types for remote detection

Reference	Radar Type	Frequency /Bandwidth	Measurement	Results
[7]	CW	5.8 GHz	RR	RR is measured with 7.15% error when subject is under large 1-D body motion.
[18]	CW	within 4-7 GHz	HR/RR	Random motion is cancelled and heartbeat is recovered in spectrum.
[31]	CW	2.4 GHz	HR/RR	Random body motion is effectively reduced with phase compensation.
[8]	CW	60 GHz	HR/RR	HR and RR are clearly observed when subject is 0.75 m away.
[12]	CW	60 GHz	HR/RR	Vital signs are detected up to 0.3 m.
[32]	CW	60 GHz	HR/RR	At 1 m, RR is detected at four orientations; at 2 m, HR/RR are detected when subject faces front.
[9]	CW	within 2.4-2.5 GHz	HR/RR	HR and RR of 15 subjects at varied distance are accurately extracted.
[10]	CW	12, 24 GHz	HR/RR	When subject is 0.5 m away, HR is detected with error less than 4.4%.
[11]	CW	2.4 GHz	HR/RR	HR and RR can be detected up to 4m.
[14]	CW	2.4 GHz	HR/RR	HR is detected of a subject jogging on a treadmill with random body motion.
[13]	CW	24 GHz	HR/RR	At 1 m, HR and RR of subject can be accurately detected.
[17]	CW	2.4 GHz	HR/RR	Improved HR measurement accuracy with a standard deviation of < 1 beat/min.
[16]	CW	2.45 GHz	HR/RR	Successful measurement of HR and RR of at distances of 21 and 69 meters is made.
[33]	CW /Pulse	1.5-4.5 GHz	RR	Localization and RR of multiple subjects are simultaneously monitored within 3.3 m.
[23]	Pulse	3.1-10.6 GHz	RR	RR of person at 0.25 m and infant at 0.2 m can be successfully detected.
[34]	Pulse	3.1-10.6 GHz	HR/RR	HR and RR of subject at 1 m and behind wall are detected.
[44]	Pulse	dc-2 GHz	victim search	RR of subject under a pile of bricks and a concrete pipe is detected.
[6]	FMCW	75-85 GHz	HR/RR	At 2 m, a median of the relative error of 5.52 % and 14.58% for RR and HR detection respectively on 10 subjects are obtained.
[4]	FMCW /CW	5.72-5.88 GHz	HR/RR	Azimuth information of subjects together with their vital signs can be monitored.
[25]	FMCW	5.72-5.88 GHz	RR	Precisely localize metal plate up to 3.5 m; effect of clutters to extracted respiration signal is studied.
[127], [28]	SFCW	6-7 GHz	fall detection	It demonstrates target localization and a success rate of 94.3% in fall detection.
[35]	SFCW	3.14-3.46 GHz	HR/RR	When subject is at 1.2 m, HR error < 1.2%; when subject is at 0.6 m in orientation, HR error < 5.7%.
[29]	SFCW	0.3-1.3 GHz	RR	When subject lying on ground with orientations, RR can be detected through bricks 1.2 m away.
[30]	SFCW	2-4 GHz	localization	Corner reflector is accurately detected using only 20% of the total frequency points.

extraction of HR and RR at similar conditions to simplify the comparison. Results from the experiments of the SFCW radar system, indicated that the detection of HR was within an error rate of 2% irrespective of the subject's four described orientations up to 2 m. The experimental results also show that SFCW radar has demonstrated slightly better accuracy in the extraction of HR in front and back positions. Conversely, IPPG technique is uniquely capable of remotely detecting oxygen saturation levels and has similar performance to radar for HR and RR under ambient light conditions. However, it is not effective for remote triage or through-wall detection, and it significantly degrades or even fails under poor lighting conditions.

CHAPTER SEVEN

CONCLUSION AND FUTURE WORK

This research demonstrates the mathematical model, hardware implementation, and advanced signal processing algorithms of wideband Doppler radar systems in vital signs detection. This work primary focuses on two radar types, UWB pulse radar and SFCW radar.

7.1 Accomplishments and Contributions

Initially, UWB impulse radar was used. To overcome the difficulties in heart rate monitoring using UWB impulse radar, phase-based methods have been proposed to extract the phases of pulses modulated by heartbeat signals. With the phase information extracted from pulses, both heart rate and heart motion amplitude can be accurately estimated. UWB pulse radar has been successfully extended for more-than-one subject heart rates detection. The results have been validated with contact wired sensor. Advanced signal processing algorithm, specifically state space method, has been proposed to enhance the SNR of heart rate detection using the impulse UWB radar. Moreover, pulse radar has been extended to the micro-Doppler information extraction using state space method to enable the use of the micro-Doppler trajectories to distinguish different body joints of a walking human subject.

Alternatively, SFCW radar has been built utilizing direct digital synthesizer (DDS) and phase-lock loop (PLL), which covers a bandwidth from 2 GHz to 4 GHz. To make the radar system portable, compact SFCW radar composed of different layers of stacked boards using chip components has been designed as well. In-lab, experiments have been conducted to demonstrate the satisfactory performance of the SFCW radar system. Moreover, compressive sensing (CS) has been utilized to randomly step through the wide bandwidth and significantly reducing the number of measurements to speed up the data acquisition process. When compression rate is around 20%, SFCW radar still can precisely localize close-range objects. SFCW radar has been successfully utilized to detect respiratory and heart rates of stationary subjects in a close range.

Currently, radar systems are capable of respiration and heart rates monitoring, while it is still very challenging for radar systems to detect blood oxygen level. iPPG has been successfully used by researchers to identify SpO_2 of human subjects. In this work, iPPG sensor has been investigated for the HR and RR detection as well as for oxygen level monitoring. The performances of SFCW radar and iPPG system in cardiorespiratory rates detection have been compared experimentally. The accuracy of iPPG in vital signs detection is subject to the

illumination level of environment. Generally, SFCW radar and iPPG has demonstrated comparable performance in respiratory and heart rates monitoring in close distance and with good illumination.

7.2 Publications

Journal Papers

- [1] **L. Ren**, L. Kong, F. Foroughian, H. Wang, P. Theilmann, and A.E. Fathy, "Comparison study of non-contact vital signs detection using a Doppler stepped-frequency continuous wave radar and camera-based imaging photoplethysmography," IEEE Trans. Microw. Theory Techn., 2017. (In print)
- [2] **L. Ren**, H. Wang, K. Naishadham, O. Kilic, and A.E. Fathy, "Phase-based methods for heart rate detection using UWB impulse Doppler radar," IEEE Trans. Microw. Theory Techn., vol. 64, no. 10, pp. 3319-3331, Aug. 2016.
- [3] H. Wang, V. Dang, **L. Ren**, Q. Liu, L. Ren, E. Mao, O. Kilik, and A.E. Fathy, "An elegant solution: an alternative ultra-wideband transceiver based on stepped-frequency continuous-wave operation and compressive sensing," IEEE Microw. Mag., vol. 17, no. 7, pp. 53-63, June 2016.
- [4] K. Naishadham, J.E. Piou, **L. Ren**, and A.E. Fathy, "Estimation of cardiopulmonary parameters from ultra wideband radar measurements using the state space method," IEEE Trans. Biomed. Circuits Syst., vol. 10, no. 6, pp. 1037 - 1046, Apr. 2016.
- [5] **L. Ren**, Y.S. Koo, H. Wang, Y. Wang, Q. Liu, and A.E. Fathy, "Noncontact multiple heartbeats detection and subject localization using UWB impulse Doppler radar," IEEE Microw. Wireless Compon. Lett., vol. 25, no. 10, pp. 690-692, Aug. 2015.

Conference Papers

IEEE MTT-S International Microwave Symposium (IMS)

- [1] F. Quaiyum, **L. Ren**, S. Nahar, F. Foroughian, and A.E. Fathy, "Development of a reconfigurable low cost multi-mode radar system for contactless vital signs detection," IEEE MTT-S International Microwave Symposium Digest (IMS), Honolulu, Hawaii, USA, June 4-9, 2017.
- [2] H. Wang, **L. Ren**, O. Kilic, and A.E. Fathy, "Fast and precise ranging based on Stepped-Frequency continuous wave radar measurements using compressive sensing algorithms," IEEE MTT-S International Microwave Symposium Digest (IMS), San Francisco, California, May 22-27, USA, 2016.
- [3] **L. Ren**, H. Wang, K. Naishadham, Q. Liu, and A.E. Fathy, "Non-invasive detection of cardiac and respiratory rates from stepped frequency continuous wave radar measurements using the state space method," IEEE MTT-S

International Microwave Symposium Digest (IMS), Phoenix, Arizona, USA, May 17-22, 2015.

[4] **L. Ren**, H. Wang, K. Naishadham, Q. Liu, and A.E. Fathy, "Non-invasive detection of cardiac and respiratory rates from stepped frequency continuous wave radar measurements using the state space method," IEEE MTT-S International Microwave Symposium Digest (IMS), Phoenix, Arizona, USA, May 17-22, 2015.

IEEE Radio and Wireless Symposium (RWS)

[1] S. Nahar, **L. Ren**, N. Tran, O. Kilic and A.E. Fathy, "Through-wall detection of human breathing rate using compressive sensing technique," IEEE Radio and Wireless Symposium (RWS), Phoenix, Arizona, USA, January 15-17, 2017.

[2] H. Wang, **L. Ren**, E. Mao, and A.E. Fathy, "Phase based motion characteristics measurement for fall detection by using stepped-frequency continuous wave radar," IEEE Topical Conference on Biomedical Wireless Technologies, Networks, and Sensing Systems (BioWireleSS), Austin, Texas, USA, January 24-27, 2016.

[3] **L. Ren**, N. Tran, H. Wang, A.E. Fathy and O. Kilic, "Analysis of micro-Doppler signatures for vital sign detection using UWB impulse Doppler radar," IEEE Topical Conference on Biomedical Wireless Technologies, Networks, and Sensing Systems (BioWireleSS), Austin, Texas, USA, January 24-27, 2016.

[4] R.A. Fathy, H. Wang, and **L. Ren**, "Comparison of UWB Doppler radar and camera based photoplethysmography in non-contact multiple heartbeats detection," IEEE Topical Conference on Biomedical Wireless Technologies, Networks, and Sensing Systems (BioWireleSS), Austin, Texas, USA, January 24-27, 2016.

[5] **L. Ren**, Y.S. Koo, Y. Wang, and A.E. Fathy, "Noncontact heartbeat detection using UWB impulse Doppler radar," IEEE Topical Conference on Biomedical Wireless Technologies, Networks, and Sensing Systems (BioWireleSS), San Diego, California, USA, January 25-28, 2015.

[6] **L. Ren**, Y.S. Koo, Y. Wang, G. To, M. Mahfouz, and A.E. Fathy, "High-amplitude motion cancellation method for handheld UWB Doppler radar," IEEE Topical Conference on Biomedical Wireless Technologies, Networks, and Sensing Systems (BioWireleSS), Newport Beach, California, USA, January 19-22, 2014.

IEEE International Symposium on Antennas and Propagation (APS)

[7] A.E. Fathy, **L. Ren**, S. Nahar and O. Kilic, "Overview of human vital signs detection using radar techniques," IEEE International Symposium on Antennas and Propagation (APSURSI), San Diego, California, USA, July 9-14, 2017. (Invited)

- [8] N. Tran, S. Nahar, **L. Ren**, H. Wang, O. Kilic, and A.E. Fathy, "Contactless monitoring and classification of human motion activities by using SFCW radar," IEEE International Symposium on Antennas and Propagation (APSURSI), Fajardo, Puerto Rico, June 26 – July 1, 2016.
- [9] **L. Ren**, T. Phan, S. Nahar, N. Tran, O. Kilic, and A.E. Fathy, "Investigation of Vital Signs Monitoring Errors Due to Subject's Orientation, Clothing and Distance from a SFCW Radar," IEEE International Symposium on Antennas and Propagation (APSURSI), Fajardo, Puerto Rico, June 26 – July 1, 2016.
- [10] **L. Ren**, N. Tran, O. Kilic, and A.E. Fathy, "Short time state space method for human motion identification," IEEE International Symposium on Antennas and Propagation (APSURSI), Vancouver, British Columbia, Canada, July 19-24, 2015.
- [11] **L. Ren**, M.S. Hasan, R.A. Fathy, S. Islam, and A.E. Fathy, "UWB baby and sleep apnea monitor," IEEE International Symposium on Antennas and Propagation (APSURSI), Vancouver, British Columbia, Canada, July 19-24, 2015.
- [12] H. Wang, V. Dang, **L. Ren**, A.E. Fathy, E. Mao, and O. Kilic, "Towards Smarter Faster UWB Transceivers," IEEE International Symposium on Antennas and Propagation (APSURSI), Vancouver, British Columbia, Canada, July 19-24, 2015.

USNC-URSI National Radio Science Meeting (URSI)

- [13] **L. Ren**, S. Nahar, and A.E. Fathy, "Development of a low cost compact integrated step frequency continuous wave radar for non-contact vital sign detection," National Radio Science Meeting (USNC-URSI), Boulder, Colorado, USA, January 4-7, 2017.
- [14] S. Nahar, **L. Ren**, T. Phan, O. Kilic and A.E. Fathy, "Human respiration rate estimation using SFCW radar system," United States National Committee of URSI National Radio Science Meeting (USNC-URSI NRSM), Boulder, Colorado, USA, January 4-7, 2017.
- [15] **L. Ren**, S. Boualleg, and A.E. Fathy, "Enhanced vital signs detection using MIMO UWB radar system by coherently accumulating multiple channel data," USNC-URSI Radio Science Meeting (Joint with AP-S Symposium), Fajardo, Puerto Rico, June 26 – July 1, 2016.
- [16] **L. Ren**, H. Wang, V. Dang, O. Kilic, and A.E. Fathy, "Stepped-frequency continuous wave radar based on compressive sensing," United States National Committee of URSI National Radio Science Meeting (USNC-URSI NRSM), Boulder, Colorado, USA, January 6-9, 2016.
- [17] H. Wang, **L. Ren**, K. Naishadham, and A.E. Fathy, "Cardiac rate estimation using continuous wave radar and ultra wideband radar at different distances," United States National Committee of URSI National Radio Science Meeting (USNC-URSI NRSM), Boulder, Colorado, USA, January 6-9, 2016.

[18] **L. Ren**, and A.E. Fathy, "Noncontact heartbeat detection using UWB impulse Doppler radar," USNC-URSI Radio Science Meeting (Joint with AP-S Symposium), Vancouver, British Columbia, Canada, July 19-24, 2015.

Other Conferences

[19] **L. Ren**, A.E. Fathy, K. Naishadham, J.E. Piou, V. Dang, and O. Kilic, "Overview of vital sign detection-simulation and measurements," IEEE/ACES International Conference on Wireless Information Technology and Systems (ICWITS) and Applied Computational Electromagnetics (ACES), Honolulu, Hawaii, March 13-17, 2016.

7.3 Conclusion

This work mainly focuses on the vital signs monitoring of human subjects using UWB pulse radar and SFCW radar. The topics of human micro-Doppler signatures extraction using UWB radar and iPPG techniques for vital signs detection are covered as well. This dissertation can be concluded as below.

(1) Compared with UWB pulse radar using free-running LO, the UWB radar with system synchronization and phased-locked transmitting signal possesses lower system phase noise and provides higher accuracy in vital signs detection.

(2) UWB pulse radar has been extended for human heart rate detection. Due to the small amplitude of heartbeat, the conventional amplitude-based signal processing suffers from harmonics of respiration and intermodulation interferences in heart rate monitoring. Phase-based methods overcome these aforementioned drawbacks and provide accurate estimation of both heartbeat amplitude in time domain and heart rate in spectrum.

(3) UWB impulse radar can localize multiple subjects and detect the heart rates. Advanced signal processing such as SSM will further improve the SNR in the heart rate detection using UWB pulse radar.

(4) STSSM has been developed to identify the m-D signatures of different human body joints. Boulic model serves as reference to the extracted m-D trajectories with STSSM using UWB pulse radar.

(5) Compact integrated SFCW radar using chips instead of connectorized components were designed and fabricated. Its performance in human vital signs detection is comparable with connectorized counterpart and heart rate detection error is <2% for 0.6m radar-subject distance.

(6) Time domain (impulse) UWB radar: equivalent time sampling is used to circumvent the need for fast and expensive ADCs. Frequency domain (SFCW) UWB radar: several channels work simultaneously to reduce the data acquisition time. CS based SFCW signal processing: uses measurements at only a small number of random frequencies to further reduce the data acquisition time with adequate errors.

(7) The performance of SFCW radar and iPPG sensor in vital signs detection has been experimentally compared. Both techniques showed comparable accuracy in the respiratory and heart rates extraction under ambient light conditions, while iPPG sensor has the unique capability of non-contact oxygen saturation level detection. However, iPPG sensor cannot be utilized for through-wall detection, and its performance deteriorates under poor lighting conditions.

7.4 Direction of Future Work

By now, equivalent time sampling scheme is still being used to collect reflected narrow pulses in impulse radar. The next step of research is to implement direct sampling instead using ultra-high-speed ADC like the ones currently developed by TI. The distortion of the reconstructed pulses introduced by the equivalent time sampling will be eliminated when using the direct sampling method.

Both phase-based methods and SSM have been proposed for the signal processing of collected radar data. A clear guideline of which method to be used will be developed for different scenarios of vital signs detection. SSM needs to be implemented for real time monitoring with LabVIEW.

In the future work, the SFCW radar will be fully integrated with CMOS or GaAs technology so the system size will be greatly reduced. A hybrid system consisting of SFCW radar and iPPG sensor with different working mode will be thoroughly studied as well. The hybrid system can monitor respiratory, heart rates and SpO_2 level of human.

BIBLIOGRAPHY

- [1] J. H. Shin, Y. J. Chee, D.-U. Jeong, and K. S. Park, "Nonconstrained sleep monitoring system and algorithms using air-mattress with balancing tube method," *IEEE transactions on information technology in biomedicine*, vol. 14, no. 1, pp. 147-156, 2010.
- [2] L. Scalise, *Non contact heart monitoring*: INTECH Open Access Publisher, 2012.
- [3] C. Li, V. M. Lubecke, O. Boric-Lubecke, and J. Lin, "A review on recent advances in Doppler radar sensors for noncontact healthcare monitoring," *IEEE Trans. Microw. Theory Techn.*, vol. 61, no. 5, pp. 2046-2060, 2013.
- [4] G. Wang, C. Gu, T. Inoue, and C. Li, "A hybrid FMCW-interferometry radar for indoor precise positioning and versatile life activity monitoring," *IEEE Transactions on Microwave Theory and Techniques*, vol. 62, no. 11, pp. 2812-2822, 2014.
- [5] M. Mercuri, P. J. Soh, L. Boccia, D. Schreurs, G. A. Vandenbosch, P. Leroux, and G. Amendola, "Optimized SFCW radar sensor aiming at fall detection in a real room environment," in *IEEE Biomedical Wireless Technologies, Networks, and Sensing Systems (BioWireleSS)*, Austin, TX, USA, 2013, pp. 4-6.
- [6] S. Wang, A. Pohl, T. Jaeschke, M. Czaplik, M. Köny, S. Leonhardt, and N. Pohl, "A novel ultra-wideband 80 GHz FMCW radar system for contactless monitoring of vital signs," in *IEEE Engineering in Medicine and Biology Society (EMBC)*, Milan, Italy, 2015, pp. 4978-4981.
- [7] J. Tu, T. Hwang, and J. Lin, "Respiration rate measurement under 1-D body motion using single continuous-wave Doppler radar vital sign detection system," *IEEE Trans. Microw. Theory Techn.*, vol. 64, no. 6, pp. 1937-1946, 2016.
- [8] H.-C. Kuo, C.-C. Lin, C.-H. Yu, P.-H. Lo, J.-Y. Lyu, C.-C. Chou, and H.-R. Chuang, "A fully integrated 60-GHz CMOS direct-conversion Doppler radar RF sensor with clutter canceller for single-antenna noncontact human vital-signs detection," *IEEE Trans. Microw. Theory Techn.*, vol. 64, no. 4, pp. 1018-1028, 2016.
- [9] M.-C. Huang, J. J. Liu, W. Xu, C. Gu, C. Li, and M. Sarrafzadeh, "A self-calibrating radar sensor system for measuring vital signs," *IEEE Transactions on Biomedical Circuits and Systems*, vol. 10, no. 2, pp. 352-363, 2016.
- [10] L. Chioukh, H. Boutayeb, D. Deslandes, and K. Wu, "Noise and sensitivity of harmonic radar architecture for remote sensing and detection of vital signs," *IEEE Trans. Microw. Theory Techn.*, vol. 62, no. 9, pp. 1847-1855, 2014.
- [11] P.-H. Wu, J.-K. Jau, C.-J. Li, T.-S. Horng, and P. Hsu, "Phase-and self-injection-locked radar for detecting vital signs with efficient elimination of DC offsets and null points," *IEEE Trans. Microw. Theory Techn.*, vol. 61, no. 1, pp. 685-695, 2013.

- [12] T.-Y. J. Kao, Y. Yan, T.-M. Shen, A. Y.-K. Chen, and J. Lin, "Design and analysis of a 60-GHz CMOS Doppler micro-radar system-in-package for vital-sign and vibration detection," *IEEE Trans. Microw. Theory Techn.*, vol. 61, no. 4, pp. 1649-1659, 2013.
- [13] G. Vinci, S. Lindner, F. Barbon, S. Mann, M. Hofmann, A. Duda, R. Weigel, and A. Koelpin, "Six-port radar sensor for remote respiration rate and heartbeat vital-sign monitoring," *IEEE Trans. Microw. Theory Techn.*, vol. 61, no. 5, pp. 2093-2100, 2013.
- [14] F.-K. Wang, T.-S. Horng, K.-C. Peng, J.-K. Jau, J.-Y. Li, and C.-C. Chen, "Single-antenna Doppler radars using self and mutual injection locking for vital sign detection with random body movement cancellation," *IEEE Trans. Microw. Theory Techn.*, vol. 59, no. 12, pp. 3577-3587, 2011.
- [15] C. Gu, R. Li, H. Zhang, A. Y. Fung, C. Torres, S. B. Jiang, and C. Li, "Accurate respiration measurement using DC-coupled continuous-wave radar sensor for motion-adaptive cancer radiotherapy," *IEEE Transactions on Biomedical Engineering*, vol. 59, no. 11, pp. 3117-3123, 2012.
- [16] M. Baboli, A. Singh, N. Hafner, and V. Lubecke, "Parametric study of antennas for long range Doppler radar heart rate detection," in *IEEE Annual International Conference of Engineering in Medicine and Biology Society (EMBC)*, 2012, pp. 3764-3767.
- [17] B.-K. Park, O. Boric-Lubecke, and V. M. Lubecke, "Arctangent demodulation with DC offset compensation in quadrature Doppler radar receiver systems," *IEEE Trans. Microw. Theory Techn.*, vol. 55, no. 5, pp. 1073-1079, 2007.
- [18] C. Li and J. Lin, "Random body movement cancellation in Doppler radar vital sign detection," *IEEE Trans. Microw. Theory Techn.*, vol. 56, no. 12, pp. 3143-3152, 2008.
- [19] P. Bernardi, R. Cicchetti, S. Pisa, E. Pittella, E. Piuze, and O. Testa, "Design, realization, and test of a UWB radar sensor for breath activity monitoring," *IEEE Sensors Journal*, vol. 14, no. 2, pp. 584-596, 2014.
- [20] J. C. Y. Lai, Y. Xu, E. Gunawan, E. C.-P. Chua, A. Maskooki, Y. L. Guan, K.-S. Low, C. B. Soh, and C.-L. Poh, "Wireless sensing of human respiratory parameters by low-power ultrawideband impulse radio radar," *IEEE Transactions on Instrumentation and Measurement*, vol. 60, no. 3, pp. 928-938, 2011.
- [21] X. Wang, A. Dinh, and D. Teng, "3-10 GHz ultra wideband front-end transceiver in 0.13 μm complementary metal oxide semiconductor for low-power biomedical radar," *IET Circuits, Devices & Systems*, vol. 8, no. 4, pp. 272-279, 2014.
- [22] K. K.-M. Chan, A. E.-C. Tan, and K. Rambabu, "Circularly polarized ultra-wideband radar system for vital signs monitoring," *IEEE Transactions on microwave theory and techniques*, vol. 61, no. 5, pp. 2069-2075, 2013.

- [23] B. Schleicher, I. Nasr, A. Trasser, and H. Schumacher, "IR-UWB radar demonstrator for ultra-fine movement detection and vital-sign monitoring," *IEEE Trans. Microw. Theory Techn.*, vol. 61, no. 5, pp. 2076-2085, 2013.
- [24] D. Zito, D. Pepe, M. Mincica, F. Zito, A. Tognetti, A. Lanatà, and D. De Rossi, "SoC CMOS UWB pulse radar sensor for contactless respiratory rate monitoring," *IEEE Transactions on Biomedical Circuits and Systems*, vol. 5, no. 6, pp. 503-510, 2011.
- [25] G. Wang, J.-M. Munoz-Ferreras, C. Gu, C. Li, and R. Gomez-Garcia, "Application of linear-frequency-modulated continuous-wave (LFMCW) radars for tracking of vital signs," *IEEE Transactions on Microwave Theory and Techniques*, vol. 62, no. 6, pp. 1387-1399, 2014.
- [26] M. Lees, "Digital beamforming calibration for FMCW radar," *IEEE Trans. Aerosp. Electron. Syst.*, vol. 25, no. 2, pp. 281-284, 1989.
- [27] J. Fuchs, K. D. Ward, M. P. Tulin, and R. A. York, "Simple techniques to correct for VCO nonlinearities in short range FMCW radars," in *IEEE International Microwave Symposium (IMS)*, 1996, pp. 1175-1178.
- [28] M. Mercuri, P. J. Soh, G. Pandey, P. Karsmakers, G. A. Vandenbosch, P. Leroux, and D. Schreurs, "Analysis of an indoor biomedical radar-based system for health monitoring," *IEEE Trans. Microw. Theory Techn.*, vol. 61, no. 5, pp. 2061-2068, 2013.
- [29] L. Liu and S. Liu, "Remote detection of human vital sign with stepped-frequency continuous wave radar," *IEEE J. Sel. Topics Appl. Earth Observ. in Remote Sens.*, vol. 7, no. 3, pp. 775-782, 2014.
- [30] H. Wang, V. Dang, L. Ren, Q. Liu, L. Ren, E. Mao, O. Kilik, and A. E. Fathy, "An elegant solution: an alternative ultra-wideband transceiver based on stepped-frequency continuous-wave operation and compressive sensing," *IEEE Microwave Magazine*, vol. 17, no. 7, pp. 53-63, 2016.
- [31] C. Gu, G. Wang, Y. Li, T. Inoue, and C. Li, "A hybrid radar-camera sensing system with phase compensation for random body movement cancellation in Doppler vital sign detection," *IEEE Trans. Microw. Theory Techn.*, vol. 61, no. 12, pp. 4678-4688, 2013.
- [32] H.-R. Chuang, H.-C. Kuo, F.-L. Lin, T.-H. Huang, C.-S. Kuo, and Y.-W. Ou, "60-GHz millimeter-wave life detection system (MLDS) for noncontact human vital-signal monitoring," *IEEE Sensors J.*, vol. 12, no. 3, pp. 602-609, 2012.
- [33] Y. Wang, Q. Liu, and A. E. Fathy, "CW and pulse-Doppler radar processing based on FPGA for human sensing applications," *IEEE Trans. Geosci. Remote Sens.*, vol. 51, no. 5, pp. 3097-3107, 2013.
- [34] A. Lazaro, D. Girbau, and R. Villarino, "Analysis of vital signs monitoring using an IR-UWB radar," *Progress In Electromagnetics Research*, vol. 100, pp. 265-284, 2010.
- [35] L. Ren, H. Wang, K. Naishadham, Q. Liu, and A. E. Fathy, "Non-invasive detection of cardiac and respiratory rates from stepped frequency continuous wave radar measurements using the state space method," in

- IEEE MTT-S International Microwave Symposium (IMS)*, Phoenix, AZ, USA, 2015, pp. 1-4.
- [36] M. Baboli, S. A. Ghorashi, N. Saniei, and A. Ahmadian, "A new wavelet based algorithm for estimating respiratory motion rate using UWB radar," in *International Conference on Biomedical and Pharmaceutical Engineering (ICBPE)*, Biopolis, Singapore, 2009, pp. 1-3.
 - [37] M. Mercuri, P. J. Soh, G. Pandey, P. Karsmakers, G. A. Vandenbosch, P. Leroux, and D. Schreurs, "Analysis of an indoor biomedical radar-based system for health monitoring," *IEEE Transactions on Microwave Theory and Techniques*, vol. 61, no. 5, pp. 2061-2068, 2013.
 - [38] Y. Wang, Q. Liu, and A. E. Fathy, "Simultaneous localization and respiration detection of multiple people using low cost UWB biometric pulse Doppler radar sensor," in *IEEE MTT-S International Microwave Symposium (IMS)*, Montréal, Canada, 2012, pp. 1-3.
 - [39] Y. S. Koo, L. Ren, Y. Wang, and A. E. Fathy, "UWB MicroDoppler Radar for human Gait analysis, tracking more than one person, and vital sign detection of moving persons," in *IEEE MTT-S International Microwave Symposium (IMS)*, Seattle, WA, USA, 2013, pp. 1-4.
 - [40] I. Hilger, C. Geyer, F. Thiel, F. S. di Clemente, F. Seifert, G. Rimkus, J. Sachs, K. Dahlke, M. Helbig, and M. Hein, *UltraMEDIS-Ultra-Wideband Sensing in Medicine*: INTECH Open Access Publisher, 2013.
 - [41] Y. Nijsure, W. P. Tay, E. Gunawan, F. Wen, Z. Yang, Y. L. Guan, and A. P. Chua, "An impulse radio ultrawideband system for contactless noninvasive respiratory monitoring," *IEEE Transactions on Biomedical Engineering*, vol. 60, no. 6, pp. 1509-1517, 2013.
 - [42] J. Li, L. Liu, Z. Zeng, and F. Liu, "Advanced signal processing for vital sign extraction with applications in UWB radar detection of trapped victims in complex environments," *IEEE Journal of Selected Topics in Applied Earth Observations and Remote Sensing*, vol. 7, no. 3, pp. 783-791, 2014.
 - [43] Z. Li, W. Li, H. Lv, Y. Zhang, X. Jing, and J. Wang, "A novel method for respiration-like clutter cancellation in life detection by dual-frequency IR-UWB radar," *IEEE Transactions on Microwave Theory and Techniques*, vol. 61, no. 5, pp. 2086-2092, 2013.
 - [44] A. Nezirovic, A. G. Yarovoy, and L. P. Ligthart, "Signal processing for improved detection of trapped victims using UWB radar," *IEEE Transactions on Geoscience and Remote Sensing*, vol. 48, no. 4, pp. 2005-2014, 2010.
 - [45] Y. Xu, S. Dai, S. Wu, J. Chen, and G. Fang, "Vital sign detection method based on multiple higher order cumulant for ultrawideband radar," *IEEE Transactions on Geoscience and Remote Sensing*, vol. 50, no. 4, pp. 1254-1265, 2012.
 - [46] W. Hu, Z. Zhao, Y. Wang, H. Zhang, and F. Lin, "Noncontact accurate measurement of cardiopulmonary activity using a compact quadrature

- Doppler radar sensor," *IEEE Transactions on Biomedical Engineering*, vol. 61, no. 3, pp. 725-735, 2014.
- [47] H. Wang, L. Ren, E. Mao, and A. E. Fathy, "Phase based motion characteristics measurement for fall detection by using stepped-frequency continuous wave radar," in *IEEE Biomedical Wireless Technologies, Networks, and Sensing Systems (BioWireleSS)*, Austin, TX, USA, 2016, pp. 43-45.
 - [48] L. Ren, Y. S. Koo, Y. Wang, and A. E. Fathy, "Noncontact heartbeat detection using UWB impulse doppler radar," in *IEEE Topical Conference on Biomedical Wireless Technologies, Networks, and Sensing Systems (BioWireleSS)*, 2015, pp. 1-3.
 - [49] L. Ren, Y. S. Koo, H. Wang, Y. Wang, Q. Liu, and A. E. Fathy, "Noncontact multiple heartbeats detection and subject localization using UWB impulse Doppler radar," *IEEE Microw. Compon. Lett.*, vol. 25, no. 10, pp. 690-692, 2015.
 - [50] J. Piou, "A state identification method for 1-D measurements with gaps," in *Proc. American Institute of Aeronautics and Astronautics Guidance Navigation and Control Conf.*, San Francisco, CA, USA, 2005, pp. 1-11.
 - [51] K. Naishadham and J. E. Piou, "A robust state space model for the characterization of extended returns in radar target signatures," *IEEE Transactions on Antennas and Propagation*, vol. 56, no. 6, pp. 1742-1751, 2008.
 - [52] L. Ren, A. E. Fathy, K. Naishadham, J. E. Piou, V. Dang, and O. Kilic, "Overview of vital sign detection-simulation and measurements," in *IEEE/ACES International Conference on Wireless Information Technology and Systems (ICWITS) and Applied Computational Electromagnetics (ACES)*, Honolulu, Hawaii, USA, 2016, pp. 1-2.
 - [53] K. Naishadham, J. E. Piou, L. Ren, and A. E. Fathy, "Estimation of Cardiopulmonary Parameters From Ultra Wideband Radar Measurements Using the State Space Method," *IEEE Transactions on Biomedical Circuits and Systems*, vol. PP, no. 99, pp. 1-10, 2016.
 - [54] L. Ren, H. Wang, A. E. Fathy, N. Tran, and O. Kilic, "Short time state space method for human motion identification," in *IEEE International Symposium on Antennas and Propagation & USNC/URSI National Radio Science Meeting*, Vancouver, BC, Canada, 2015, pp. 510-511.
 - [55] Q. Liu, Y. Wang, and A. E. Fathy, "Towards low cost, high speed data sampling module for multifunctional real-time UWB radar," *IEEE Transactions on Aerospace and Electronic Systems*, vol. 49, no. 2, pp. 1301-1316, 2013.
 - [56] Y. Wang and A. E. Fathy, "UWB micro-doppler radar for human gait analysis using joint range-time-frequency representation," in *SPIE Defense, Security, and Sensing*, 2013, pp. 873404-873404-9.
 - [57] J. Wang, X. Wang, L. Chen, J. Huangfu, C. Li, and L. Ran, "Noncontact distance and amplitude-independent vibration measurement based on an

- extended DACM algorithm," *IEEE Transactions on Instrumentation and Measurement*, vol. 63, no. 1, pp. 145-153, 2014.
- [58] A. Singh, X. Gao, E. Yavari, M. Zakrzewski, X. H. Cao, V. M. Lubecke, and O. Boric-Lubecke, "Data-based quadrature imbalance compensation for a CW Doppler radar system," *IEEE Transactions on Microwave Theory and Techniques*, vol. 61, no. 4, pp. 1718-1724, 2013.
 - [59] L. Ren, M. S. Hasan, S. K. Islam, A. E. Fathy, and R. A. Fathy, "UWB baby and sleep apnea monitor," in *IEEE International Symposium on Antennas and Propagation & USNC/URSI National Radio Science Meeting*, Vancouver, BC, Canada, 2015, pp. 721-722.
 - [60] R. Boulic, N. M. Thalmann, and D. Thalmann, "A global human walking model with real-time kinematic personification," *The visual computer*, vol. 6, no. 6, pp. 344-358, 1990.
 - [61] V. C. Chen, "Detection and analysis of human motion by radar," in *IEEE Radar Conference*, Rome, Italy, 2008.
 - [62] A. Lin and H. Ling, "Doppler and direction-of-arrival (DDOA) radar for multiple-mover sensing," *IEEE transactions on aerospace and electronic systems*, vol. 43, no. 4, 2007.
 - [63] M. Otero, "Application of a continuous wave radar for human gait recognition," in *Proc. SPIE*, 2005, pp. 538-548.
 - [64] B. G. Mobasser and M. G. Amin, "A time-frequency classifier for human gait recognition," in *Proc. SPIE*, 2009, p. 730628.
 - [65] A. R. Hunt, "Use of a frequency-hopping radar for imaging and motion detection through walls," *IEEE Transactions on Geoscience and Remote Sensing*, vol. 47, no. 5, pp. 1402-1408, 2009.
 - [66] J. Sachs, M. Aftanas, S. Crabbe, M. Drutarovsky, R. Klukas, D. Kocur, T.-T. Nguyen, P. Peyerl, J. Rovnakova, and E. Zaikov, "Detection and tracking of moving or trapped people hidden by obstacles using ultra-wideband pseudo-noise radar," in *Radar Conference, 2008. EuRAD 2008. European*, 2008, pp. 408-411.
 - [67] D. Tahmoush and J. Silvius, "Radar micro-doppler for long range front-view gait recognition," in *Biometrics: Theory, Applications, and Systems, 2009. BTAS'09. IEEE 3rd International Conference on*, 2009, pp. 1-6.
 - [68] V. C. Chen, F. Li, S.-S. Ho, and H. Wechsler, "Micro-Doppler effect in radar: phenomenon, model, and simulation study," *IEEE Transactions on Aerospace and electronic systems*, vol. 42, no. 1, pp. 2-21, 2006.
 - [69] A. Ghaleb, L. Vignaud, and J. Nicolas, "Micro-Doppler analysis of wheels and pedestrians in ISAR imaging," *IET Signal Processing*, vol. 2, no. 3, pp. 301-311, 2008.
 - [70] V. C. Chen, F. Li, S.-S. Ho, and H. Wechsler, "Analysis of micro-Doppler signatures," *IEE Proceedings-Radar, Sonar and Navigation*, vol. 150, no. 4, pp. 271-276, 2003.

- [71] L. Stankovic, T. Thayaparan, M. Dakovic, and V. Popovic-Bugarin, "Micro-Doppler removal in the radar imaging analysis," *IEEE Transactions on Aerospace and Electronic Systems*, vol. 49, no. 2, pp. 1234-1250, 2013.
- [72] J. Niu, Y. Liu, W. Jiang, X. Li, and G. Kuang, "Weighted average frequency algorithm for Hilbert–Huang spectrum and its application to micro-Doppler estimation," *IET Radar, Sonar & Navigation*, vol. 6, no. 7, pp. 595-602, 2012.
- [73] S. Ram and H. Ling, "Analysis of microDopplers from human gait using reassigned joint time-frequency transform," *Electronics Letters*, vol. 43, no. 23, 2007.
- [74] T. Thayaparan, S. Abrol, E. Riseborough, L. Stankovic, D. Lamothe, and G. Duff, "Analysis of radar micro-Doppler signatures from experimental helicopter and human data," *IET Radar, Sonar & Navigation*, vol. 1, no. 4, pp. 289-299, 2007.
- [75] A. Balleri, K. Chetty, and K. Woodbridge, "Classification of personnel targets by acoustic micro-Doppler signatures," *IET radar, sonar & navigation*, vol. 5, no. 9, pp. 943-951, 2011.
- [76] Y. Kim and H. Ling, "Through-wall human tracking with multiple Doppler sensors using an artificial neural network," *IEEE Transactions on Antennas and Propagation*, vol. 57, no. 7, pp. 2116-2122, 2009.
- [77] Y. Kim and H. Ling, "Human activity classification based on micro-Doppler signatures using a support vector machine," *IEEE Transactions on Geoscience and Remote Sensing*, vol. 47, no. 5, pp. 1328-1337, 2009.
- [78] L. Du, Y. Ma, B. Wang, and H. Liu, "Noise-robust classification of ground moving targets based on time-frequency feature from micro-Doppler signature," *IEEE Sensors Journal*, vol. 14, no. 8, pp. 2672-2682, 2014.
- [79] L. Du, J. Li, P. Stoica, H. Ling, and S. S. Ram, "Doppler spectrogram analysis of human gait via iterative adaptive approach," *Electronics letters*, vol. 45, no. 3, pp. 186-188, 2009.
- [80] O. R. Fogle and B. D. Rigling, "Micro-range/micro-Doppler decomposition of human radar signatures," *IEEE Transactions on Aerospace and Electronic Systems*, vol. 48, no. 4, pp. 3058-3072, 2012.
- [81] D. P. Fairchild and R. M. Narayanan, "Classification of human motions using empirical mode decomposition of human micro-Doppler signatures," *IET Radar, Sonar & Navigation*, vol. 8, no. 5, pp. 425-434, 2014.
- [82] Y. Ding and J. Tang, "Micro-Doppler trajectory estimation of pedestrians using a continuous-wave radar," *IEEE Transactions on Geoscience and Remote Sensing*, vol. 52, no. 9, pp. 5807-5819, 2014.
- [83] J. Piou, "Gait extraction from short radar dwells collected on dismounts," in *American Control Conference (ACC), 2014*, 2014, pp. 4834-4839.
- [84] K. Naishadham and J. E. Piou, "A novel 1-D block processing approach to 2-D NMR spectroscopy," in *Biomedical Imaging: From Nano to Macro, 2007. ISBI 2007. 4th IEEE International Symposium on*, 2007, pp. 1352-1355.

- [85] J. M. Garcia-Rubia, O. Kilic, V. Dang, Q. M. Nguyen, and N. Tran, "Analysis of moving human micro-Doppler signature in forest environments," *Progress In Electromagnetics Research*, vol. 148, pp. 1-14, 2014.
- [86] S. S. Ram, C. Christianson, and H. Ling, "Simulation of high range-resolution profiles of humans behind walls," in *Radar Conference, 2009 IEEE*, 2009, pp. 1-4.
- [87] Q. M. Nguyen, V. Dang, O. Kilic, and E. El-Araby, "Parallelizing fast multipole method for large-scale electromagnetic problems using GPU clusters," *IEEE antennas and wireless propagation letters*, vol. 12, pp. 868-871, 2013.
- [88] C. L. Bennett and G. F. Ross, "Time-domain electromagnetics and its applications," *Proceedings of the IEEE*, vol. 66, no. 3, pp. 299-318, 1978.
- [89] F. C. Commission, "In the matter of revision of part 15 of the commission's rules regarding ultra-wideband transmission systems," *First Report And Order, ET Docket 98-153*, 2002.
- [90] E. M. Dominguez, R. Tigrek, M. Rugginao, G. Lellough, W. de Heij, D. Bockstal, and P. van Gendersen, "EXPERIMENTAL SET UP DEMONSTRATING COMBINED USE OF OFDM FOR RADAR AND COMMUNICATIONS," *Microwave Journal*, 2010.
- [91] J. D. Taylor, *Ultra-wideband radar technology*: CRC press, 2000.
- [92] E. Elkhoully, N. Rowe, A. E. Fathy, M. J. Kuhn, and M. R. Mahfouz, "Precise indoor localization systems: Alternative methods for sub-sampling UWB pulses and associated error sources," in *Biomedical Wireless Technologies, Networks, and Sensing Systems (BioWireleSS), 2013 IEEE Topical Conference on*, 2013, pp. 1-3.
- [93] A. G. Yarovoy, T. G. Savelyev, P. J. Aubry, P. E. Lys, and L. P. Ligthart, "UWB array-based sensor for near-field imaging," *IEEE Transactions on Microwave Theory and Techniques*, vol. 55, no. 6, pp. 1288-1295, 2007.
- [94] L. Chen and O. Shan, "A time-domain beamformer for UWB through-wall imaging," in *Proc. IEEE TENCON*, Taipei, 2007, pp. 1-4.
- [95] K. Kauffman, J. Raquet, Y. Morton, and D. Garmatyuk, "Real-time UWB-OFDM radar-based navigation in unknown terrain," *IEEE Transactions on Aerospace and Electronic Systems*, vol. 49, no. 3, pp. 1453-1466, 2013.
- [96] G. T. Ruck, "Ultra-wideband radar receiver," in *OE/LASE'92*, 1992, pp. 174-180.
- [97] C. Zhang, A. E. Fathy, and M. Mahfouz, "Performance enhancement of a sub-sampling circuit for ultra-wideband signal processing," *IEEE Microwave and wireless components letters*, vol. 17, no. 12, pp. 873-875, 2007.
- [98] Y. Yang and A. E. Fathy, "Development and implementation of a real-time see-through-wall radar system based on FPGA," *IEEE Transactions on Geoscience and Remote Sensing*, vol. 47, no. 5, pp. 1270-1280, 2009.

- [99] D. Yang, H. Li, Z. Zhang, and G. D. Peterson, "Compressive sensing based sub-mm accuracy UWB positioning systems: A space-time approach," *Digital Signal Processing*, vol. 23, no. 1, pp. 340-354, 2013.
- [100] E. J. Candès, J. Romberg, and T. Tao, "Robust uncertainty principles: Exact signal reconstruction from highly incomplete frequency information," *IEEE Transactions on information theory*, vol. 52, no. 2, pp. 489-509, 2006.
- [101] A. B. Suksmono, E. Bharata, A. A. Lestari, A. G. Yarovoy, and L. P. Ligthart, "Compressive stepped-frequency continuous-wave ground-penetrating radar," *IEEE geoscience and remote sensing letters*, vol. 7, no. 4, pp. 665-669, 2010.
- [102] P. Van Genderen, P. Hakkaart, J. Van Heijenoort, and G. Hermans, "A multi frequency radar for detecting landmines: design aspects and electrical performance," in *Microwave Conference, 2001. 31st European*, 2001, pp. 1-4.
- [103] V. F. Kroupa, V. Cizek, J. Stursa, and H. Svandova, "Spurious signals in direct digital frequency synthesizers due to the phase truncation," *IEEE transactions on ultrasonics, ferroelectrics, and frequency control*, vol. 47, no. 5, pp. 1166-1172, 2000.
- [104] H. Wang, H. Wang, L. Ren, and E. Mao, "Low spurious noise frequency synthesis based on a DDS-driven wideband PLL architecture," *Journal of Beijing Institute of Technology*, vol. 4, p. 014, 2013.
- [105] D. L. Donoho, "Compressed sensing," *IEEE Transactions on information theory*, vol. 52, no. 4, pp. 1289-1306, 2006.
- [106] E. J. Candès, J. K. Romberg, and T. Tao, "Stable signal recovery from incomplete and inaccurate measurements," *Communications on pure and applied mathematics*, vol. 59, no. 8, pp. 1207-1223, 2006.
- [107] J. A. Tropp and A. C. Gilbert, "Signal recovery from random measurements via orthogonal matching pursuit," *IEEE Transactions on information theory*, vol. 53, no. 12, pp. 4655-4666, 2007.
- [108] S. Sarvotham, D. Baron, M. Wakin, M. F. Duarte, and R. G. Baraniuk, "Distributed compressed sensing of jointly sparse signals," in *Asilomar conference on signals, systems, and computers*, 2005, pp. 1537-1541.
- [109] E. J. Candès and T. Tao, "Decoding by linear programming," *IEEE transactions on information theory*, vol. 51, no. 12, pp. 4203-4215, 2005.
- [110] M. Lustig, D. Donoho, and J. M. Pauly, "Sparse MRI: The application of compressed sensing for rapid MR imaging," *Magnetic resonance in medicine*, vol. 58, no. 6, pp. 1182-1195, 2007.
- [111] M. Lustig, D. L. Donoho, J. M. Santos, and J. M. Pauly, "Compressed sensing MRI," *IEEE Signal Processing Magazine*, vol. 25, no. 2, pp. 72-82, 2008.
- [112] R. Baraniuk and P. Steeghs, "Compressive radar imaging," in *2007 IEEE Radar Conference*, 2007, pp. 128-133.

- [113] M. Herman and T. Strohmer, "Compressed sensing radar," in *2008 IEEE Radar Conference*, 2008, pp. 1-6.
- [114] M. A. Herman and T. Strohmer, "High-resolution radar via compressed sensing," *IEEE transactions on signal processing*, vol. 57, no. 6, pp. 2275-2284, 2009.
- [115] M. Rossi, A. M. Haimovich, and Y. C. Eldar, "Spatial compressive sensing for MIMO radar," *IEEE Transactions on Signal Processing*, vol. 62, no. 2, pp. 419-430, 2014.
- [116] M. Rossi, A. M. Haimovich, and Y. C. Eldar, "Conditions for target recovery in spatial compressive sensing for MIMO radar," in *Acoustics, Speech and Signal Processing (ICASSP), 2013 IEEE International Conference on*, 2013, pp. 4115-4119.
- [117] G. Lellouch, R. Pribic, and P. van Genderen, "Merging frequency agile ofdm waveforms and compressive sensing into a novel radar concept," in *Radar Conference, 2009. EuRAD 2009. European*, 2009, pp. 137-140.
- [118] A. C. Gurbuz, J. H. McClellan, and W. R. Scott, "A compressive sensing data acquisition and imaging method for stepped frequency GPRs," *IEEE Transactions on Signal Processing*, vol. 57, no. 7, pp. 2640-2650, 2009.
- [119] Y.-S. Yoon and M. G. Amin, "Imaging of behind the wall targets using wideband beamforming with compressive sensing," in *2009 IEEE/SP 15th Workshop on Statistical Signal Processing*, 2009, pp. 93-96.
- [120] Q. Huang, L. Qu, B. Wu, and G. Fang, "UWB through-wall imaging based on compressive sensing," *IEEE Transactions on Geoscience and Remote Sensing*, vol. 48, no. 3, pp. 1408-1415, 2010.
- [121] V. Dang and O. Kilic, "Joint DoA-range-doppler tracking of moving targets based on compressive sensing," in *2014 IEEE Antennas and Propagation Society International Symposium (APSURSI)*, 2014, pp. 141-142.
- [122] J. Yuan, P. Tian, and H. Yu, "The detection of frequency hopping signal using compressive sensing," in *Information Engineering and Computer Science, 2009. ICIECS 2009. International Conference on*, 2009, pp. 1-4.
- [123] R. G. Baraniuk, "Compressive sensing [lecture notes]," *IEEE signal processing magazine*, vol. 24, no. 4, pp. 118-121, 2007.
- [124] E. Candes and J. Romberg, "l1-magic: Recovery of sparse signals via convex programming," *URL: www. acm. caltech. edu/l1magic/downloads/l1magic. pdf*, vol. 4, p. 14, 2005.
- [125] B. Lu, Q. Song, Z. Zhou, and X. Zhang, "Detection of human beings in motion behind the wall using SAR interferogram," *IEEE geoscience and remote sensing letters*, vol. 9, no. 5, pp. 968-971, 2012.
- [126] A. Ataman, B. Tekeli, and A. C. Gurbuz, "Development of a stepped frequency GPR prototype," in *Signal Processing and Communications Applications Conference (SIU), 2013 21st*, 2013, pp. 1-4.
- [127] M. Mercuri, P. J. Soh, L. Boccia, D. Schreurs, G. A. Vandenbosch, P. Leroux, and G. Amendola, "Optimized SFCW radar sensor aiming at fall detection in a real room environment," in *IEEE Topical Conference on*

- Biomedical Wireless Technologies, Networks, and Sensing Systems (BioWireleSS)*, 2013, pp. 4-6.
- [128] M. Zakrzewski, A. Singh, E. Yavari, X. Gao, O. Boric-Lubecke, J. Vanhala, and K. Palovuori, "Quadrature imbalance compensation with ellipse-fitting methods for microwave radar physiological sensing," *IEEE Trans. Microw. Theory Techn.*, vol. 62, no. 6, pp. 1400-1408, 2014.
 - [129] E. Yavari and O. Boric-Lubecke, "Channel imbalance effects and compensation for Doppler radar physiological measurements," *IEEE Trans. Microw. Theory Techn.*, vol. 63, no. 11, pp. 3834-3842, 2015.
 - [130] L. Kong, Y. Zhao, L. Dong, Y. Jian, X. Jin, B. Li, Y. Feng, M. Liu, X. Liu, and H. Wu, "Non-contact detection of oxygen saturation based on visible light imaging device using ambient light," *Optics express*, vol. 21, no. 15, pp. 17464-17471, 2013.
 - [131] M.-Z. Poh, D. J. McDuff, and R. W. Picard, "Advancements in noncontact, multiparameter physiological measurements using a webcam," *IEEE Trans. Biomed. Eng.*, vol. 58, no. 1, pp. 7-11, 2011.
 - [132] W. Verkrusse, L. O. Svaasand, and J. S. Nelson, "Remote plethysmographic imaging using ambient light," *Optics express*, vol. 16, no. 26, pp. 21434-21445, 2008.
 - [133] M.-Z. Poh, D. J. McDuff, and R. W. Picard, "Non-contact, automated cardiac pulse measurements using video imaging and blind source separation," *Optics express*, vol. 18, no. 10, pp. 10762-10774, 2010.
 - [134] M. Kumar, A. Veeraraghavan, and A. Sabharwal, "DistancePPG: Robust non-contact vital signs monitoring using a camera," *Biomedical optics express*, vol. 6, no. 5, pp. 1565-1588, 2015.
 - [135] K.-M. Chen, D. Misra, H. Wang, H.-R. Chuang, and E. Postow, "An X-band microwave life-detection system," *IEEE Trans. Biomed. Eng.*, vol. BME-33, no. 7, pp. 697-701, 1986.
 - [136] C. Li, Y. Xiao, and J. Lin, "Experiment and spectral analysis of a low-power \$ Ka \$-band heartbeat detector measuring from four sides of a human body," *IEEE Transactions on Microwave Theory and Techniques*, vol. 54, no. 12, pp. 4464-4471, 2006.
 - [137] J. Kuutti, M. Paukkunen, M. Aalto, P. Eskelinen, and R. E. Sepponen, "Evaluation of a Doppler radar sensor system for vital signs detection and activity monitoring in a radio-frequency shielded room," *Measurement*, vol. 68, pp. 135-142, 2015.
 - [138] D. Obeid, S. Samad, S. Sadek, G. Zaharia, and G. El Zein, "Position-Free Vital Sign Monitoring: Measurements and Processing," in *Advanced Biosignal Processing and Diagnostic Methods*, ed: InTech, 2016.
 - [139] C. Li, F. Chen, J. Jin, H. Lv, S. Li, G. Lu, and J. Wang, "A method for remotely sensing vital signs of human subjects outdoors," *Sensors*, vol. 15, no. 7, pp. 14830-14844, 2015.

- [140] L. Ren and A. E. Fathy, "Noncontact heartbeat detection using UWB impulse Doppler radar," in *USNC-URSI Radio Science Meeting (Joint with AP-S Symposium)*, 2015, pp. 221-221.
- [141] L. Ren, H. Wang, K. Naishadham, O. Kilic, and A. E. Fathy, "Phase-based methods for heart rate detection using UWB impulse Doppler radar," *IEEE Trans. Microw. Theory Techn.*, vol. 64, no. 10, pp. 3319-3331, 2016.
- [142] L. Ren, S. Nahar, A. E. Fathy, T. Phan, N. Tran, and O. Kilic, "Investigation of vital signs monitoring errors due to subject's orientation, clothing and distance from a SFCW radar," in *IEEE International Symposium on Antennas and Propagation (APSURSI)* 2016, pp. 1171-1172.
- [143] R. A. Fathy, H. Wang, and L. Ren, "Comparison of UWB Doppler radar and Camera based Photoplethysmography in Non-contact Multiple Heartbeats Detection," in *Biomedical Wireless Technologies, Networks, and Sensing Systems (BioWireleSS), 2016 IEEE Topical Conference on*, 2016, pp. 1-3.

APPENDIX

A.1 Differentiate and cross-multiply (DACM)

The DACM is introduced in Chapter 3.2 to avoid the wrapping problem

The derivative to the arctangent demodulation is computed as

$$\frac{d}{dt} \left[\arctan \frac{M(t)}{R(t)} \right] = \frac{R(t)\dot{M}(t) - \dot{R}(t)M(t)}{R(t)^2 + M(t)^2} \quad (2-35)$$

where $\dot{M}(t)$ and $\dot{R}(t)$ represent the slow time derivative of $M(t)$ and $R(t)$ respectively. Then integration is applied to (2-20) to retrieve results of the arctangent operation. In digital domain, the total phase information $\psi(t)$ can be calculated practically as [57],

$$\psi[n] = \sum_{k=2}^n \frac{R[k]\{M[k] - M[k-1]\} - M[k]\{R[k] - R[k-1]\}}{R[k]^2 + M[k]^2} \quad (2-36)$$

where differentiation is characterized as a forward difference and integration is approximated by an accumulation.

A.2 Imbalance compensation method

The imbalance compensation method is introduced in Chapter 3.2. It is proposed to correct such imbalance and dc offsets in UWB radar data

In presence of imbalance, the complex value obtained from Fourier transform of fast time samples will be $Y'(t, 0) = R' + j \cdot M'$.

$$R' = A_R \cos[-j2\pi\nu_c \tau_d(t) + \phi_R] + B_R \quad (2-37a)$$

$$M' = A_M \sin[-j2\pi\nu_c \tau_d(t) + \phi_M] + B_M \quad (2-37b)$$

where B_R and B_M denotes dc offsets; the amplitude imbalance between real and imaginary parts is $A_e = A_M/A_R$; the phase imbalance is $\phi_e = \phi_M - \phi_R$. The standard equation of ellipse using R' as horizontal axis and M' as vertical axis is [58],

$$R'^2 + A' \cdot M'^2 + B' \cdot R' \cdot M' + C' \cdot R' + D' \cdot M' + E' = 0 \quad (2-38)$$

then the amplitude imbalance and phase imbalance can be calculated as,

$$A_e = \sqrt{\frac{1}{A'}} \text{ and } \phi_e = \sin^{-1}\left(\frac{B'}{2\sqrt{A'}}\right) \quad (2-39)$$

It is obvious that all these five ellipse parameters can be acquired with five or more than five pairs of data samples (R', M'). The solution for $A', B', C', D',$ and E' can be obtained as [58],

$$\begin{bmatrix} A' \\ B' \\ C' \\ D' \\ E' \end{bmatrix} = (G^T G)^{-1} G^T b \quad (2-40)$$

where $K \times 5$ matrix G and $K \times 1$ matrix b are ($K \geq 5$),

$$G = \begin{bmatrix} (M'_1)^2 & R'_1 M'_1 & R'_1 & M'_1 & 1 \\ \vdots & \vdots & \vdots & \ddots & \vdots \\ (M'_K)^2 & R'_K M'_K & R'_K & \cdots & 1 \end{bmatrix} \text{ and } b = \begin{bmatrix} (R'_1)^2 \\ \vdots \\ (R'_K)^2 \end{bmatrix} \quad (2-41)$$

The dc offsets B_R and B_M can be estimated as well when ellipse parameters are available. As a result, the imbalance and dc offsets in the real and imaginary components of complex values obtained from Fourier transform can be effectively calibrated in real-time.

VITA

Lingyun Ren was born in Jintan, Jiangsu province, China in 1985. He received the B.S. and M.S. degrees in electrical engineering from the University of Electronic Science and Technology of China, in 2007 and 2010, respectively. He received his Ph.D. degree in electrical engineering (with a focus on biomedical applications of microwave/RF systems and microwave circuit design) at the University of Tennessee, Knoxville, in 2017.

Lingyun Ren was a finalist in the Student Paper Competition of the IEEE Topical Conference on Biomedical Wireless Technologies, Networks and Sensing Systems (BioWireleSS) in 2015 and 2016, and the IEEE MTT-S International Microwave Symposium in 2015.